



저작자표시-비영리-동일조건변경허락 2.0 대한민국

이용자는 아래의 조건을 따르는 경우에 한하여 자유롭게

- 이 저작물을 복제, 배포, 전송, 전시, 공연 및 방송할 수 있습니다.
- 이차적 저작물을 작성할 수 있습니다.

다음과 같은 조건을 따라야 합니다:



저작자표시. 귀하는 원 저작자를 표시하여야 합니다.



비영리. 귀하는 이 저작물을 영리 목적으로 이용할 수 없습니다.



동일조건변경허락. 귀하가 이 저작물을 개작, 변형 또는 가공했을 경우에는, 이 저작물과 동일한 이용허락조건하에서만 배포할 수 있습니다.

- 귀하는, 이 저작물의 재이용이나 배포의 경우, 이 저작물에 적용된 이용허락조건을 명확하게 나타내어야 합니다.
- 저작권자로부터 별도의 허가를 받으면 이러한 조건들은 적용되지 않습니다.

저작권법에 따른 이용자의 권리는 위의 내용에 의하여 영향을 받지 않습니다.

이것은 [이용허락규약\(Legal Code\)](#)을 이해하기 쉽게 요약한 것입니다.

[Disclaimer](#)



공학박사학위논문

포어어레이 박막을 이용한  
멀티스케일 입자분리

Separation of Multiscale Particles  
with Pore Array Membrane

2014년 8월

서울대학교 대학원

기계항공공학부

김 윤 호

# 포어어레이 박막을 이용한 멀티스케일 입자분리

Separation of Multiscale Particles  
with Pore Array Membrane

지도교수 이 정 훈

이 논문을 공학박사 학위논문으로 제출함

2014년 6월

서울대학교 대학원  
기계항공공학부  
김 윤 호

김윤호의 공학박사 학위논문을 인준함

2014년 8월

위 원장 : 최 만 수 (인)

부위원장 : 이 정 훈 (인)

위 원 : 김 호 영 (인)

위 원 : 김 성 재 (인)

위 원 : 정 남 조 (인)

## **Abstract**

# **Separation of Multiscale Particles with Pore Array Membrane**

Yunho Kim

School of Mechanical and Aerospace Engineering  
Seoul National University

Particles are governed by different physical laws in different scale. In small scale, the effects of the environment and other unexpected factors which are not significant in macro scale, become more dominant. Size of particles determines the intensity of governing forces and the behavior of the particle. For example, gravity is one of the dominating forces in the movement of macro particle such as dune sand. However, temperature and pH become more significant factors in molecular particles such as DNA and protein.

Recently applications in healthcare and environment use the separation of particles as a crucial process. Examples include pharmaceutical manufacturing/analysis, removal of air pollutants, wastewater treatment, and alternative energy production and storage. Based on mechanical, chemical, electromagnetic, and thermal properties of particles, various particle separation technologies have been developed over a period of time for different applications. Among these separation technologies,

membrane separation is an intuitive and effective method because of direct particle-pore interaction. Also membrane method has been well-developed and widely used in the field of microbiology. However more fundamental study is required to use the membrane-based separation for modern biological applications such as molecular binary separation and red blood cell filtering for point of care diagnosis. In this study, separation processes of molecular particle such as DNA and micro particle such as blood cell by pore array membrane have been investigated.

DNA as an aptamer is separated from a complex with protein by the nanoporous anodized aluminium oxide (AAO) membrane that has well controlled pores under 100 nm in diameter. For an effective separation, virtual pore size which is determined by electrical double layer (EDL) is controlled with different buffer condition based on ionic concentration. Electrophoretic (EP) force is applied to the negatively charged DNA through nano pores of AAO for translocation. Size exclusive binary separation process is achieved due to the size difference between DNA and DNA/protein complex. To verify the transport of DNA, fluorescence intensity change is measured, and the detail of the interaction process is analyzed.

Conventional AAO membranes are already used for various applications such as bio/chemical sensors, pre-treatment filters, and nanoscale templates. These AAO membranes are made from Al-foil substrate of thickness 50 to 100  $\mu\text{m}$ , and then usually assembled in to the other device. On the other hand, AAO membrane in this work is directly fabricated from deposited Al ( $< 2 \mu\text{m}$  thickness) on silicon substrate, followed by a MEMS fabrication process to complete an integrated device. This

direct AAO fabrication process can reduce the length of AAO nanochannel and improve the compatibility with microfluidic devices.

Blood cell is separated by micro pore array membrane with pore size of 2 to 10  $\mu\text{m}$ . For effective blood cells separation, the size of pores, the number of pores, and the spacing between pores are investigated. The blood cells which might block the pores are repelled from the pore by DEP force. DEP parameters such as electrode shape and applied voltage of frequency/amplitude, are studied for enhanced purity and recovery. In this analysis, it is crucial to compare hydrodynamic drag and DEP forces because the parametric complexity including pore array designs and DEP conditions is not sufficient to estimate only by experimental results.

Point-of-care (POC) diagnosis requires the blood plasma separation for the monitoring of cholesterol, glucose, and hepatic function in blood. Recent approaches include microfluidics-based blood separation by components. However, conventional microfluidic approaches used continuous process with large volume of sample through a syringe device. In POC application usually a small volume of analyte is needed in a single-shot processing on a compact platform. Our approach with the pore array membrane device satisfies such requirements for the single-shot separation with small droplet sample in a sample batch.

The understanding of characteristics of multiscale particles is applied to the separation of particles in two different domains such as DNA and blood cell with pore array membrane. Each of these particles has different size scale and characteristic properties such as density, elasticity, conductivity, etc. Basic principle

of separation for nano pore is the combination of physical pore diameter and thickness of electrical double layer. On the other hand, basic principle of separation for micro pore is the physical dimension of pore with respect to the particle size interacting with drag and DEP forces. Though EDL is negligible in micro pore because of relatively large pore diameter, EDL is an important factor in nano pore because of relatively small pore diameter. Also the driving forces for nano particle (DNA) and micro particle (Blood cell) are electrophoresis and dielectrophoresis, respectively. Through this study the effect of various factors that control for pore transport physics in different dimension is evaluated. This report presents a theoretical and engineering analysis of separation technique based on particle size, including experimental results of separation of DNA and blood cell from the blood using two different types of membrane devices.

.....

**Keywords:** Multiscale particle, separation, membrane separation, particle-pore interaction, DNA, molecule, blood cell, pore array membrane, AAO, EDL, electrophoresis, transport of DNA, dielectrophoresis

Student Number: 2005-21012

# Contents

Abstract .....	i
Contents .....	v
List of Figures .....	vii
List of tables.....	xiv
1      Introduction .....	1
1.1    Multiscale nature of particle-pore interaction .....	5
1.2    Particle-pore interaction in molecular scale .....	9
1.3    Particle-pore interaction in microscale.....	12
1.4    MEMS and microfluidics integration.....	15
1.5    Our approach.....	18
2      Part I: Separation of molecular sclaee particles .....	24
2.1    Concept and applications .....	26
2.1.1    Anodized aluminum oxide (AAO).....	28
2.1.2    Electrophoresis (EP).....	31
2.2    Theoretical background.....	33
2.2.1    Size of molecules.....	35
2.2.2    Electrical double layer (EDL) .....	38
2.3    Materials and methods .....	40
2.3.1    Molecular sample preparation.....	41
2.3.2    AAO fabrication process.....	42
2.3.3    MEMS integration process.....	49
2.3.4    Experimental setup.....	56
2.4    Results and discussion .....	57
2.4.1    DNA separation.....	57

2.4.2	DNA & protein separataion.....	63
2.5	Conclusions.....	65
3	Part II: Separation of microsclae particles .....	70
3.1	Concept and applications .....	72
3.1.1	Pore-array membrane .....	75
3.1.2	Dielectrophoresis (DEP) .....	80
3.2	Theoretical background.....	83
3.2.1	Forces on microparticle .....	85
3.2.2	DEP force expression on blood cell .....	87
3.2.3	Hydrodynamic drag force on blood cell.....	99
3.2.4	Balance between DEP vs. Hydrodynamic drag forces .....	104
3.3	Materials and methods .....	106
3.3.1	Blood sample preparation.....	107
3.3.2	MEMS integration process.....	109
3.3.3	Experimental setup.....	117
3.3.4	Evaluation methods .....	119
3.4	Results and discussion .....	120
3.4.1	Experiments with microbeads .....	120
3.4.2	Electrode shape optimization .....	122
3.4.3	Experiment with blood cells.....	124
3.5	Conclusions.....	135
4	Summary .....	140
4.1	Comparison between molecular and micro scale particles .....	141
4.2	Future work .....	143
4.3	Conclusions.....	145
	Abstract in Korean (국문초록).....	147
	Acknowledgement.....	

# List of Figures

Figure 1-1. Relative size of common materials, ionic range to macro particle range .....	5
Figure 1-2. (a) Filtration in microbiology is the passage of a liquid or gas through a screen like material with pores small enough to retain microorganisms., (b) clarifying filtration, (c) membrane filtration, (d) microporous membrane, (e) ultrafiltration .....	8
Figure 1-3. Examples of nanoscale particle-pore interaction. (a) Various nanopore methods, (b) anisotropic sieving through shallow nanometre sized gaps, (c) entropic DNA recoil .....	10
Figure 1-4. (a) Device concept. Only negatively charged molecules can pass through the nanoporous membrane when an electric field is applied (electrophoresis, EP), (b) SEM image of thin membrane, (c) SEM image of AAO nano pore .....	11
Figure 1-5. Examples of microscale particle-pore interaction. (a) Pinched flow fractionation, (b) RBC agglutination, (c) Biosite point-of-care testing test strip .....	13
Figure 1-6. Concept of blood plasma extraction device and components (DEP electrode + micro pore array membrane) .....	14
Figure 1-7. Microfluidics for LOC and $\mu$ TAS. (a) microfluidics channels, components and devices, (b) high-performance liquid chromatography in packed column, (c) trapping cells for large-scale single-cell analysis .....	17
Figure 2-1. (a) Device concept. Only negatively charged molecules can pass through the nanoporous membrane when an electric field is applied (electrophoresis, EP), (b) SEM image of thin membrane of AAO .....	26
Figure 2-2. Schematic of the pore formation mechanism in an acidic electrolyte .....	28
Figure 2-3. Anopore Inorganic Membranes (Anodisc, Whatman) .....	30
Figure 2-4. (a) concept of electrophoresis (EP), (b) gel electrophoresis of DNA, (c) dsDNA	

and worm-like DNA .....	31
Figure 2-5. Concept of effective pore size. The effective pore size is composed of AAO pore diameter and electrical double layer thickness (EDL). EDL thickness is affected by buffer concentrations. ....	33
Figure 2-6. DNA structures. (a) The structure of the DNA double helix, (b) chemical structure of DNA. ....	35
Figure 2-7. (a) interaction of DNA with protein (histones), (b) lambda repressor helix-turn-helix transcription factor bound to its DNA target .....	36
Figure 2-8. Illustration of EDL. (a) simplified illustration of the potential development in the area and in the further course of a Helmholtz double layer, (b) mathematical description of interfacial EDL .....	38
Figure 2-9. Schematic of molecular filtration. Only negatively charged molecules can pass through the nanoporous membrane when an electric field is applied. ....	39
Figure 2-10. Experimental set-up of AAO nanoporous membrane .....	40
Figure 2-11. Aptamer interaction with Thrombin. Binding of the protein Thrombin to a fluorescently labeled aptamer .....	41
Figure 2-12. T. The holder for anodizing process, (a) cathode & anode, acryl plates and O-ring made by Kyounghan Jung, (b) AAO process equipment set-up assembly .....	43
Figure 2-13. SEM images about pore widening w.r.t. etching time, (a) AAO ( $D_{pore} = \sim 28$ nm), (b) 10 min etching ( $D_{pore} = \sim 36$ nm), (c) 50 min etching $D_{pore} = \sim 69$ nm), (d) 70 min etching ( $D_{pore} = \sim 85$ nm), (e) 90 min etching ( $D_{pore} = \sim 100$ nm) .....	44
Figure 2-14. The relation between pore diameter ( $D_{pore}$ ) and etching time in 10 wt.% H <sub>3</sub> PO <sub>4</sub> , etch rate = ~0.8 nm/min @R.T. ....	45
Figure 2-15. SEM images of AAO nanoporous membrane. (a) 500 nm thickness of free-standing AAO membrane on Si substrate. (b) magnified view of AAO membrane .....	46

Figure 2-16. SEM images of AAO nanoporous membrane. (a) backside view of AAO membrane. (b) nano-pore size distribution.....	47
Figure 2-17. SEM images of Ru coated on AAO nanoporous membrane. Ru is deposited by ALD process. The AAO pore diameter is reduced from 38 nm to 13 nm.....	48
Figure 2-18. Fabrication process of a free-standing AAO nano-porous membrane (A), PDMS microchannel (B).....	49
Figure 2-19. SEM image of AAO on the free-standing Si <sub>3</sub> N <sub>4</sub> membrane. The AAO membrane is broken, but it maintains the free standing shape.....	50
Figure 2-20. Images AAO membrane in fabrication steps, before (left) and after (right) sacrificial layers etching.....	52
Figure 2-21. SEM images of Si <sub>3</sub> N <sub>4</sub> etching on free-standing AAO membrane, (a) 0 min, 350 nm, (b) 7 min, 90 nm, (c) (7 + 3) min, < 10 nm, (d) (7+5) min, 0 nm.....	54
Figure 2-22. (A) Device integration schematic of the AAO membrane and double side PDMS microchannels, (B) Device images after bonding process with O <sub>2</sub> plasma .....	55
Figure 2-23. Experimental equipment. (a) Nikon Eclipse_ME600L, (b) Keithley 2440 .....	56
Figure 2-24. Control of effective pore size by ionic strength. 50×, 5×, and 0.5× TAE buffer condition .....	59
Figure 2-25 Biomolecular transport in different ionic strength 50×, 5×, and 0.5× TAE buffer condition, respectively. Green arrow indicate the direction and quantity of bimolecular transport. ....	60
Figure 2-26. Biomolecular separation through the nanoporous membrane. Changes in current during the translocation of DNA through the AAO nanoporous membrane .....	61
Figure 2-27. . Biomolecular separation through the nanoporous membrane. ssDNA translocation vs. applied voltage, .....	62
Figure 2-28. . Biomolecular separation through the nanoporous membrane. ssDNA translocation vs. different ssDNA concentrations. ....	62
Figure 2-29. Biomolecular separation through the nanoporous membrane. Performance of	

size specific biomolecular separation of an aptamer and aptamer-thrombin complex at 5 V .....	64
Figure 3-1. Concept of plasma extraction. On the micron size of pore-array, DEP electrodes are patterned to prevent the blood cell clogging on the pore. Red parts are blood cells (RBCs), yellow parts are DEP electrodes, and grey parts are pore-array membranes .....	73
Figure 3-2. Composition of human blood. Plasma is a pale yellow-colored, clear liquid that is 91% water, 7% proteins, and 2% other substances including ions, nutrients, gases, and waste products .....	73
Figure 3-3. The conventional clinical way for plasma extraction. This centrifugal method requires long processing time, large amount of blood sample, bulky space and relatively high external power .....	74
Figure 3-4. Blood cell size distribution. Thrombocyte (platelet) is 2-3 $\mu\text{m}$ size. ....	75
Figure 3-5. Photographs of the fabricated filters with different hole geometries .....	76
Figure 3-6. Photographs of the filters before and after Parylene deposition .....	76
Figure 3-7. Schematics of the microfilter designs (a) weir filter (side view), (b) pillar filter (top view), (c) crossflow filter (top view), (d) membrane filter (side view) ...	77
Figure 3-8. Schematic illustrating dielectrophoresis (DEP) resulted from electric force. a) uniform electric field, b) non-uniform field .....	80
Figure 3-9. Plasma separation using various active energy source. A) acoustophoresis, B) dielectrophoresis (DEP) combined with capillary force, C) bulk electrohydrodynamics thrust or ionic winds generated by sharp corona electrode tip .....	81
Figure 3-10. Schematic diagram of force balance between DEP force and hydrodynamic viscous force. ....	83
Figure 3-11. Blood cell filter images for theoretical modeling. (a) MEMS filter with PDMS microchannel, (b), (c) DEP electrode (yellow) on pore array membrane (green)	

.....	84
Figure 3-12. Schematic of forces on blood cell, RBC. (Blue arrow: DEP force, green arrow: hydrodynamic drag force, grey arrow: gravity force). .....	85
Figure 3-13. Real part of the CM factor change depending on electric field frequency .....	90
Figure 3-14. Various shapes of non-uniform DEP electrode for blood cell separation. Yellow area is the gold electrode, and grey area is the membrane of $\text{Si}_3\text{N}_4$ . .....	91
Figure 3-15. Finite element analysis (FEA) modeling of gap between the positive and negative electrode using COMSOL 3.5. ....	92
Figure 3-16. FEA result for electric field between electrodes, when voltages are positive (+5 V) and negative (-5 V) on each electrode. ....	93
Figure 3-17. FEA for DEP(number of mesh=39,097), (a) mesh, (b) electric field, (c) DEP .....	94
Figure 3-18. FEA for DEP(number of mesh=625,552), (a) mesh, (b) electric field, (c) DEP .....	95
Figure 3-19. DEP force comparison between mid-line and corner-line. ....	96
Figure 3-20. Schematic and FEA result about flow field near the pore (3 $\mu\text{m}$ ). ....	98
Figure 3-21. Horizontal flow velocity with various pore sizes on the membrane surface. The diameter of pore sizes are 1, 3, 5, 7, 9 $\mu\text{m}$ , respectively. ....	99
Figure 3-22. Horizontal flow velocity of different spacing between pores. The diameter of a pore is 3 $\mu\text{m}$ and the spacing between pore centers is 0, 5, 7 $\mu\text{m}$ . ....	101
Figure 3-23. Horizontal flow velocity of different pore numbers (N=1, 3, 5). The diameter of a pore is 3 $\mu\text{m}$ and the spacing between pore centers is 4 $\mu\text{m}$ . ....	103
Figure 3-24. Force balance between FDEP and Fdrag on membrane. (Blue line: FDEP at mid, grey line: FDEP at corner, yellow red line: Fdrag) .....	104
Figure 3-25. Concept of blood plasma extraction device and components. The system consists of blood sample and MEMS filter. The MEMS filter combines DEP function and micro pore array which is made by microfabrication process. ....	106

Figure 3-26. Phlebotomy: Syringe draw procedure, Venipuncture and EDTA tube .....	107
Figure 3-27. Inverted microscope images of RBC in various dilution ratio. ....	108
Figure 3-28. MEMS filter devices. The right one is the first version device (25 mm × 12 mm) and the left one is the second version device (11.75 mm × 8.45 mm). ....	110
Figure 3-29. Cross-section view of the integrated MEMS filter and microchannels. (a) first design version, (b) second design version .....	111
Figure 3-30. Fabrication process of MEMS filter. (a) Si <sub>3</sub> N <sub>4</sub> deposition on silicon, (b) micro pore array patterning on Si <sub>3</sub> N <sub>4</sub> , (c) gold electrode for DEP patterning, and (d) anisotropic KOH wet etching .....	112
Figure 3-31. MEMS filter device images by SEM. (a), (c) DEP electrode, (b) membrane by KOH etching, (d) parameters, (e), (f) pore between electrodes, (h), (i) pores on membrane .....	116
Figure 3-32. Experimental setups for blood filtration. (a) inverted microscope for cell counting, (b) metal microscope for DEP effectiveness of blood cell, and (c) Macroscopic camera for measuring blood droplet. ....	118
Figure 3-33. Inverted microscope image for DEP with microbeads. ITO is used for DEP electrode, and substrate is glass wafer. (a) before the voltage applied and after the voltage turned on. Beads were arranged differently by the distinct electrode arrays such as the shapes of (b) crescent, (c) crossed rectangles, (d) narrow crossed rectangles and (e) fingers. ....	121
Figure 3-34. Two different electrode shapes which could generate strong DEP force. The areas which seem brighter are electrodes and the perfectly circular black dots between electrodes are micropores. The diameters of pores in both cases are 8 μm. It was not possible to find pores in photos before DEP was applied but pores came into view after beads were trapped onto electrodes .....	123
Figure 3-35. Blood cell separation efficiencies of different electrode shapes. Photos show comparison between the number of blood cells near pore array before and after	

applying DEP voltage. ....	125
Figure 3-36. Blood cell separation with DEP by metal microscope. DEP conditions are $V_{pp} = 10$ V, 500 kHz, 3min, (20:1 = buffer: blood) .....	126
Figure 3-37. Purity of blood cell after filtration with various pore sizes. (a) Original diluted blood (b) 2 $\mu$ m pore result, (c) 3 $\mu$ m pore result, (d) 4 $\mu$ m pore result, and (e) 5 $\mu$ m pore result by inverted microscope .....	127
Figure 3-38. Concept diagram of relation between a droplet on surface and contact angle. ....	128
Figure 3-39. Schematic of sessile drop and surface treatment .....	130
Figure 3-40. Shrinking droplet (20 $\mu$ l) with (a) 5 $\mu$ m pores and (b) 3 $\mu$ m pores, 5 minutes after blood dropped on the surface. In the device with a diameter of 3 $\mu$ m, pores were blocked with blood cells and blood flow was stopped. ....	131
Figure 3-41. Diluted blood cell droplet (40:1, 40 $\mu$ m) contact angle change with/without DEP applied ( $V_{pp}=10$ V, 500 kHz). The droplet volume change is (on:off = 14.2 : 1.6). Also without DEP, filtration through pore array takes more than 100 min.. ·	131
Figure 3-42. Relation between purity and recovery with pore diameter from 2 $\mu$ m to 15 $\mu$ m. ....	132
Figure 3-43. DEP effectiveness comparison with diluted blood (20:1). DEP force makes pore array be exposed by moving away blood cells. ....	134

## List of tables

Table 1-1. Dimensionless numbers and their relation to the dimension length (at constant velocity) .....	11
Table 1-2. Continuous flow separation methods based on the principles and samples .....	18
Table 2-1. Typical Data – Anopore Inorganic Membranes (Anodisc, Whatman) .....	30
Table 2-2. Detail fabrication protocol for AAO nano filter and microchannel .....	51
Table 2-3. EDL thickness & effective pore size w.r.t. buffer concentration in bulk conditions .....	60
Table 3-1. Total pore area and measured blood handling capacity of the microfilters .....	78
Table 3-2. Efficiency of microfilters for passing RBCs and trapping WBCs at a given flow of blood .....	78
Table 3-3. Parameterization of multi-shelled spheroid model .....	87
Table 3-4. Conductivity change of various dilution ratio of blood and buffer. ....	108
Table 3-5. Detail process protocol for MEMS filter and microchannel .....	114

# 1 Introduction

Particles are governed by different physical laws in different scale. In small scale, the effects of the environment and other unexpected factors which are not significant in macro scale, become more dominant. Size of particles determines the intensity of governing forces and the behavior of the particle. For example, gravity is one of the dominating forces in the movement of macro particle such as dune sand. However, temperature and pH become more significant factors in molecular particles such as DNA and protein.

Recently applications in healthcare and environment use the separation of particles as a crucial process [1]. Examples include pharmaceutical manufacturing/analysis [2], removal of air pollutants [3], wastewater treatment [4], and alternative energy production and storage [5]. Based on mechanical, chemical, electromagnetic, and thermal properties of particles, various particle separation technologies have been developed over a period of time for different applications [6]. Among these separation technologies, membrane separation is an intuitive and effective method because of direct particle-pore interaction. Also membrane method has been well-developed and widely used in the field of microbiology. However more fundamental study is required to use the membrane-based separation for modern biological applications such as molecular binary separation and red blood cell filtering for point of care diagnosis. In this study, separation processes of molecular particle such as

DNA and micro particle such as blood cell by pore array membrane have been investigated.

Many researches have been performed recently in miniaturization and integration of separation system based on lab-on-a-chip (LOC) and micro total analysis system ( $\mu$ TAS), which boasts great advantages including large reaction volume, short diffusion time, accurate sample amount, precise experiment control, economical costs and more [7, 8]. However, bulky surrounding components including the pump, valve, tube, and external power sources have sets limitations to scale down the size. For instance, the pneumatic actuation valve and pump by Quake *et al.* is one of the most well-known microfluidics components [9]. However, while the microchannel in the system could be miniaturized, the bulky peripheral devices like the vacuum pump was extremely difficult to downsize.

DNA as an aptamer is separated from a complex with protein by the nanoporous anodized aluminium oxide (AAO) membrane that has well controlled pores under 100 nm in diameter. For an effective separation, virtual pore size which is determined by electrical double layer (EDL) is controlled with different buffer condition based on ionic concentration. Electrophoretic (EP) force is applied to the negatively charged DNA through nano pores of AAO for translocation. Size exclusive binary separation process is achieved due to the size difference between DNA and DNA/protein complex. To verify the transport of DNA, fluorescence intensity change is measured, and the detail of the interaction process is analyzed.

Conventional AAO membranes are already used for various applications such as bio/chemical sensors, pre-treatment filters, and nanoscale templates. These AAO

membranes are made from Al-foil substrate of thickness 50 to 100  $\mu\text{m}$ , and then usually assembled in to the other device. On the other hand, AAO membrane in this work is directly fabricated from deposited Al ( $< 2 \mu\text{m}$  thickness) on silicon substrate, followed by a MEMS fabrication process to complete an integrated device. This direct AAO fabrication process can reduce the length of AAO nanochannel and improve the compatibility with microfluidic devices.

Blood cell is separated by micro pore array membrane with pore size of 2 to 10  $\mu\text{m}$ . For effective blood cells separation, the size of pores, the number of pores, and the spacing between pores are investigated. The blood cells which might block the pores are repelled from the pore by DEP force. DEP parameters such as electrode shape and applied voltage of frequency/amplitude, are studied for enhanced purity and recovery. In this analysis, it is crucial to compare hydrodynamic drag and DEP forces because the parametric complexity including pore array designs and DEP conditions is not sufficient to estimate only by experimental results.

Point-of-care (POC) diagnosis requires the blood plasma separation for the monitoring of cholesterol, glucose, and hepatic function in blood. Recent approaches include microfluidics-based blood separation by components. However, conventional microfluidic approaches used continuous process with large volume of sample through a syringe device. In POC application usually a small volume of analyte is needed in a single-shot processing on a compact platform. Our approach with the pore array membrane device satisfies such requirements for the single-shot separation with small droplet sample in a sample batch.

The understanding of characteristics of multiscale particles is applied to the separation of particles in two different domains such as DNA and blood cell with pore array membrane. Each of these particles has different size scale and characteristic properties such as density, elasticity, conductivity, etc. Basic principle of separation for nano pore is the combination of physical pore diameter and thickness of electrical double layer. On the other hand, basic principle of separation for micro pore is the physical dimension of pore with respect to the particle size interacting with drag and DEP forces. Though EDL is negligible in micro pore because of relatively large pore diameter, EDL is an important factor in nano pore because of relatively small pore diameter. Also the driving forces for nano particle (DNA) and micro particle (Blood cell) are electrophoresis and dielectrophoresis, respectively. Through this study the effect of various factors that control for pore transport physics in different dimension is evaluated. This report presents a theoretical and engineering analysis of separation technique based on particle size, including experimental results of separation of DNA and blood cell from the blood using two different types of membrane devices.

## 1.1 Multiscale Nature of particle-pore Interaction

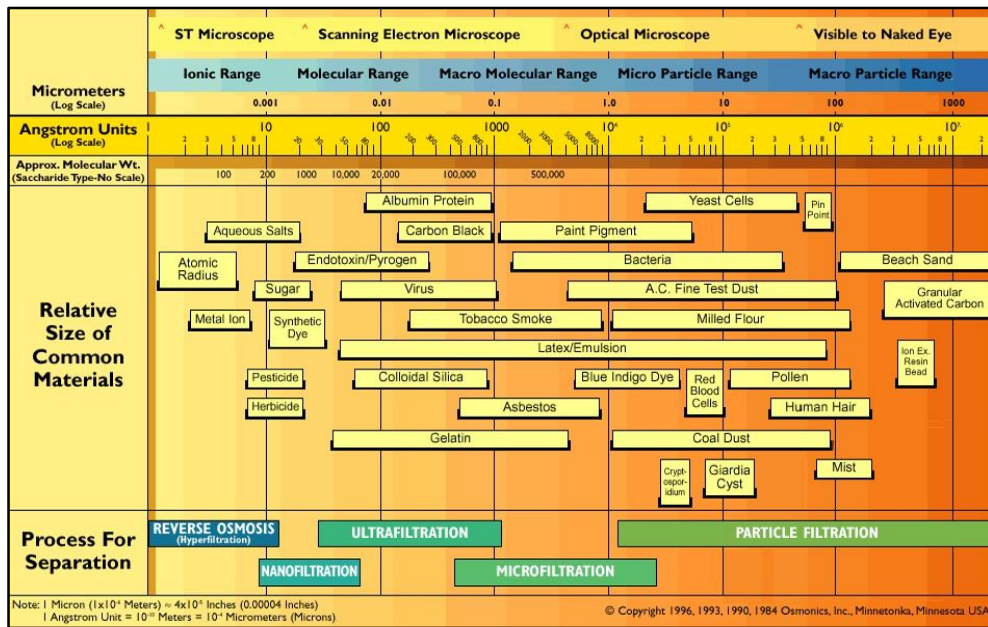


Figure 1-1. Relative size of common materials, ionic range to macro particle range [10]

Scale of context is a keyword to comprehend multiscale particle physics and phenomenon in this paper. Depending on particle's size, effects of forces applied on a particle show different results. In Figure 1-1, multiscale particle from macro ( $< 1000 \mu\text{m}$ ) to ionic ( $< 10\text{\AA}$ ) range needs process variation for separation from particle filtration to reverse osmosis. Not only does it need a separation process, but also observation methods should vary from naked eye to scanning tunnelling (ST) microscope. Furthermore, the meaning of "size" could differ according to the particle range. In other words, in molecular range, radius of gyration tends to describe the dimension of the particle. Therefore, a deep understanding of particle scale is essential for multiscale particle research.

Table 1-1. Dimensionless numbers and their relation to the dimension length (at constant velocity);  $\beta$  thermal expansion coefficient (1/K),  $c$  surface tension (N/m),  $\eta$  dynamic viscosity (Pa·s),  $\rho$  mass density (kg/m<sup>3</sup>),  $T$  temperature (K),  $g$  constant of gravity (m/s<sup>2</sup>),  $l$  (characteristic) length (m),  $v$  velocity (m/s). Adapted from the more comprehensive list in Ref. [11]

Group	Abbreviation	Definition	Interpretation	Order length
Bond number	$Bo$	$\frac{g(\rho_l - \rho_v)l^2}{\gamma}$	Ratio of gravitational and surface tension forces	2
Grashof number	$Gr_L$	$\frac{g\beta\rho^2(T_s - T_\infty)l^3}{\eta^2}$	Ratio of buoyancy to viscous forces	3
Reynolds number	$Re_L$	$\frac{\rho v l}{\eta}$	Ratio of the inertia and viscous forces	1
Weber number	$We$	$\frac{\rho v^2 l}{\gamma}$	Ratio of inertia to surface tension forces	1
Capillary number	$Ca$	$\frac{v\eta}{\gamma}$	Ratio of viscous and surface tension forces	0

Dimensionless numbers related to dimension length ( $l$ ) in Table 1-1 are proper indicators for scale of context. For instance, Reynolds number ( $Re$ ) is the most famous dimensionless number in fluid mechanics, which defines the ratio between inertia and viscous forces.  $Re$  is also frequently used to pinpoint whether laminar or turbulent flow exists. While laminar flow at low  $Re$  is dominated by viscous forces, turbulent flow at high  $Re$  is controlled by inertial forces. As shown in Table 1-1, the order length of  $Re$  is “1”, which means scale of  $l$  directly influence fluid characteristics. Thus, for the smaller  $l$ , viscous force is larger. On the other hand, capillary number ( $Ca$ ) which is defined by the ratio between viscous and surface tension force, has an order length of “0”. This means the effects of viscosity and surface tension is equal regardless of  $l$ . Among the dimensionless numbers in Table 1, Grashof number ( $Gr$ ), which explains the ratio between buoyancy to viscous in

heat transfer and fluid dynamics involving natural convection, has the largest value of “3” order length. In the small range of  $l$ , buoyancy influence is almost negligible compared with the viscous force. Consequently, the influence factor of various forces can be manipulated depending on  $l$ , causing multiscale particles with different ranges of  $l$  in need of estimation for the effective force applied on the particle.

In short, as particle is near molecular scale region, behaviour of particle could be much different from macro region one. Therefore a thorough understanding of these phenomenon is required for multiscale particle study. Based on literature survey and investigation, we predict these phenomenon in advance and try to solve problems that might occur during experiments.

Various types of particle separation methods applying mechanical, chemical, electromagnetic, thermal diffusive principles have been developed for broad application fields [6]. Recently, with rise in healthcare and environmental concerns, particle separation became an essential process in clinical diagnosis, pharmaceutical manufacturing and analysis, removal of air pollutants, waste water treatment, alternative energy production and storage. Among the particle separation technologies, membrane separation is known to be size-exclusive, intuitive, effective, reliable, and well-developed method in microbiology [12]. Also, membrane separation can cover a wide separation range, from ionic particles to macro particles as shown in Figure 1-1 [10].

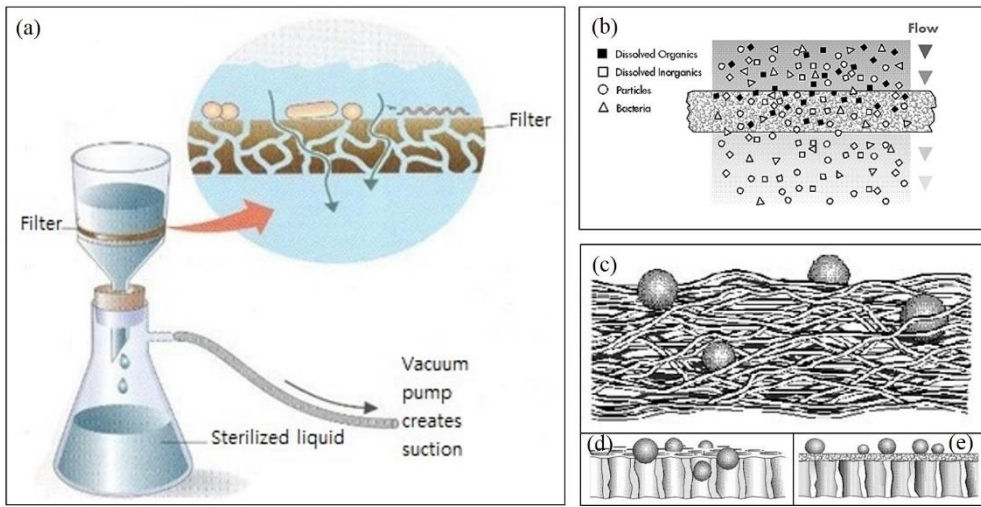


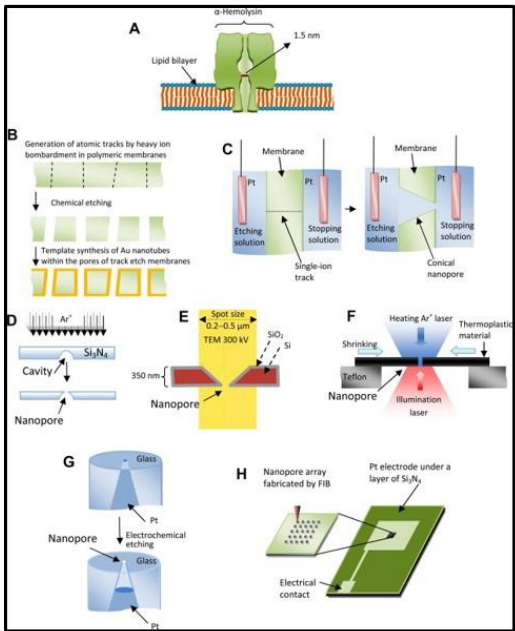
Figure 1-2. (a) Filtration in microbiology is the passage of a liquid or gas through a screen like material with pores small enough to retain microorganisms. [12], (b) clarifying filtration, (c) membrane filtration, (d) microporous membrane, (e) ultrafiltration [13]

Representative membrane separation (Figure 1-2 (a)) cases are divided into clarifying filtration (Figure 1-2. (b)) and membrane filtration (Figure 1-2. (c)) [13]. Clarifying filtration is effective for removal of organic impurities using a method known as “fouling” in membrane pores. On the other hand, membrane filtration utilizes size “screening” process. After the membrane screening process, porous membranes are separated into undersize and oversize. While undersize passes through the membrane easily, oversize remains on the membrane. Generally, particle size  $20\text{ }\mu\text{m}$  is the criterion to decide whether dry screening or wet screening is needed for particles under  $20\text{ }\mu\text{m}$  size tend to assemble with other particles, sticking to larger particles due to humidity in air.

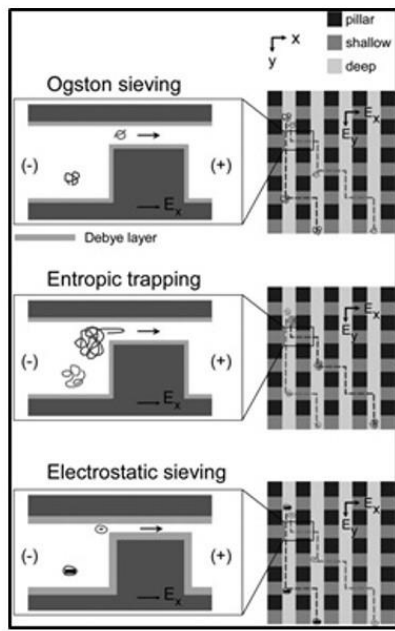
## 1.2 Particle-pore interaction in molecular scale

In molecular range, there are several characteristic phenomenon related to particle size. Extraordinary phenomenon in large particle region can occur in small particle region [14]. For example, electric double layer (EDL) overlap happens in nanochannel [15]. The conductivity through EDL increases on downscaling due to the high surface to volume ratio. When EDL overlap happens, hydrostatic pressure will increase in nanochannel. Thus, the transport of particle through nanochannel would be influence. Another phenomenon in small scale is relate to size of molecule and steric repulsion. Due to the flexible conformational state of molecule, rigid molecule could not pass through the pore even the same average radius [16]. Molecular size of water ( $H_2O$ ) and the fully stretched 10-kbp DNA would be 0.3 nm and 3.4  $\mu m$  range, which cover several orders of magnitude. Furthermore, in sub-nanometre scale, entropy change can influence on size exclusion [17]. DNA which is a flexible molecule has higher possibility of coiled state than fully stretched state [18]. Due to the coil state, DNA is more likely to stay in bulky space, and to make the maximum entropic energy gain [19]. This maximized entropy in nanoslit or nanochannel affects DNA separation in “entropic trap.” [17] Hence, large radius of gyration of DNA could easily pass through nanochannel in Figure 1-3 (b). DNA also can be recoiled by external electric field in Figure 1-3 (c) [20]. Also, in order to separate and sense molecular particles, various methods for nanopore fabrication have been developed from biological protein pore to micromachining fabrication assembled patterning pore in Figure 1-3 (a) [21]. In Figure 1-3 (a), nanopore array with FIB (focused ion beam) method is comparable with our AAO nanoporous membrane method.

(a)



(b)



(c)

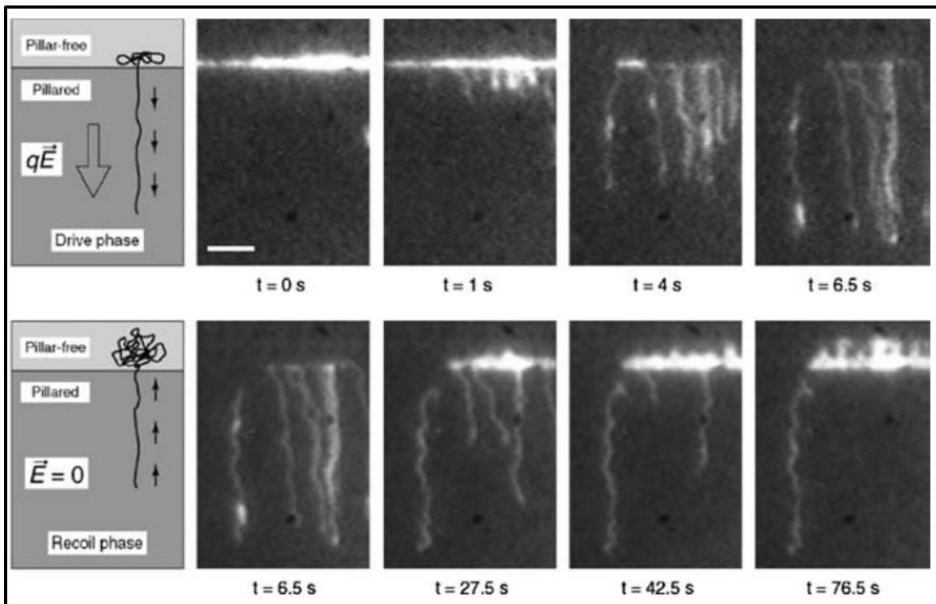


Figure 1-3. Examples of nanoscale particle-pore interaction. (a) Various nanopore methods [21], (b) anisotropic sieving through shallow nanometre sized gaps [22], (c) entropic DNA recoil [20]

In this study, biomolecules as molecular scale particles are separated by nanoporous membrane. Separation and filtration of biomolecules using the nano-porous membrane can play central roles to many analytical and purification process. Gel electrophoresis, for example, is used to sort charged biopolymers according to weights for interrogating the molecular composition of a certain mixture. Proteins that cause a disease can be removed through a blood filtration from a patient. DNA purification can be achieved through a size specific separation and collection after cell lysis [17, 23]. Among various applications, the nano-pore based translocation of single strand DNA (ssDNA) is a vital issue because of their utility in fast DNA sequencing [24-26].

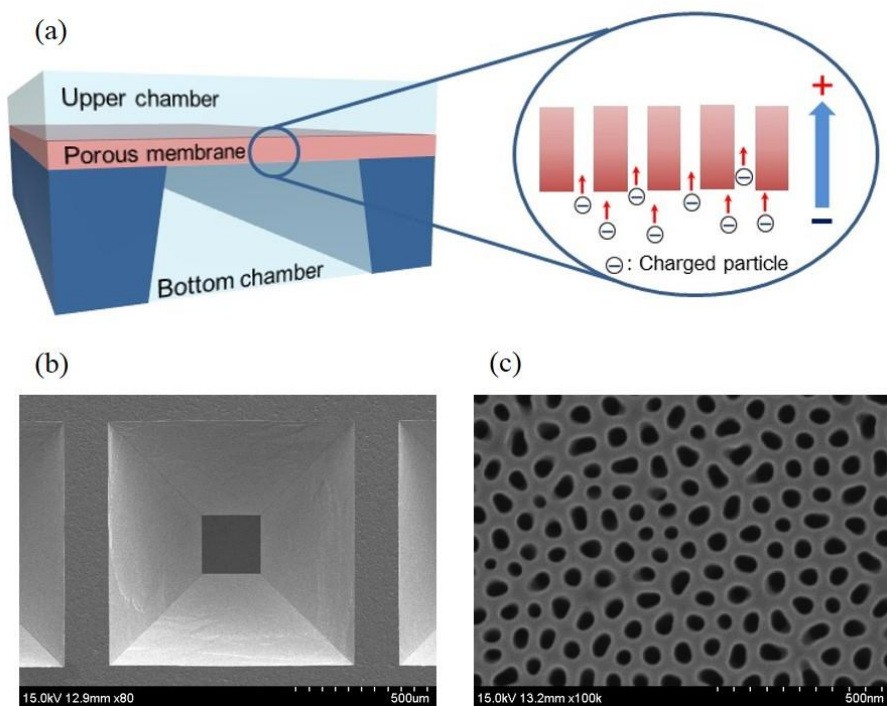


Figure 1-4. (a) Device concept. Only negatively charged molecules can pass through the nanoporous membrane when an electric field is applied (electrophoresis, EP), (b) SEM image of thin membrane, (c) SEM image of AAO nano pore

For efficient biomolecule separation based on nano-porous membrane, some of the key properties that materials with controlled pore diameter, length and surface chemistry are required. However, commercially available nano-porous membranes possess pore size-cutoff properties and low transport rates since they generally have broad size distributions and relatively large thickness values. Anodized aluminum oxide (AAO) membrane has the potential to be a good nano-porous membrane element for biomolecule separation because of its very high pore density, e.g., up to  $24 \times 10^{20}$  pores/cm<sup>2</sup>, its relative uniform pore sizes, as well as the availability of the sub 100 nm pores [27].

### 1.3 Particle-pore interaction in microscale

In micro particle range, comparing with the phenomenon in molecular range, micro particles behavior is more intuitive than the smaller particle. As shown in previous Table 1-1, *Re* in general microfluidics is low, which means laminar flow and viscous force are dominant in microchannel. Also surface phenomenon such as surface tension, surface charge, and capillary forces mostly drive passive fluid actuation. Laminar flow settings and well-ordered diffusion allow frequently and spatially very resolute reactions with tiny solution consumption [28]. Based on various fluidic principles, several continuous flow separation devices have been developed. For example, laminar flow and no diffusion in microchannel are used to separated micro particles in Figure 1-5 (a) [29]. Especially in blood cell separation, agglutination of blood cell should be considered because the size of particle separation is different from each blood cell size in Figure 1-5 (b) [30]. Also, in order to diagnose cardiac

disease, plasma from blood is separated with surface tension driven flow in Figure 1-5 (c) [31].

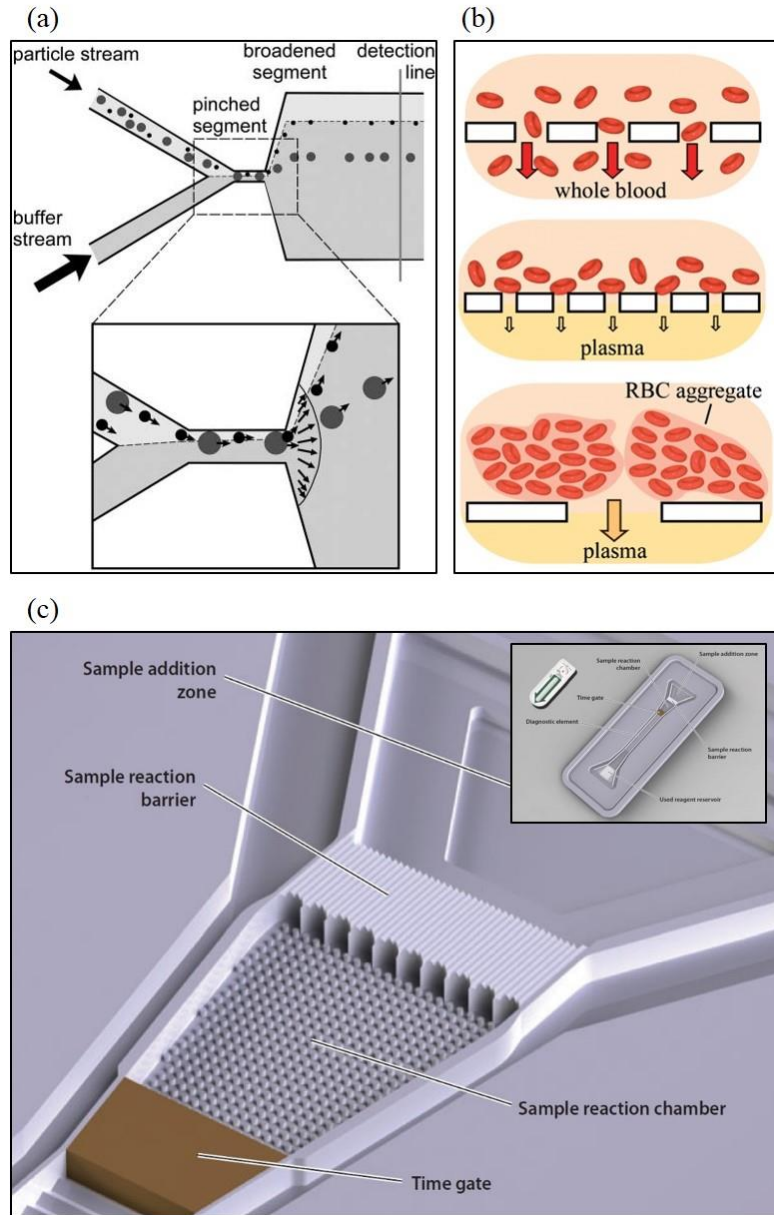


Figure 1-5. . Examples of microscale particle-pore interaction. (a) Pinched flow fractionation [29], (b) RBC agglutination [30], (c) Biosite point-of-care testing test strip [31]

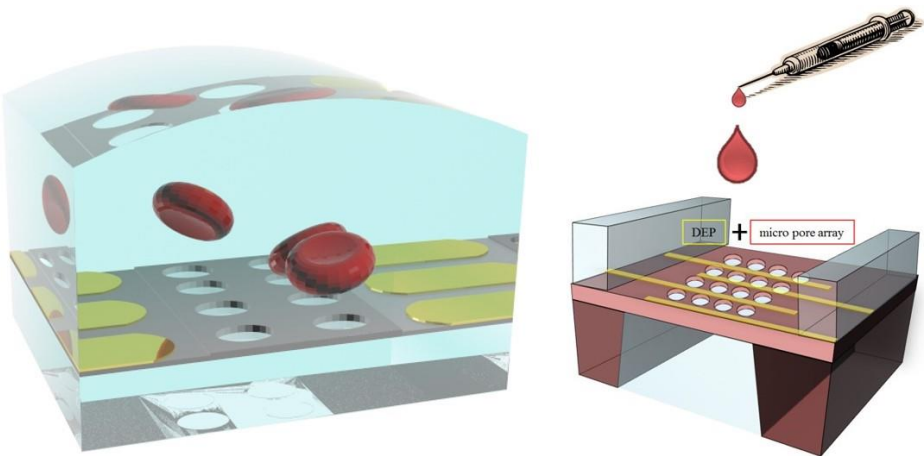


Figure 1-6. Concept of blood plasma extraction device and components (DEP electrode + micro pore array membrane)

Blood cell, as a micro particle, separation from blood is a crucial process for many clinical tests and assays. For example, point-of-care (POC) diagnosis requires the blood plasma separation for the monitoring of cholesterol, glucose, and hepatic function in blood [1, 32]. In order to achieve detection of various target proteins with high sensitivity and reliability, such separation process is necessary [33]. Various microfluidic devices for blood separation and plasma extraction have been developed [34-39]. Recent approaches include microfluidics-based blood component separation. Microfluidics has many advantages such as only needing small sample volume for experiment. Recently, various types of blood cell separation method have developed such as microchannel with trench (SIMBAS) [40], paper-based analytical device ( $\mu$ -PAD) [30], centrifugal platform [41], and surface acoustic wave (SAW) [33] and so on. However microchip of microfluidics had given rise to limitations in various sample preparation, separation methods and integrated blood

analysis modules [42]. Furthermore, these methods are generally horizontal systems with limited flux capacity per unit time. Here we suggest a vertical separation device for high throughput and high quality separation efficiency through integration of dielectrophoretic (DEP) function on a micro-porous membrane.

In this study, we design a blood plasma extraction device that integrates DEP function on a micro-patterned membrane. It has been demonstrated in a previous research that a pore array with size variation could filter the blood particles with different efficiency of separation [30]. We target enhancing the separation efficiency and speed by establishing a “virtual barrier” with DEP function integrated on a membrane with a regular pore size and distribution. Metal electrodes are patterned on the membrane for preventing clogging by blood cells through the application of negative DEP, while helping blood plasma to pass through the membrane pores selectively. Essentially the DEP force is designed to block the passage of red blood cells (RBCs), which account for more than 90% of the whole blood cells including white blood cells (WBCs) and platelets. The diameter of micro pore array are varied between 3~10  $\mu\text{m}$ , but targeted to filter RBCs of which size is approximately 6~8  $\mu\text{m}$ .

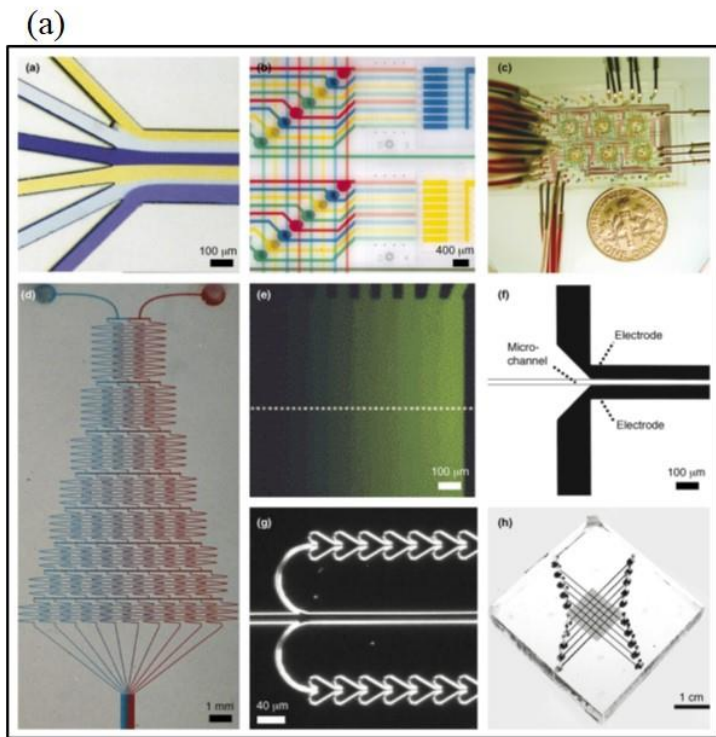
## 1.4 MEMS and microfluidics integration

Miniaturization and integration of bio-analysis system are related to lab-on-a-chip (LOC) and micro total analysis system ( $\mu\text{TAS}$ ) in chemistry, biology, engineering

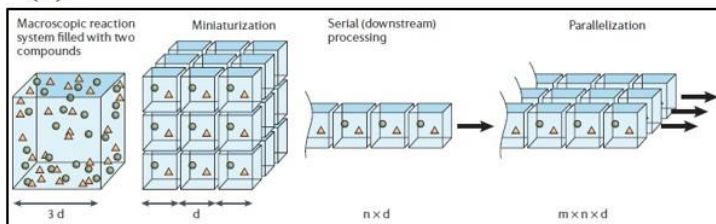
and medicine [7, 8]. Based on the development of microfluidics, the previous bulky system can be downsized without deteriorating performance. Microfluidics present various advantages including large reaction volume, short diffusion time, accurate sample amount, precise experiment control, economical cost, and more. Moreover, the structure scale of microfluidics is suitable within biology and biomedicine due to the compatible intrinsic size of eukaryotic cells, collections of cells, and organelles [43]. One of the characteristics of microfluidics is the laminar flow which is related to  $Re$  introduced previously.  $Re$  in microfluidics is usually under 2000, and viscous force dominates the flow of fluid. Due to the laminar flow, mixing only occurs by diffusion and stable gradients of flow are typically perpendicular.

However, bulky surrounding components including the pump, valve, tube, and external power sources have sets limitations to scale down the size. For instance, the pneumatic actuation valve and pump by Quake *et al.* is one of the most well-known microfluidics components [9]. However, while the microchannel in the system could be miniaturized, the bulky peripheral devices like the vacuum pump were extremely difficult to downsize.

In this study, pore array membrane using micro electromechanical system (MEMS) and PDMS microfluidics are prepared and integrated to separate multiscale particles. Based on MEMS process, thin ( $< 1 \mu\text{m}$ ) thickness membrane and uniform pore size ( $< 10 \mu\text{m}$ ) can be achieved. Then, PDMS microchannel using soft lithography helps fluidic system to be compact and efficient resulting in a small amount of sample volume.



(b)



(c)

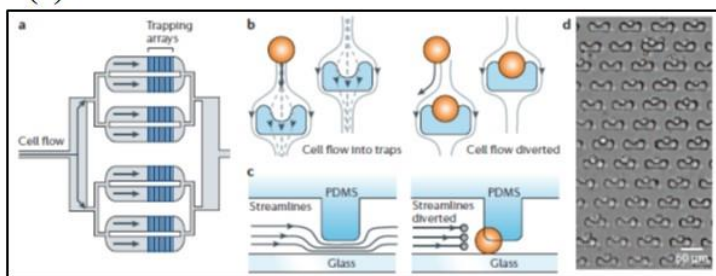


Figure 1-7. Microfluidics for LOC and  $\mu$ TAS. (a) microfluidics channels, components and devices [7], (b) high-performance liquid chromatography in packed column [8], (c) trapping cells for large-scale single-cell analysis [8]

Table 1-2. Continuous flow separation methods based on the principles and sample [35]

Method	Separation induced by	Separation based on	Sample
Pinched flow fractionation	Laminar flow regime	Size	Microparticles, cells
Hydrodynamic filtration	Laminar flow regime	Size	Microparticles
Bifurcation	Laminar flow	Size, shape	Blood
Filtration obstacles	Diffusion and obstacles	Size	Blood
Lateral displacement	Obstacle array	Size	Particles (0.8, 0.9, 1.0 mm) DNA (61 kbp, 158 kbp)
Brownian ratchet	Diffusion and obstacles	Size	DNA
Hydrophoretic separation	Pressure gradient from slanted obstacles	Size	Microparticles
Entropic trap array	Dams and electric field	Size	DNA
Repulsion array	Dams, electric double layers	Charge to size ratio	Proteins
Free-flow electrophoresis	Homogeneous electric field	Charge to size ratio	Proteins, amino acids
Free-flow isoelectric focusing	pH gradient	Isoelectric point	Proteins and cells
Magnetophoresis	Inhomogeneous magnetic field	Size, magnetisation	Magnetic particles, cells
Dielectrophoresis	Inhomogeneous electric field	Size, polarisability	Microparticles, cells
Acoustophoresis	Acoustic pressure	Size, density, compressibility	Microparticles, cells
Optical lattice	Optical force	Size, refractive index	Microparticles, cells
Sedimentation	Gravity	Density, size	Microparticles, droplets

## 1.5 Our approach

In this study, in order to separate multiscale particle, comprehension about scale of context is a crucial process because particle physics and behaviour in small region are absolutely diverse. The dual multiscale particles are separated with pore array membrane based on a theoretical analysis on scale of context and practical experiments performed with DNA and blood which are placed in different scale ranges. Based on a study of appropriate particle separation method for specific particle dimension range, calculation and finite elements analysis (FEA) are accomplished to verify the separation system. In both experiments, MEMS

micromachining process to make free standing thin ( $< 1 \mu\text{m}$ ) membrane are used, and pore arrays of nano and micron diameter ranges are created on the membrane. Also electrophoresis (EP) function is combined to separate DNA, molecular particle on nano pore (anodized aluminium oxide, AAO) array membrane. On the other hand, dielectrophoresis (DEP) function is assembled to extract plasma, removing blood cells on the micro pore (photolithography  $\text{Si}_3\text{N}_4$ ) array membrane. In addition, PDMS microfluidics is integrated to produce a compact total system. The performance of particle separation system is verified and discussed by the experimental results, taking into account the pore size control, binary separation efficiency, purity (= selectivity), and recovery rate (= throughput).

## References

1. Hou, H.W., et al., *Microfluidic Devices for Blood Fractionation*. *Micromachines*, 2011. **2**(3): p. 319-343.
2. Nghiem, L.D., A.I. Schafer, and M. Elimelech, *Pharmaceutical retention mechanisms by nanofiltration membranes*. *Environ Sci Technol*, 2005. **39**(19): p. 7698-705.
3. Khan, F.I. and A.K. Ghoshal, *Removal of Volatile Organic Compounds from polluted air*. *Journal of Loss Prevention in the Process Industries*, 2000. **13**(6): p. 527-545.
4. Adin, A. and M. Elimelech, *Particle filtration for wastewater irrigation*. *Journal of irrigation and drainage engineering*, 1989. **115**(3): p. 474-487.
5. Che, G.L., et al., *Carbon nanotubule membranes for electrochemical energy storage and production*. *Nature*, 1998. **393**(6683): p. 346-349.
6. Wheaton, F.W., *Aquacultural engineering*. 1993: Krieger Publishing Company.
7. Weibel, D.B. and G.M. Whitesides, *Applications of microfluidics in chemical biology*. *Curr Opin Chem Biol*, 2006. **10**(6): p. 584-91.
8. Dittrich, P.S. and A. Manz, *Lab-on-a-chip: microfluidics in drug discovery*. *Nat Rev Drug Discov*, 2006. **5**(3): p. 210-8.
9. Unger, M.A., et al., *Monolithic microfabricated valves and pumps by multilayer soft lithography*. *Science*, 2000. **288**(5463): p. 113-6.
10. Pierre Buckens. Available from: <http://www.buckens.com/PacSci/partcntfr.htm>.
11. Oosterbroek, R.E., *Modeling, design and realization of microfluidic components*. 1999, Universiteit Twente.
12. *Importance of Filter in Microbiology history*: , in *Microbiology ONLINE*.

13. *Various Types of Water Purification Methods.* Available from: <http://www.roengineering.com.hk/Eng/tech.htm>.
14. Eijkel, J.C. and A. Van Den Berg, *Nanofluidics: what is it and what can we expect from it?* Microfluidics and Nanofluidics, 2005. **1**(3): p. 249-267.
15. Pu, Q.S., et al., *Ion-enrichment and ion-depletion effect of nanochannel structures.* Nano Letters, 2004. **4**(6): p. 1099-1103.
16. Giddings, J.C., *Unified separation science.* 1991.
17. Han, J. and H.G. Craighead, *Separation of long DNA molecules in a microfabricated entropic trap array.* Science, 2000. **288**(5468): p. 1026-9.
18. Strick, T., et al., *Twisting and stretching single DNA molecules.* Prog Biophys Mol Biol, 2000. **74**(1-2): p. 115-40.
19. Muthukumar, M. and A. Baumgartner, *Effects of Entropic Barriers on Polymer Dynamics.* Macromolecules, 1989. **22**(4): p. 1937-1941.
20. Turner, S.W., M. Cabodi, and H.G. Craighead, *Confinement-induced entropic recoil of single DNA molecules in a nanofluidic structure.* Phys Rev Lett, 2002. **88**(12): p. 128103.
21. Gyurcsányi, R.E., *Chemically-modified nanopores for sensing.* TrAC Trends in Analytical Chemistry, 2008. **27**(7): p. 627-639.
22. Fu, J., et al., *A patterned anisotropic nanofluidic sieving structure for continuous-flow separation of DNA and proteins.* Nat Nanotechnol, 2007. **2**(2): p. 121-8.
23. Woolley, A.T. and R.A. Mathies, *Ultra-High-Speed DNA Fragment Separations Using Microfabricated Capillary Array Electrophoresis Chips.* Proceedings of the National Academy of Sciences of the United States of America, 1994. **91**(24): p. 11348-11352.
24. Min, S.K., et al., *Theoretical Design of Nanomaterials and Nanodevices: Nanolensing, Supermagnetoresistance, and Ultrafast DNA Sequencing.*

- Journal of Physical Chemistry C, 2011. **115**(33): p. 16247-16257.
- 25. Min, S.K., et al., *Fast DNA sequencing with a graphene-based nanochannel device*. Nat Nanotechnol, 2011. **6**(3): p. 162-5.
  - 26. Lagerqvist, J., M. Zwolak, and M. Di Ventra, *Fast DNA sequencing via transverse electronic transport*. Nano Lett, 2006. **6**(4): p. 779-82.
  - 27. TAKAHASHI, H. and M. NAGAYAMA, *The determination of the porosity of anodic oxide films on aluminium by the pore-filling method*. Corrosion Science, 1978. **18**: p. 911-925.
  - 28. Mark, D., et al., *Microfluidic lab-on-a-chip platforms: requirements, characteristics and applications*. Chem Soc Rev, 2010. **39**(3): p. 1153-82.
  - 29. Yamada, M., M. Nakashima, and M. Seki, *Pinched flow fractionation: continuous size separation of particles utilizing a laminar flow profile in a pinched microchannel*. Anal Chem, 2004. **76**(18): p. 5465-71.
  - 30. Yang, X., et al., *Integrated separation of blood plasma from whole blood for microfluidic paper-based analytical devices*. Lab Chip, 2012. **12**(2): p. 274-80.
  - 31. Cima, M.J., *Microsystem technologies for medical applications*. Annu Rev Chem Biomol Eng, 2011. **2**: p. 355-78.
  - 32. Nakashima, Y., S. Hata, and T. Yasuda, *Blood plasma separation and extraction from a minute amount of blood using dielectrophoretic and capillary forces*. Sensors and Actuators B-Chemical, 2010. **145**(1): p. 561-569.
  - 33. Lange, K., B.E. Rapp, and M. Rapp, *Surface acoustic wave biosensors: a review*. Anal Bioanal Chem, 2008. **391**(5): p. 1509-19.
  - 34. Bhagat, A.A., et al., *Microfluidics for cell separation*. Med Biol Eng Comput, 2010. **48**(10): p. 999-1014.
  - 35. Pamme, N., *Continuous flow separations in microfluidic devices*. Lab Chip,

2007. **7**(12): p. 1644-59.
36. Kersaudy-Kerhoas, M., R. Dharival, and M.P. Desmulliez, *Recent advances in microparticle continuous separation*. IET Nanobiotechnol, 2008. **2**(1): p. 1-13.
  37. Eijkel, J.C. and A. van den Berg, *Nanotechnology for membranes, filters and sieves. A series of mini-reviews covering new trends in fundamental and applied research, and potential applications of miniaturised technologies*. Lab Chip, 2006. **6**(1): p. 19-23.
  38. Tsutsui, H. and C.M. Ho, *Cell Separation by Non-Inertial Force Fields in Microfluidic Systems*. Mech Res Commun, 2009. **36**(1): p. 92-103.
  39. Kulrattanarak, T., et al., *Classification and evaluation of microfluidic devices for continuous suspension fractionation*. Adv Colloid Interface Sci, 2008. **142**(1-2): p. 53-66.
  40. Dimov, I.K., et al., *Stand-alone self-powered integrated microfluidic blood analysis system (SIMBAS)*. Lab Chip, 2011. **11**(5): p. 845-50.
  41. Gorkin, R., et al., *Centrifugal microfluidics for biomedical applications*. Lab Chip, 2010. **10**(14): p. 1758-73.
  42. Toner, M. and D. Irimia, *Blood-on-a-chip*. Annu Rev Biomed Eng, 2005. **7**: p. 77-103.
  43. Sia, S.K. and G.M. Whitesides, *Microfluidic devices fabricated in poly(dimethylsiloxane) for biological studies*. Electrophoresis, 2003. **24**(21): p. 3563-76.

## 2 Part I : Separation of molecular scale particles

Separation and filtration of biomolecules using the nano-porous membrane can play central roles to many analytical and purification process. Gel electrophoresis, for example, is used to sort charged biopolymers according to weights for interrogating the molecular composition of a certain mixture. Proteins that cause a disease can be removed through a blood filtration from a patient. DNA purification can be achieved through a size specific separation and collection after cell lysis [1, 2]. Among various applications, the nano-pore based translocation of ssDNA is a vital issue because of their utility in fast DNA sequencing [3-5]. The idea is to electrophoretically drive negatively charged nucleotides into a nano-pore and identify each constituent nucleotide by monitoring currents [5] while the DNA molecules reside within the pore.

For efficient biomolecule separation based on nano-porous membrane, some of the key properties that materials with controlled pore diameter, length and surface chemistry are required. However, commercially available nano-porous membranes possess pore size-cutoff properties and low transport rates since they generally have broad size distributions and relatively large thickness values. Anodized aluminum oxide (AAO) membrane has the potential to be a good nano-porous membrane element for biomolecule separation because of its very high pore density, e.g., up to  $24 \times 10^{20}$  pores/cm<sup>2</sup>, its relative uniform pore sizes, as well as the availability of the sub 100 nm pores [6].

On-chip integration is crucial to high-quality molecular separation and provides an additional benefit of automated handling in a portable format [7]. In a normal fabrication process for such a chip device, commercially available AAO membranes are directly ‘attached’ to microfluidic components [8]. However, there have been few techniques developed for the direct integration of AAO through a unified fabrication procedure. Among the many advantages afforded via such seamless integration is the availability of thin membrane (e.g. 0.5  $\mu\text{m}$ ), which provide a short pore channel for efficient transport and safe handling compared with prefabricated AAO membranes of a certain thickness (e.g., > 100  $\mu\text{m}$ ).

Herein we report on an on-chip integrated AAO nano-porous membrane device with a combined configuration and fabrication procedure. The AAO was directly formed on a silicon substrate in a cleanroom fabrication process, enabling the precise control of the membrane thickness and pore diameter. The characteristics of DNA transport through the pores driven by an electric field were investigated. It was demonstrated that while free aptamers (i.e. single-stranded DNA, from here on termed ssDNA) easily pass through the pores, whereas, aptamer-protein complexes are effectively prevented from such translocation due to their size and electrokinetic properties.

## 2.1 Concept and applications

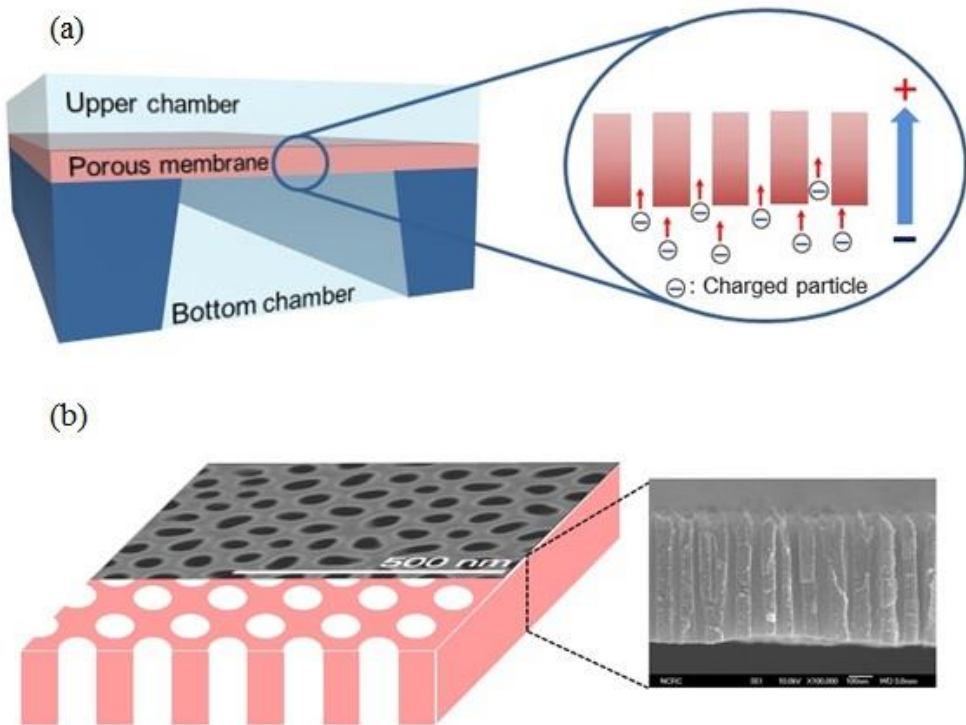


Figure 2-1. (a) Device concept. Only negatively charged molecules can pass through the nanoporous membrane when an electric field is applied (electrophoresis, EP), (b) SEM image of thin membrane of AAO

Figure 2-1 (a) shows the concept of lab-on-a-chip (LOC) bio-molecular separation device. The device is composed of three components. AAO nano-porous membrane (Figure 2-1 (b)) integrated on the silicon substrate, upper microfluidic chamber and bottom microfluidic chamber. AAO nano-porous membrane is assembled into two microfluidic chambers. This device serves as a size exclusive filter like a sieve. Charged molecules smaller than the size of the pores in the mixed samples are driven by electrostatic force and transported via the porous alumina membrane. When, for

example, an electric field is applied across the membrane, negatively charged biomolecules such as single strand DNA aptamer, RNA will migrate toward the anode, and eventually permeates the membrane through the pores. However, molecules larger than the pore size or positively charged molecules are not allowed to be transported through the membrane being blocked by the relatively small size of pores.

In this study, the interaction between pore-particle sizes is a critical issue for size-exclusive separation. The AAO diameter is controlled by fabrication conditions such as pore reduction time and etchant concentration. Also the driving force of molecular particles is an important matter considering the particle properties. For DNA separation, electrophoretic (EP) force is chosen to drive the negatively charged DNA. In this section, we are going to explain about AAO process and EP principle.

### 2.1.1 Anodized aluminum oxide (AAO)

In these days, AAO has been applied in a various nanotechnology. The reason is why AAO has good properties such as well-controllable pore size, periodicity and density distribution between pores. The traditional anodization process the organization of the pores were discreetly disordered. However, two-step anodization process made the well-ordered hexagonal pore formation [9]. These well-regulated macroscopic parameters dictated the resulting nano scale structure that is formed in the AAO layer, thus producing a nano array that can be used in many nanotechnology applications.

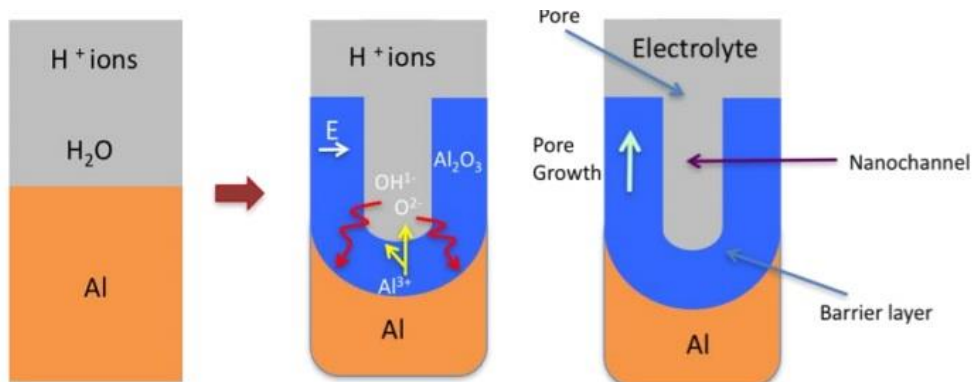


Figure 2-8. Schematic of the pore formation mechanism in an acidic electrolyte [10]

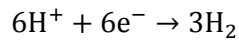
In the first stages of the anodization process,  $Al^{3+}$  ions move from the metal across the metal/oxide interface into the creating oxide layer [11]. Meanwhile  $O^{2-}$  ions are generated from water at the oxide/electrolyte interface mobile into the oxide layer. During this stage approximately 70% of the  $Al^{3+}$  ions and the  $O^{2-}$  ions contribute to the formation of the barrier oxide layer [12], the remaining  $Al^{3+}$  ions are dissolved into the electrolyte. This condition has been shown to be the prerequisite for porous oxide growth, in which the Al-O bonds in the oxide lattice break to release  $Al^{3+}$  ions

[13]. Through the oxide formation the barrier layer continually regenerates with further oxide growth and converts into a semi-spherical oxide layer of constant thickness that forms the pore bottom as shown in Figure 2-2.

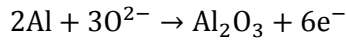
During the process of the porous oxide layer the anodic Al dissolution reaction is presented by



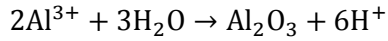
and the resulting reaction at the cathode produces hydrogen gas:



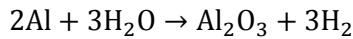
Anode reactions taking place at the metal/oxide boundary (Oxygen anions react with Al)



At the oxide/electrolyte boundary (Al cations react with the water molecules)



Sum of the separate reactions at electrode (Overall anodization of Al equation)



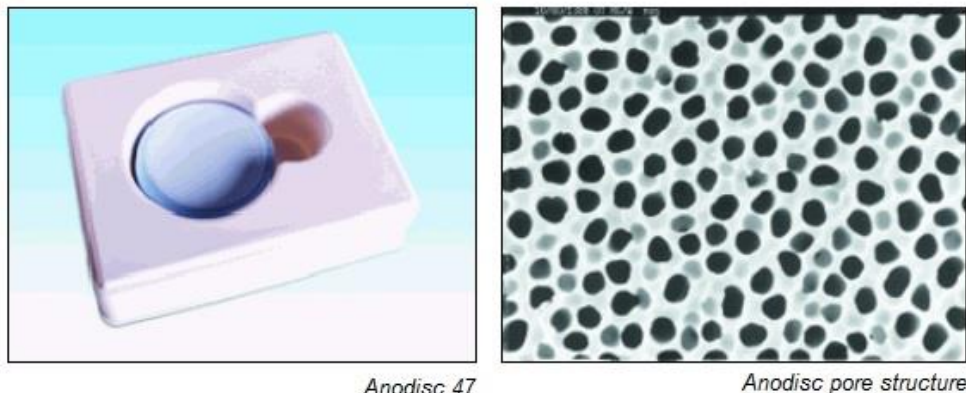


Figure 2-9. Anopore Inorganic Membranes (Anodisc, Whatman) [14]

Table 2-3. Typical Data – Anopore Inorganic Membranes (Anodisc, Whatman) [14]

Typical Data - Anopore Inorganic Membranes			
	Anodisc 13	Anodisc 25	Anodisc 47
Average membrane thickness	60 µm	60 µm	60 µm
Membrane diameter	13 mm	21 mm	43 mm
Membrane type	Anopore aluminum oxide	Anopore aluminum oxide	Anopore aluminum oxide
Support ring material	None	Polypropylene	Polypropylene
Construction process	None	Thermal weld	Thermal weld
Protein adsorption	Low	Low	Low
Burst strength	65 to 110 psi	65 to 110 psi	65 to 110 psi
Maximum service temperature	400°C	40°C	40°C
Porosity	25 to 50%	25 to 50%	25 to 50%
Autoclavable	Yes	No	No
Refractive index	1.6	1.6	1.6

## 2.1.2 Electrophoresis (EP)

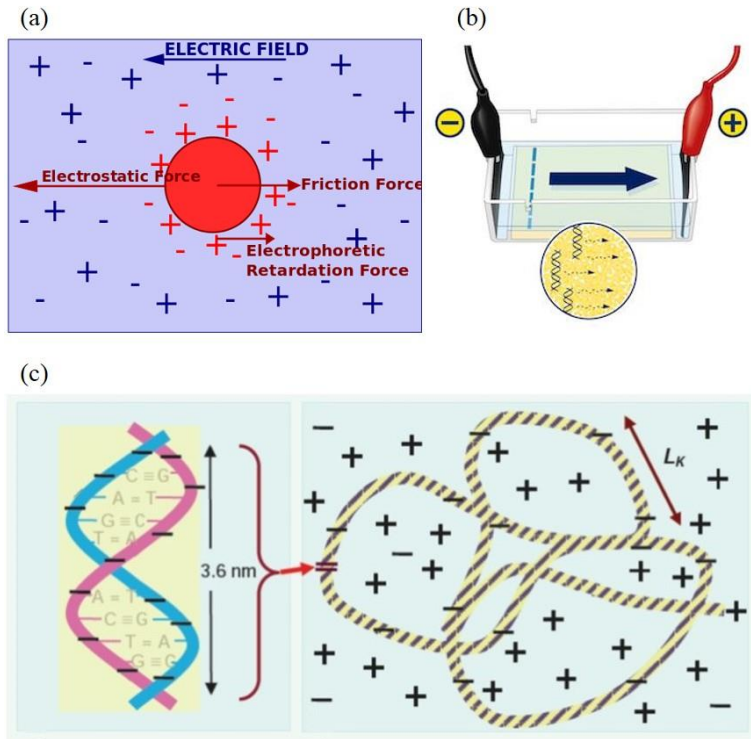


Figure 2-10. (a) concept of electrophoresis (EP) [15], (b) gel electrophoresis of DNA [16],  
(c) dsDNA and worm-like DNA [17]

In Figure 2-4. (a), electrophoresis is the motion of dispersed particles related to fluid under the influence of a spatially uniform electric field [18]. This electrokinetic phenomenon is ultimately caused by the presence of a charged interface between the particle surface and the surrounding fluid. It is the beginning for a number of analytical methods used in biochemistry for molecule separation by size, charge, or binding affinity. Gel electrophoresis in Figure 2-4. (b) is used to sort charged biopolymers according to weights for interrogating the molecular composition of a certain mixture [16]. Gel electrophoresis is a key technique in modern biology. First,

a gel is cast from agarose - a very pure form of agar, which is obtained from seaweed. At one end of the slab of gel are several small wells, made by the teeth of a comb that was placed in the gel before it set. A buffer solution is poured over the gel, so that it fills the wells and makes contact with the electrodes at each end of the gel. Ions in the buffer solution conduct electricity. The DNA fragments are mixed with a small volume of loading dye. This dye is dissolved in a dense sugar solution, so that when it is added to the wells, it sinks to the bottom, taking the DNA with it. An electrical potential is applied across the gel. Phosphate groups give the DNA fragments a negative electrical charge, so that the DNA migrates through the gel towards the positive electrode. Small fragments move quickly through the porous gel — larger fragments travel more slowly. In this way the pieces of DNA are separated by size. The loading dye also moves through the gel, so that the progress of the electrophoresis can be seen. After electrophoresis, the gel is stained with a harmless dye to reveal the DNA.

In conclusion, in order to separate DNA in this study, EP is used to drive DNA from (-) negative electrode to (+) positive electrode because DNA is usually negatively charged. Instead of gel electrophoresis, MEMS device and microfluidics is used to make electric field and electrophoretic force.

## 2.2 Theoretical background

Particle-pore size interaction is the most important issue in molecular separation with nano pores. The effective pore size is determined by physical AAO diameter and electrical double layers (EDL) thickness. The AAO diameter is controlled by the fabrication settings. On the other hand, EDL thickness can be changed depending on the conditions of buffer solution. Especially, ionic concentration of buffer is controlled in this study. Thus, after estimating the biomolecular sizes and applying forces, the effective pore size will be discussed.

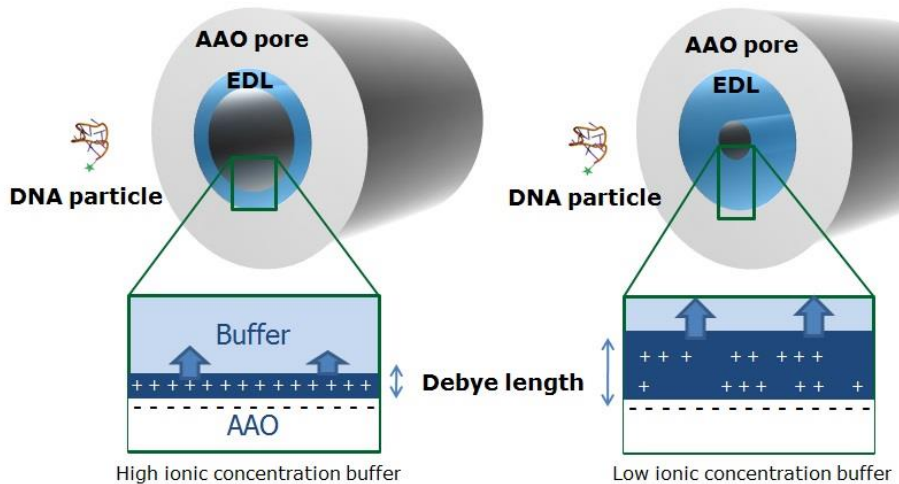


Figure 2-11. Concept of effective pore size. The effective pore size is composed of AAO pore diameter and electrical double layer thickness (EDL). EDL thickness is affected by buffer concentrations.

The biomolecule size could be calculated by its molecular weight (g/mole). For instance, FITC, aptamer, thrombin, and aptamer-thrombin complex are used in this study. The molecular weights of these biomolecules are 332, 4 K, 36 K, and 44 K respectively. Among the biomolecules, aptamer which is 150mer DNA would be calculated as the radius of gyration is around 1 nm. The size of aptamer-thrombin complex is about 10 nm. Detail calculation process will be followed next section.

The forces on the charged biomolecules in nanochannel are electrophoretic (EP) and hydrodynamic drag forces. Each force is described as below.

$$F_{ep} = qE_e \quad (2.1)$$

$$F_{drag} = 6\pi R\mu u_{ep} \quad (2.2)$$

where  $F_{ep}$  is electrophoretic force,  $F_{drag}$  is hydrodynamic drag force,  $E_e$  is electric field,  $R$  is diameter of nano pore,  $u_{ep}$  is velocity of the charged biomolecules,  $\mu$  is dynamic viscosity. This size difference affects different drags and electrophoretic velocity in electrophoresis Eq. (2.1). The second one is the role of pores. There is a porous membrane which has effective pores as a sieve.

$$F_{ep} = F_{drag} \quad (2.3)$$

$$u_{ep} = \frac{qE_e}{6\pi R\mu} \quad (2.4)$$

The membrane is a size selective filter. Even though the physical size of the pore is large ( $\sim 38$  nm), the nano channel (500 nm) is negatively charged in the given

condition (higher pH than iso-electric point of  $\text{Al}_2\text{O}_3$ ), acting as a strong barrier against the transport. In addition, zeta potential of molecules in the experimental configuration also helps the separation.

### 2.2.1 Size of molecules

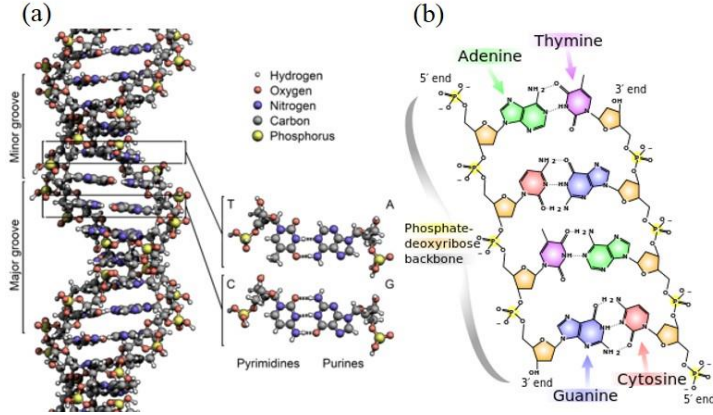


Figure 2-12. DNA structures [19]. (a) The structure of the DNA double helix, (b) chemical structure of DNA.

DNA is a long polymer made from repeating units called nucleotides [20]. The structure of DNA of all species comprises two helical chains each coiled round the same axis, and each with a pitch of  $34 \text{ \AA}$  (3.4 nanometers) and a radius of  $10 \text{ \AA}$  (1.0 nanometer) [21]. While every repeating unit is too small, DNA polymers can be large molecules having millions of nucleotides. For instance, the largest human chromosome, chromosome number 1, consists of approximately 220 million base pairs and is 85 nm long [22].

The DNA double helix in solution has a shape very different from the classical straight DNA configuration in which this molecule is famously depicted. In reality, DNA is a flexible polymer subject to thermal fluctuations. A polymer is a long chain of similar repeated units, in which each unit is composed of many atoms. At equilibrium, the orientation between the different units is the same, but when subject to thermal fluctuations, the adjacent units differ in direction and are poorly correlated. This results in long molecules of DNA in solution behaving like a random coil.

A widely used measure for the characterization of the configuration of a polymer is the radius of gyration ( $R_G$ ), which measures the root-mean square distance of the collection of segments from their common center of mass, i.e.

$$R_G^2 = \frac{1}{N+1} \sum_{i=0}^N (r_i - r_{cm})^2 \quad (2.5)$$

where  $r_{cm}$  is the vector defining the coordinates of the center of mass, and  $r_i, r_j$  being the mass and the position of segment  $i, j$ , respectively. The radius of gyration can be measured from particle scattering experiments [23].

All the functions of DNA depend on interactions with proteins. The protein interactions could be non-specific, or the protein could bind precisely to a single DNA sequence.

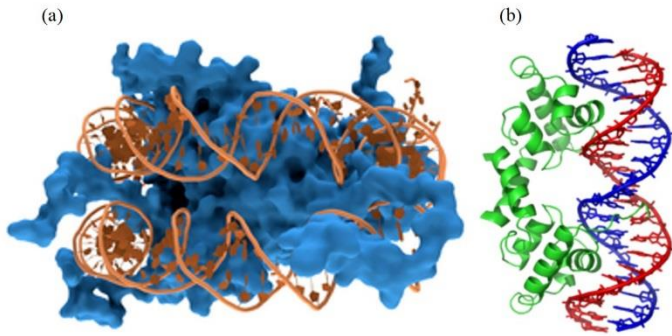


Figure 2-오류! 지정한 스타일은 사용되지 않습니다.13. (a) interaction of DNA with protein (histones), (b) lambda repressor helix-turn-helix transcription factor bound to its DNA target [19]

Structural proteins that bind DNA are well-understood examples of non-specific DNA-protein interactions [19]. Within chromosomes, DNA consists of complexes with structural proteins. The proteins organize the DNA to be a compact structure called chromatin. While in prokaryotes multiple types of proteins are involved, in eukaryotes these structures involve DNA binding to a complex of small basic proteins called histones. The histones make a disk-shaped complex, a nucleosome, which has two complete turns of double-stranded DNA wrapped around its surface. These non-specific interactions are made through basic residues in the histones forming ionic bonds to the acidic sugar-phosphate backbone of the DNA, and are consequently independent of the base sequence. Chemical changes of these basic amino acid residues contain methylation, phosphorylation and acetylation. These chemical modifications rework the strength of the interaction between the DNA and the histones, making the DNA more or less nearby to transcription factors and changing the rate of transcription. Other non-specific DNA-binding proteins in chromatin comprise the high mobility group proteins, which fix to bent or distorted

DNA. These proteins are essential in bending arrays of nucleosomes and positioning them into the larger structures that consist of chromosomes.

In this study, short 15-mer ssDNA, aptamer, is used to verify the relationship between effective pore size and ionic strength. Also complex of thrombin (coagulation protein, 36 kDa) and thrombin aptamer (4 kDa, 5'-FITC-GGT TGG TGT GGT TGG-3') [24] is used to confirm the size exclusive biomolecular separation.

### 2.2.2 Electrical double layers (EDL)

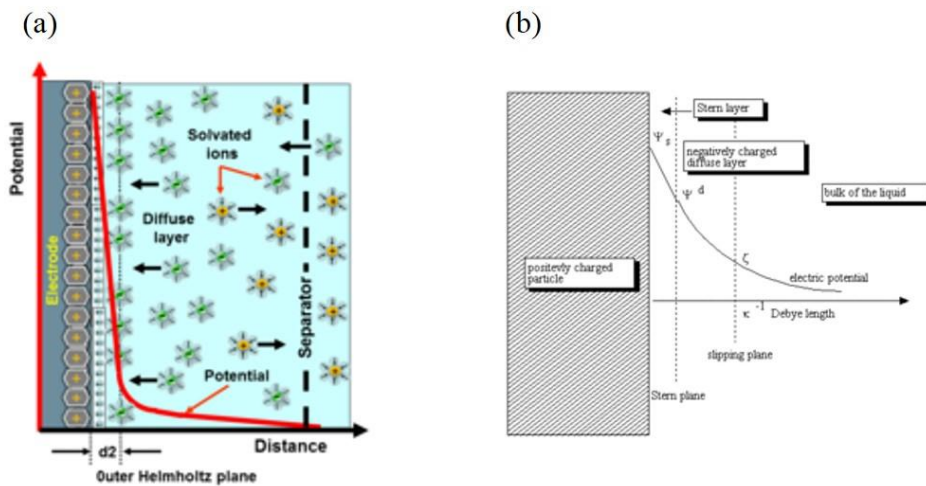


Figure 2-오류! 지정한 스타일은 사용되지 않습니다. 14. Illustration of EDL. (a) simplified illustration of the potential development in the area and in the further course of a Helmholtz double layer, (b) mathematical description of interfacial EDL

Electrical double layer (EDL) is a structure that appears on the surface of an object when it is exposed to a fluid. The object would be a solid particle, a gas bubble, a

liquid droplet, or a porous body. The EDL consists of two parallel layers of charge surrounding the object. The first layer, the surface charge (either positive or negative), covers ions adsorbed onto the object due to chemical interactions. The second layer consists of ions attracted to the surface charge via the Coulomb force, electrically screening the first layer. The second layer is loosely related with the object. It is made of free ions that transfer in the fluid under the effect of electric attraction and thermal motion rather than being anchored. It is also called the "diffuse layer".

EDL is most apparent in systems with a large surface area to volume ratio, such as colloid or porous bodies with particles or pores (respectively) on the scale of micrometers to nanometers. However, EDL is important to other phenomena, such as the electrochemical behavior of electrodes. EDL plays a fundamental role in many everyday substances. For instance, milk exists only because fat droplets are covered with a EDL that prevent their coagulation into butter. EDLs exist in practically all heterogeneous fluid-based systems, such as blood, paint, ink and ceramic and cement slurry.

In this study, AAO is used for molecular particle filter in liquid solution. The effective pore size is determined by the sum of physical pore size and EDL thickness inside AAO pore. In an electrolyte or a colloidal suspension, the Debye length is usually denoted with symbol  $\lambda_D$  [25],

$$\lambda_D = \sqrt{\frac{\varepsilon_r \varepsilon_0 k_B T}{2N_A e^2 I}} \quad (2.1)$$

where,  $I$  is the ionic strength of the electrolyte, and here the unit should be mole/m<sup>3</sup>,  $\epsilon_0$  is the permittivity of free space,  $\epsilon_0$  is the dielectric constant,  $k_B$  is the Boltzmann constant,  $T$  is the absolute temperature in kelvins,  $N_A$  is the Avogadro number,  $e$  is the elementary charge.

Among the parameters,  $I$  can be changed by buffer concentration. This means the buffer concentration change makes the difference in EDL thickness and the effective pore size. In short, changing the buffer concentration can decide whether the molecules can pass AAO filter or not.

### 2.3 Materials and methods

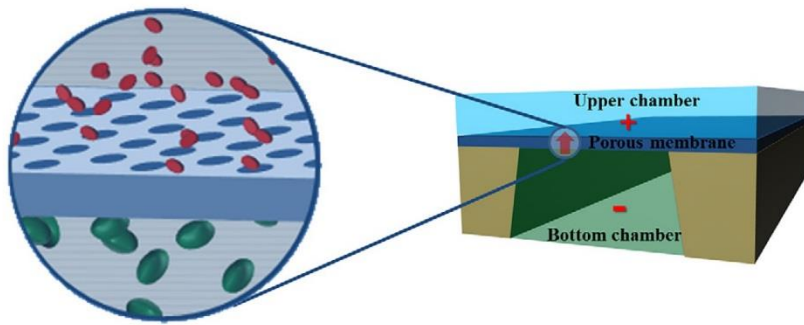


Figure 2-9. Schematic of molecular filtration. Only negatively charged molecules can pass through the nanoporous membrane when an electric field is applied.

In Figure 2-9, the system is composed of molecule (DNA and protein) sample and AAO nanoporous MEMS filter. Using PDMS microchannel, the sample solution with molecules and buffer fills the PDMS channels and chambers. Figure 2-10 also represents the experimental setup for molecular separation. In this section, we describe the sample solution preparation, AAO MEMS filter fabrication process.

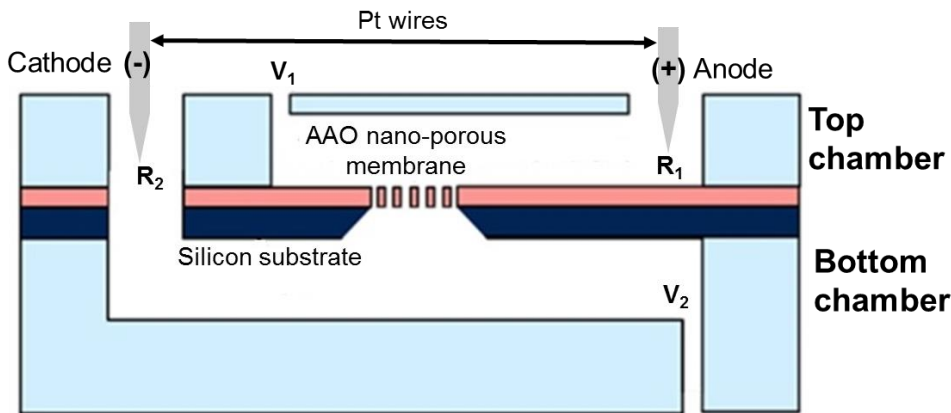


Figure 2-10. Experimental set-up of AAO nanoporous membrane

### 2.3.1 Molecular sample preparation

In Figure 2-10, two Pt electrodes are placed on each reservoir to perform the electrophoretic experiment. TAE buffer (1 ×, containing 40 mM Tris base, 40 mM glacial acetic acid, and distilled water, resulting in a pH of 7.4) is used to fill the upper chamber. Fluorescein isothiocyanate (FITC)-tagged oligo ssDNA dissolved in 1 × TAE buffer was then injected into the bottom chamber through R<sub>1</sub>, as shown in Figure 2-10. Due to capillary effects and the venting holes, injection is achieved without any external pressure source applied, such as the use of pneumatic apparatus.

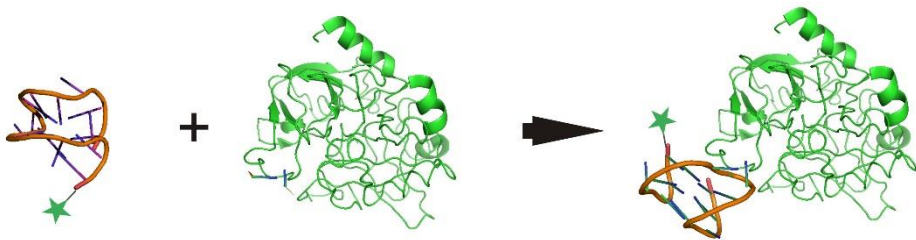


Figure 2-15. Aptamer interaction with Thrombin. Binding of the protein Thrombin to a fluorescently labeled aptamer [26].

To verify the size exclusive bimolecular separation, we use a complex of thrombin (coagulation protein, 36 kDa) and thrombin aptamer (4 kDa, 5'-FITC-GGT TGG TGT GGT TGG-3') [24] in Figure 2-11. Thrombin and FITC-tagged (0.33 kDa) thrombin aptamer are incubated in an aptamer binding buffer (20 mM Tris-acetate, pH =7.4, 140 mM NaCl, 5 mM KCl, 1mM CaCl<sub>2</sub>, and 1 mM MgCl<sub>2</sub>) for 1 hour to make an aptamer-thrombin complex (ATC).

### 2.3.2 AAO fabrication process

Instead of conventional AAO from Al foil strip [14], the AAO is directly formed on a substrate in a cleanroom fabrication process, enabling the precise control of the membrane thickness and pore diameter [27].

Two-step anodizing process is used to form AAO on the silicon nitride substrate [9]. The process begins with deposition of 400 nm-thick film of silicon nitride (Si<sub>3</sub>N<sub>4</sub>) on 4 inch silicon wafer. Titanium (50 nm) and aluminum (1~2 μm) layer are subsequently deposited with e-gun evaporator (Maestech ZZS550-2/D, Korea).

Surface cleaning process is used with acetone in ultrasonic bath. Then, HF/HNO<sub>3</sub>/HCl/H<sub>2</sub>O (1:10:20:69) is used to remove the surface thin Al<sub>2</sub>O<sub>3</sub> layer. After washing in D.I water, heat treatment is done in 4~500 °C N<sub>2</sub> condition (Seoul Electronics SMF-800, Korea). This step is very important in AAO pore size control, because the grain size of Al affected on the pore diameter and the pores distance [28]. In addition, electropolishing with HClO<sub>4</sub>/C<sub>2</sub>H<sub>5</sub>OH (1:3) is applied to reduce the surface roughness for 10 min. The anodizing process is carried out with the holder, which is made by Kyounghan Jung (Figure 2-12). The holder consists of cathode (top black line) and anode (bottom red line) electrodes (in Figure 14 (b)), two acryl plates, and wafer packing O-ring. Using the holder, two-step anodizing process is conducted to make AAO on the substrate [9]. The first anodizing process is carried out in 0.3 M oxalic acid (H<sub>2</sub>C<sub>2</sub>O<sub>4</sub>) at 40 V (Agilent Technologies, N5771A, System DC Power Supply) to render a seed template. The voltage is preciously controlled by the program in Figure 2-12 (b). A mixture of 6 w.t..% phosphoric acid (H<sub>3</sub>PO<sub>4</sub>) and 8 w.t..% chromic acid (H<sub>2</sub>CrO<sub>4</sub>) at 60 w.t..% is used to selectively remove the first AAO layer and expose the seed template [29]. Well-aligned vertical and periodic pores are formed by the second anodizing process under the same conditions as the first step.

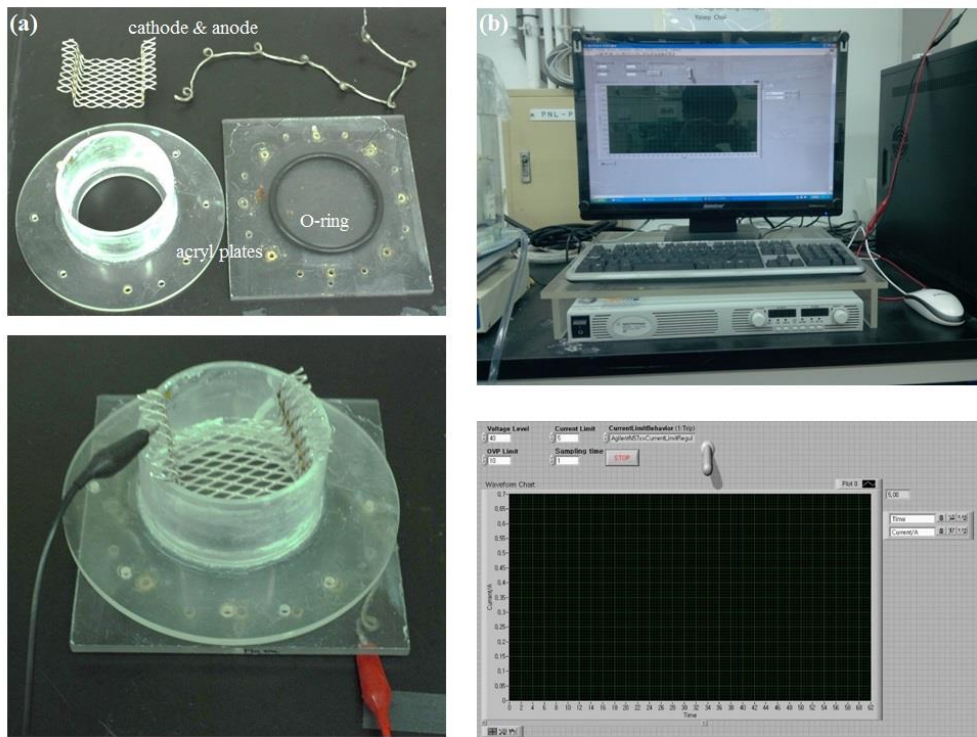


Figure 2-오류! 지정한 스타일은 사용되지 않습니다.16. The holder for anodizing process, (a) cathode & anode, acryl plates and O-ring made by Kyounghan Jung, (b) AAO process equipment set-up assembly

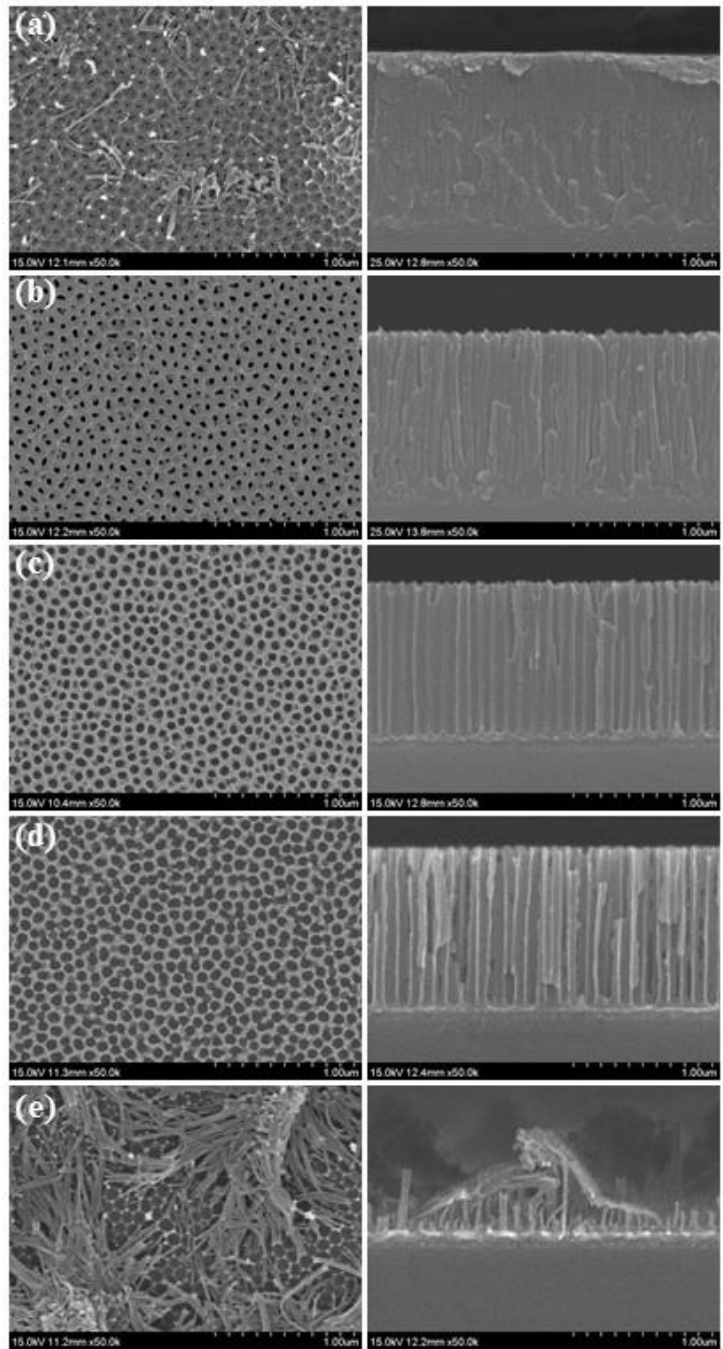


Figure 2-17. SEM images about pore widening w.r.t. etching time, (a) AAO ( $D_{pore} = \sim 28$  nm), (b) 10 min etching ( $D_{pore} = \sim 36$  nm), (c) 50 min etching  $D_{pore} = \sim 69$  nm), (d) 70 min etching ( $D_{pore} = \sim 85$  nm), (e) 90 min etching ( $D_{pore} = \sim 100$  nm)

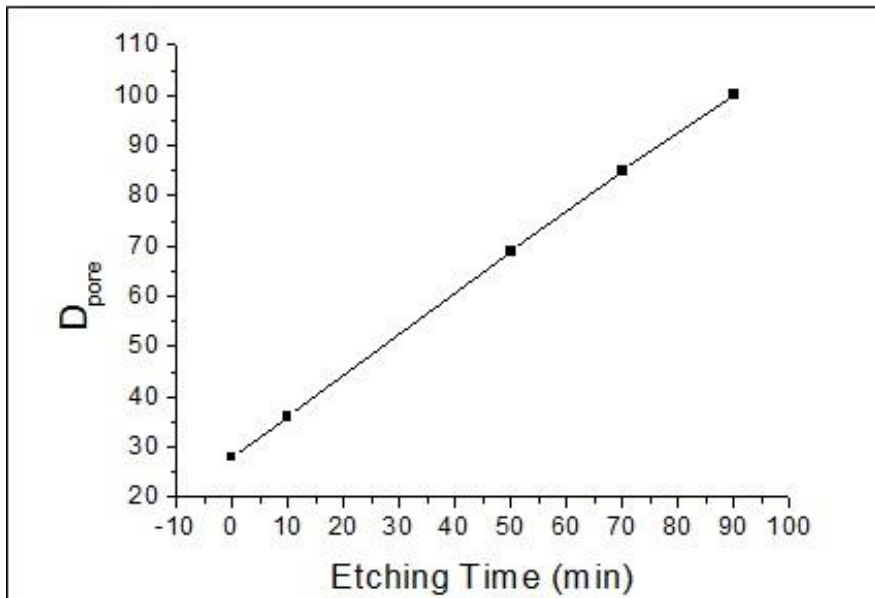


Figure 2-18. The relation between pore diameter ( $D_{\text{pore}}$ ) and etching time in 10 wt.%  $\text{H}_3\text{PO}_4$ , etch rate = ~0.8 nm/min @ R.T.

Then, pore widening process is carried out in 10 wt.% phosphoric acid at room temperature. Figure 2-15 shows the pore widening result depending on etching time. After heat treatment Al layer in 400°C, AAO is prepared with ~28 nm pore diameter ( $D_{\text{pore}}$ ).  $D_{\text{pore}}$  is linearly increased with respect to the etching time Figure 2-14. The average etching rate is ~0.8 nm/min at R.T. Using pore widening process,  $D_{\text{pore}}$  could be made under 100 nm. Furthermore the pore becomes more uniform during the widening process because of the isotropic etching property.

Figure 2-15 shows the images of the AAO nanoporous membrane obtained via SEM. The AAO membrane is suspended on a selectively etched area of the silicon substrate (Figure 2-15 (a)). A magnified image (Figure 2-15 (b)) verifies the flatness and uniformity of the sample, and the thickness of the membrane is about 500 nm.

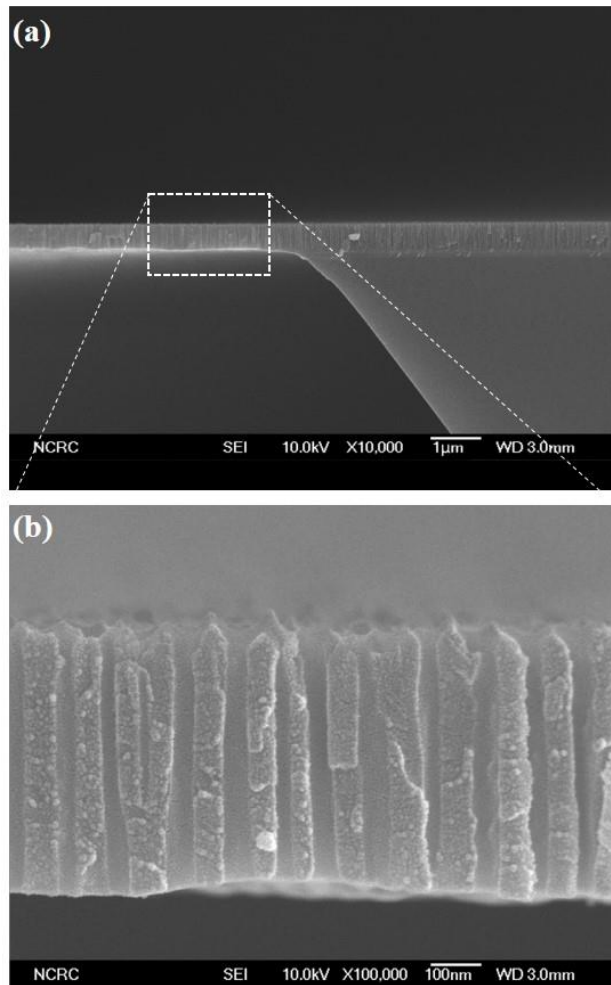


Figure 2-15. SEM images of AAO nanoporous membrane. (a) 500 nm thickness of free-standing AAO membrane on Si substrate. (b) magnified view of AAO membrane.

A backside image of the AAO membrane (Figure 2-16 (a)) shows that the pores are well opened and formed in a quasi-periodic arrangement. The average diameter of the vertically formed pores is 38.2 nm ( $\sigma = 6.64$  nm) and it is confirmed by image analysis with Vision Assistant (National Instrument, Figure 2-16 (b)).

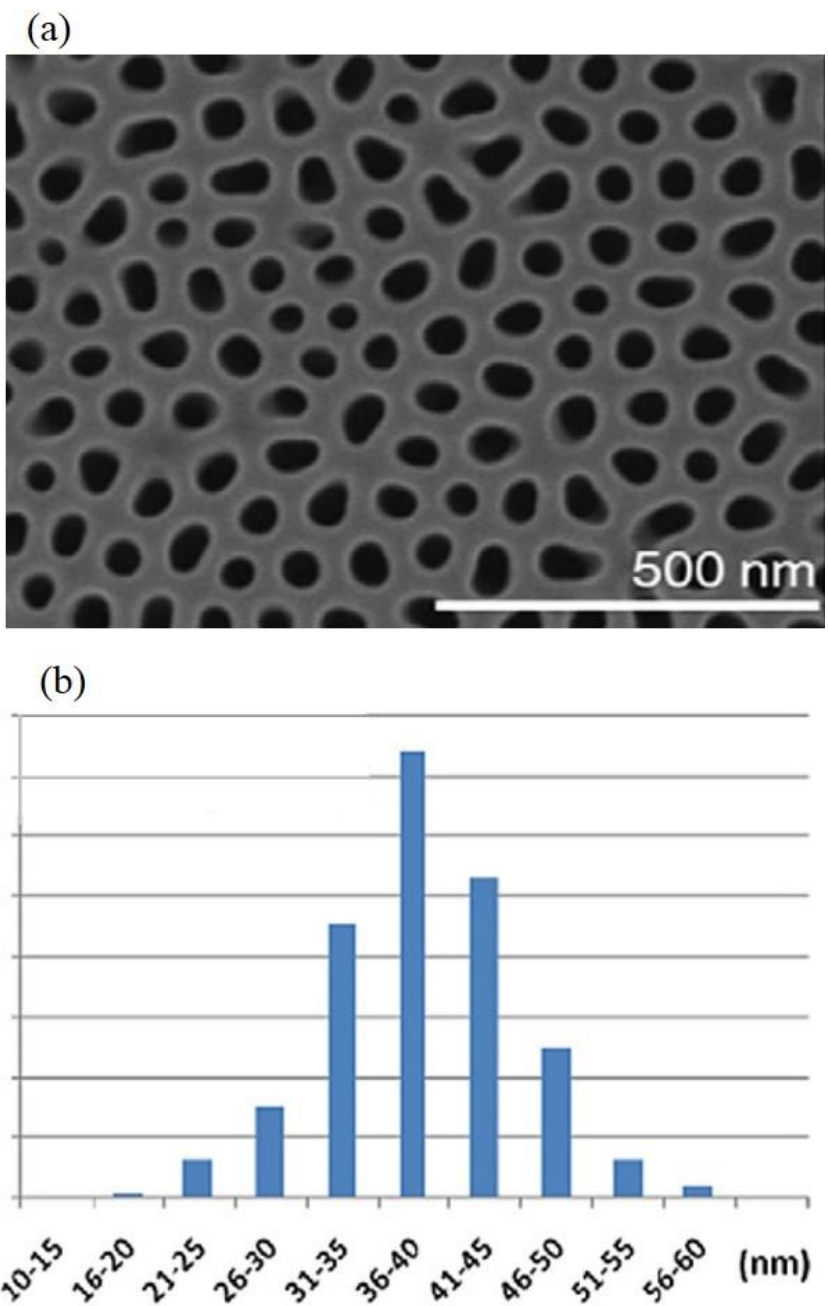


Figure 2-16. SEM images of AAO nanoporous membrane. (a) backside view of AAO membrane. (b) nano-pore size distribution.

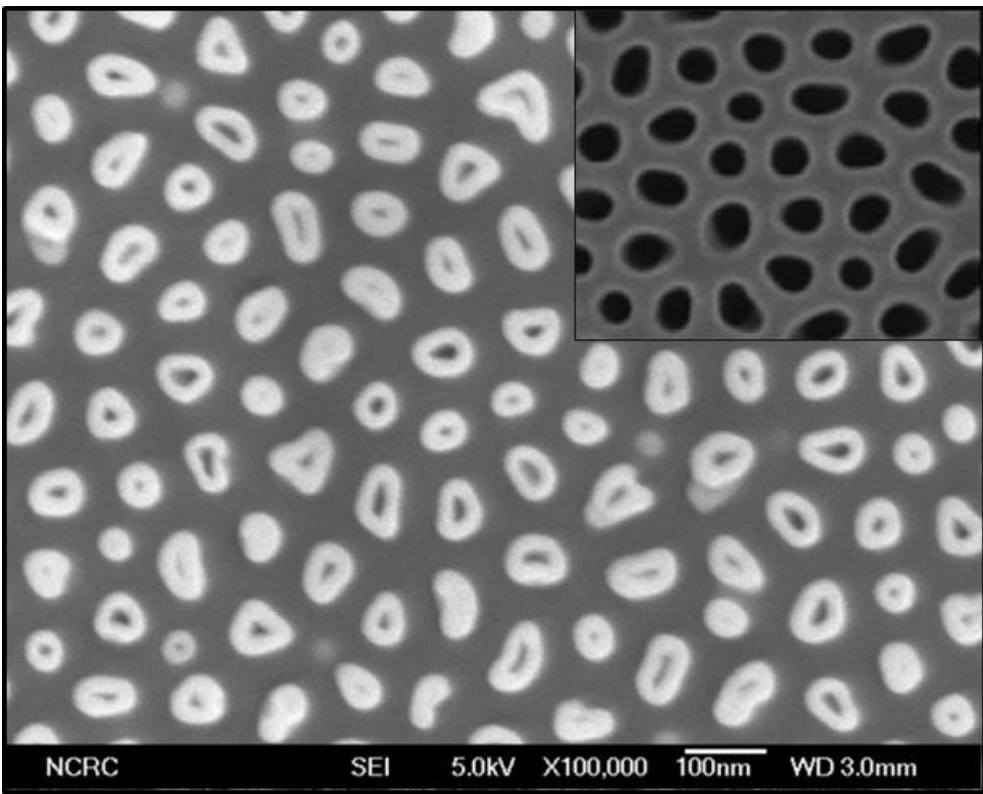


Figure 2-17. SEM images of Ru coated on AAO nanoporous membrane. Ru is deposited by ALD process. The AAO pore diameter is reduced from 38 nm to 13 nm.

AAO pore diameter is reduced by atomic layer deposition (ALD) process of Ru. Thin Ru layer is coated the nano porous AAO surface with conformal coverage, and average diameter of nano pore becomes 13 nm (Figure 2-17). 450 cycles of ALD process are used for pore reduction. The physical pore size could be controlled in nanometer range for biomolecular separation. This precise pore reductions is one of the key process in this study.

### 2.3.3 MEMS integration process

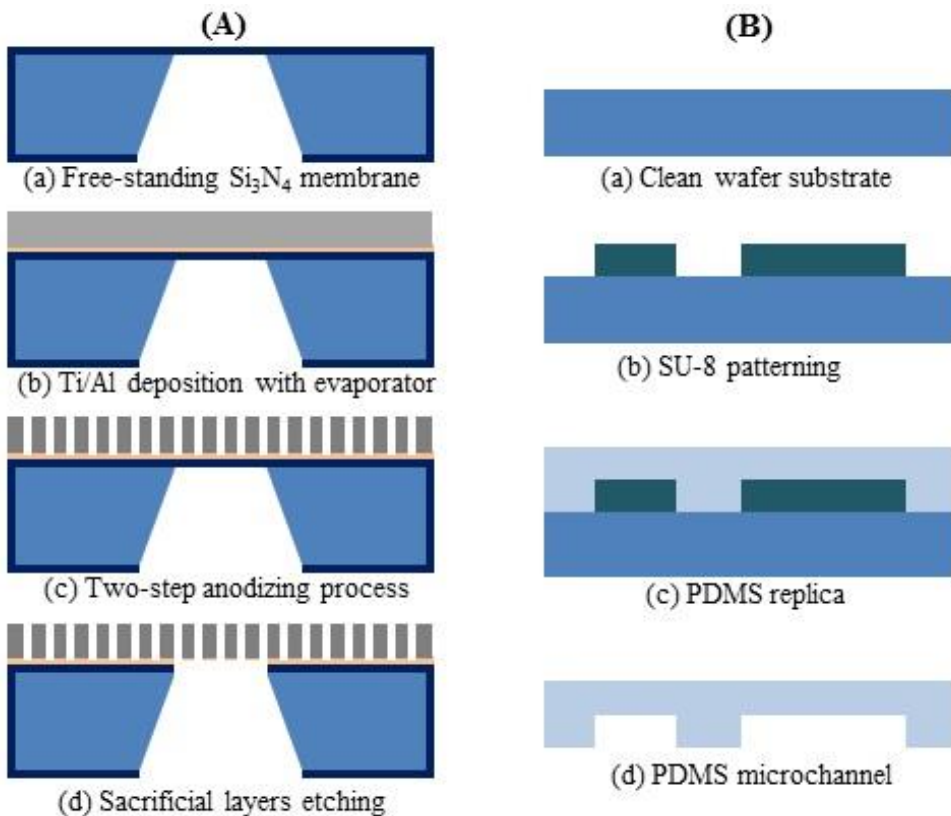


Figure 2-18. Fabrication process of a free-standing AAO nano-porous membrane (A), PDMS microchannel (B)

AAO nanoporous membrane is fabricated using the procedure outlined in Figure 2-18. The detail fabrication protocol is represented in Table 2-2. The fabrication process begins with deposition of a 400 nm-thick film of silicon nitride ( $\text{Si}_3\text{N}_4$ ) on (100) silicon substrate. The silicon nitride is then suspended by KOH anisotropic wet-etching of the substrate. Ti/Al layers are subsequently deposited by metal evaporation. A two-step anodizing process is used to form AAO on the silicon nitride membrane [9]. Then, a pore widening process is carried out in 10 wt.% phosphoric

acid at room temperature for 15 min (etch rate  $\approx$ 0.8 nm/min). Reactive-ion etching (RIE 80 plus, Oxford Instrument) is performed to remove the  $\text{Si}_3\text{N}_4$  layer. After the dry etching process, wet etching is performed to open the backside of AAO membrane by removing the Ti/AAO barrier layers.

PDMS microfluidic structure is fabricated as shown in Figure 2-18 B and is integrated with the AAO-silicon substrate for a single chip device. SU-8 (SU-8 100, MicroChem) mold with a thickness of 100  $\mu\text{m}$  were prepared by a typical photolithography process. PDMS chambers are replicated from the SU-8 mold.

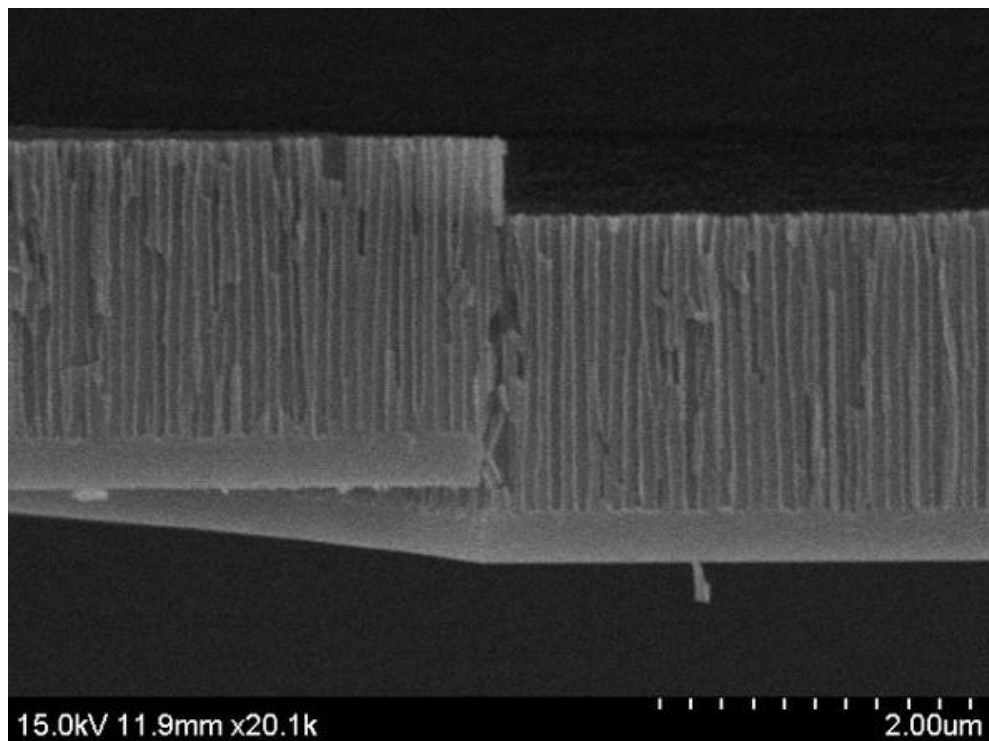


Figure 2-19. SEM image of AAO on the free-standing  $\text{Si}_3\text{N}_4$  membrane. The AAO membrane is broken, but it maintains the free standing shape.

Table 2-4. Detail fabrication protocol for AAO nano filter and microchannel

Process	Step
SPM cleaning	$\text{H}_2\text{SO}_4 + \text{H}_2\text{O}_2 = 4:1$ @120 °C for 5 min D.I. water for 10 min Rinse & dry for 10 min
$\text{Si}_3\text{N}_4$ deposition	LPCVD (Low Pressure Chemical Vapor deposition) 650 °C, DSC: 300 sccm, NH <sub>3</sub> : 100 sccm, 200 mTorr
AZ 1512 PR (photoresist)	with HDMS: 500 rpm/5 s, 2500 rpm/7s 500 rpm/ 5 s, 4000 rpm/ 35 s
Photolithography	Soft bake @ 95 °C for 90 s 60 s exposure @ 15mW Developing @ AZ 300 MIF : D.I. water = 1:6 for 90 s Hard bake @ 110 °C for 3 min
Dry etching with P-5000	$\text{Si}_3\text{N}_4$ etching RF 600 W, 100 mTorr, 30 G, 4000 Å/min $\text{CHF}_3$ 15 sccm, $\text{CF}_4$ 10 sccm, Ar 10 sccm, $\text{O}_2$ 8 sccm
KOH wet etching	40 w.t % (KOH : D.I.water) 80 °C for 10 hr Rinse in D.I. water without bubble and shower Manual N <sub>2</sub> gun dry carefully Bake 110 °C for 5 min
Ti/Al deposition with E-gun evaporator	Power 10 kW, N <sub>2</sub> gas Chamber pressure $\leq 5 \times 10^{-7}$ Torr 30 min (=0.5 μm) × 2 times = 1 μm

Process	Step
Dry etching with Oxford	Si <sub>3</sub> N <sub>4</sub> etching RF 100 W, 55 mTorr, CF <sub>4</sub> 50 sccm, O <sub>2</sub> 5 sccm etch rate = 1000 Å/min
Ti layer wet etching	(HF : D.I.water = 1 : 1000) @ RT Etch time < 10 s
SU-8 PR (photoresist) Photolithography - 50 µm thickness	Surface treatment with O <sub>2</sub> plasma 20 s 500 rpm/ 5 s, 2500 rpm/ 30 s Soft bake @ 95 °C for 60 min 17 s exposure @ 15mW Post exposure bake @ 100 °C for 6 min Developing @ SU-8 developer for 15 min Hard bake @ 110 °C for 1 min
PDMS molding (Polydimethyl siloxane) - Sylgard 184	DC-184A : DC-184B = 10:1 mixing for 15 min 1 <sup>st</sup> degassing for 30 min with vacuum chamber PDMS pouring to SU-8 mold 2 <sup>nd</sup> degassing for 30 min with vacuum chamber 70 °C for 50 min

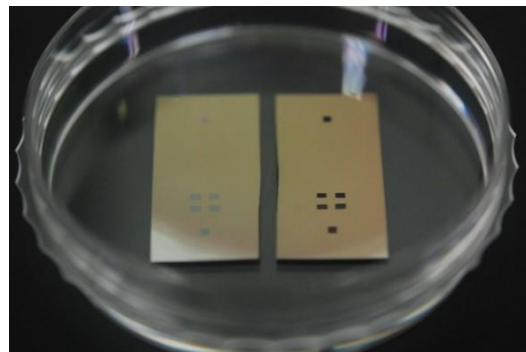


Figure 2-20. Images AAO membrane in fabrication steps, before (left) and after (right) sacrificial layers etching.

In free-standing AAO membrane process, sacrificial layers etching step (Figure 2-18A (d)) is a crucial work to make a DNA separation filter. The sacrificial layers ( $\text{Si}_3\text{N}_4/\text{Ti}/\text{AAO}$  barrier) should be perfectly removed, and then the small size of DNA could pass through the AAO nanochannel. Among the sacrificial layers etching process, silicon nitride dry-etching step is especially important. The other layers except silicon nitride could be easily removed by wet-etching process in room temperature [30]. On the other hand, wet-etching condition of the silicon nitride layer was relatively harsh and tough (phosphoric acid wt.% 80% at 160°C) [30]. During the silicon nitride wet-etching step, AAO layer could be damaged by the etchant. Therefore, dry-etching of silicon nitride is a requisite process to make AAO membrane. In addition, the thickness of the silicon nitride layer is accounted for the larger proportion than the others.

As the thickness of silicon nitride layer reduced, the AAO membrane is getting transparent (Figure 2-20). However, depending on the dry-etching conditions such as RF power and etching gas, the etching result could be seriously different. Reactive-ion etching (RIE 80 plus, Oxford Instrument) is performed to remove the  $\text{Si}_3\text{N}_4$  layer ( $\text{O}_2$ : 5 sccm,  $\text{CF}_4$ : 50 sccm, pressure: 55 mTorr, RF power: 100 W). In the same conditions, etching process time is investigated in Figure 2-21. 350 nm thickness of silicon nitride layer (Figure 2-21 (a)) is completely vanished after 12 min etching time. Considering the etching process time is 7 min and additional 5 min, the etching rate on free-standing membrane (< 35 nm/min) is lower than etching rate on the silicon wafer substrate (~80 nm/min). This different etching rate is supposed that the RF power focusing is changed with the substrate conditions.

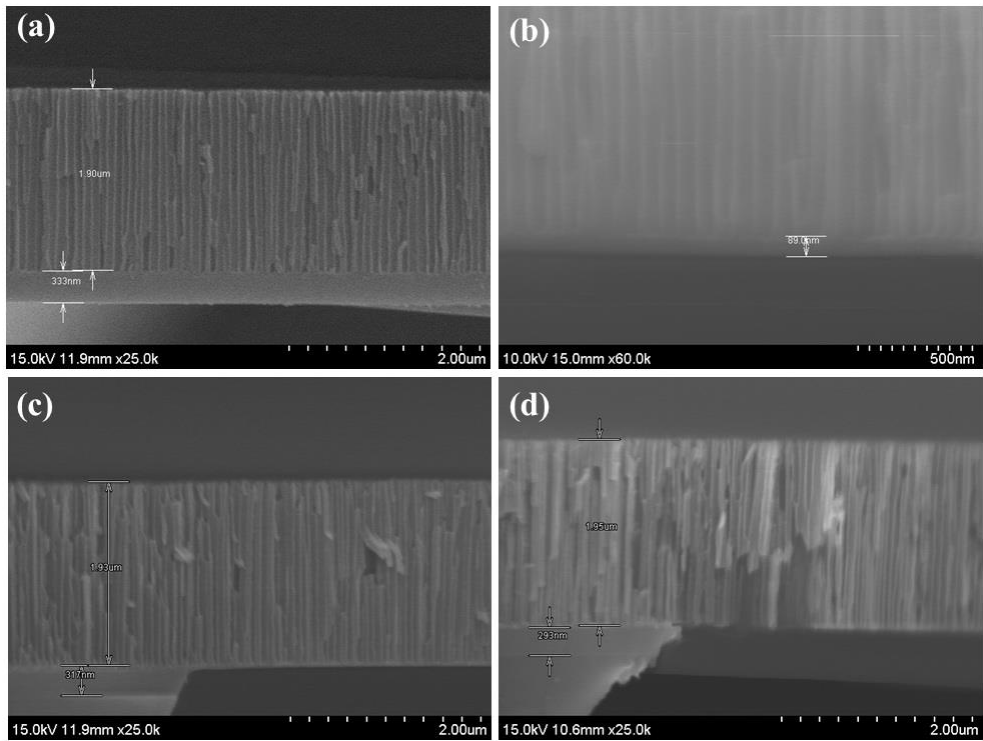


Figure 2-21. SEM images of  $\text{Si}_3\text{N}_4$  etching on free-standing AAO membrane, (a) 0 min, 350 nm, (b) 7 min, 90 nm, (c) (7 + 3) min, < 10 nm, (d) (7+5) min, 0 nm.

PDMS structures are bonded to the top and bottom sides of the AAO membrane, forming separate chambers that are directly connected through the pores in the membrane in Figure 2-22. The top and bottom chambers are composed of two reservoirs ( $R_1$  and  $R_2$ ), and venting holes ( $V_1$  and  $V_2$ ), and microfluidic channels. The PDMS structures are bonded to the AAO and silicon surfaces through  $\text{O}_2$  plasma treatment. This process, a combination of microfabrication and AAO techniques, offers flexibility to the device design, resulting in a reliable platform for high-quality experiments. The venting holes ( $V_1$  and  $V_2$ ) are useful for easy introduction of the solution and removal of air bubbles that often cause problems in electrokinetic

experiments, such as disturbing the sample and buffer flow. Since  $R_1$  is directly connected to the bottom chamber via the silicon substrate, a sample injected into  $R_1$  spontaneously flows into the bottom chamber via the silicon substrate through a capillary effect.

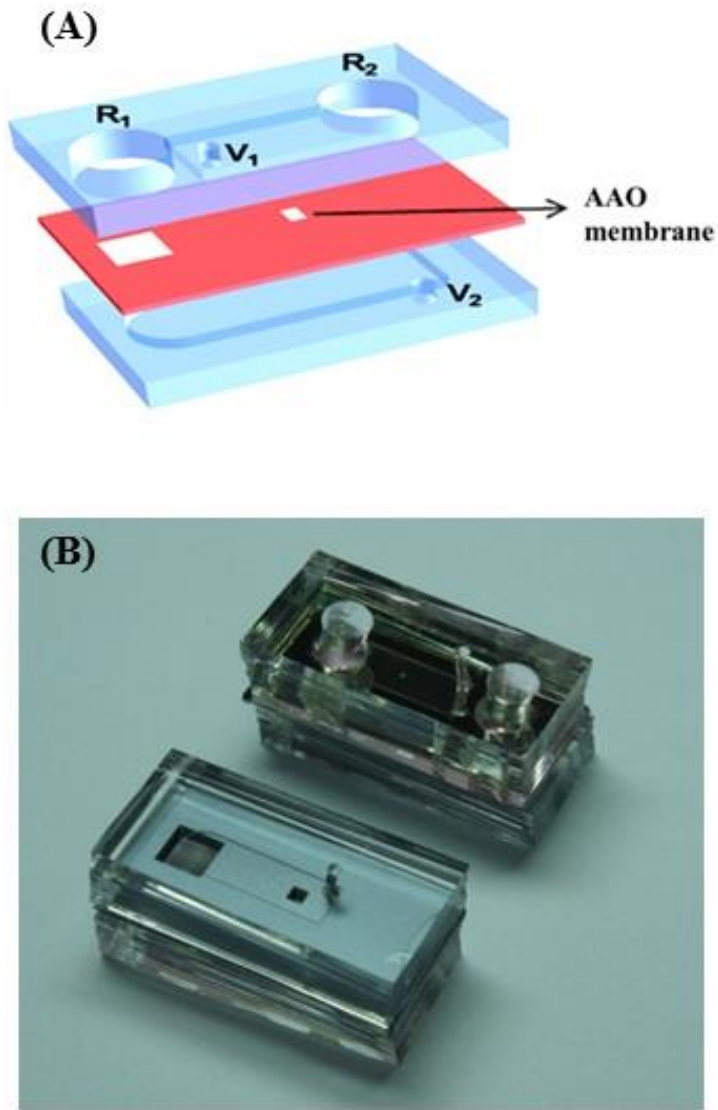


Figure 2-22. (A) Device integration schematic of the AAO membrane and double side PDMS microchannels, (B) Device images after bonding process with  $O_2$  plasma

### 2.3.4 Experimental setup

Due to capillary effects and the venting holes, injection is achieved without any external pressure source applied, such as the use of pneumatic apparatus. The device filled with the sample is placed on a fluorescence microscope stage (Nikon Eclipse\_ME600L) and the Pt electrodes are connected to a power supply (Keithley 2440) in Figure 2-22. When a voltage is applied, the FITC-tagged ssDNA in the bottom reservoir is transported to the top chamber and detected by observing the light fluorescence. To estimate the amount of transported DNA, the light intensity (arbitrary unit) is quantified by averaging the pixel intensity over the whole observation area with image analysis. The change in current during the experiment is monitored with a current source meter (Keithley 2440).

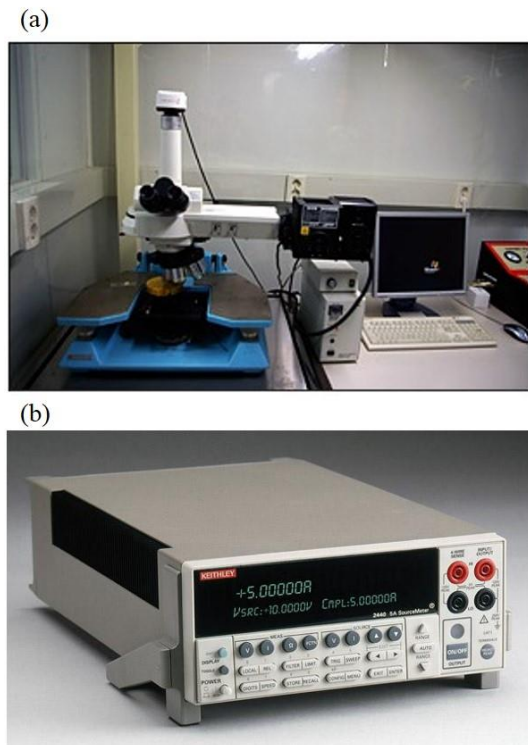


Figure 2-23. Experimental equipment. (a) Nikon Eclipse\_ME600L, (b) Keithley 2440

## 2.4 Results and discussion

### 2.4.1 DNA separation

When the microfluidic channels are filled with buffer, the negatively charged molecules are repelled from the porous membrane because the surface of the AAO is usually positively charged in solution [31]. It is called as Debye length, which increases with a decrease in buffer concentration. Debye length is one of the most important factors for determining the effective pore size; however, effective pore size is sometimes strongly influenced by electroosmotic flow (EOF) which is the motion of liquid induced by an applied potential across a porous material [5]. The zeta potential may also increase with a decrease in buffer concentration. These effects are possible contributors to a decrease in the effective pore size.

To explicitly demonstrate the relationship between effective pore size and ionic strength, we observe the FITC-tagged ssDNA (1  $\mu$ M, 15-mer poly(A)) translocation event through the nanoporous membrane in a serially controlled range of ionic strengths. ssDNA is injected into the bottom chamber, the membrane appears bright before applying the voltage because the AAO is a semi-transparent material. The quantity of DNA transported through the nanopore is estimated from the fluorescence intensity. As shown in Figure 2-24, when the electric field is applied across the membrane (positive at the top and negative at the bottom), ssDNA transport is most effective in the 50  $\times$  TAE buffer condition.

In high ionic strengths, where the Debye length and zeta potential are negligible, the effective pore size is almost identical to the physical pore size (Figure 2-25).

Therefore, negatively charged ssDNA molecules with diameters smaller than the physical pore size can easily pass through the pore. When the polarity of the electric field is reversed, transported DNAs return to the original place through the AAO nanoporous membrane. Whereas, EOF acts as dominant factor for driving the DNA translocation through the nanopore in low ionic strength condition which the positively charged electrical double layer is maximized. We confirm that the EOF runs downward through the membrane when the electric field is applied at  $0.5 \times$  TAE buffer condition.

However, in Table 2-3, the estimated effective pore size at  $0.5 \times$  TAE buffer concentration is about 7 nm. This effective pore size is larger than 15-mer DNA in this experiment. In fact, the estimated EDL thickness in nano pore is thicker than that of bulk state. This reason is why the ion depletion in nanochannel occurs when electric field is applied [32, 33]. As a result, the effective pore size is smaller than the expectation, and the passage of DNA through the nano porous membrane is changed as present in Table 2-3.

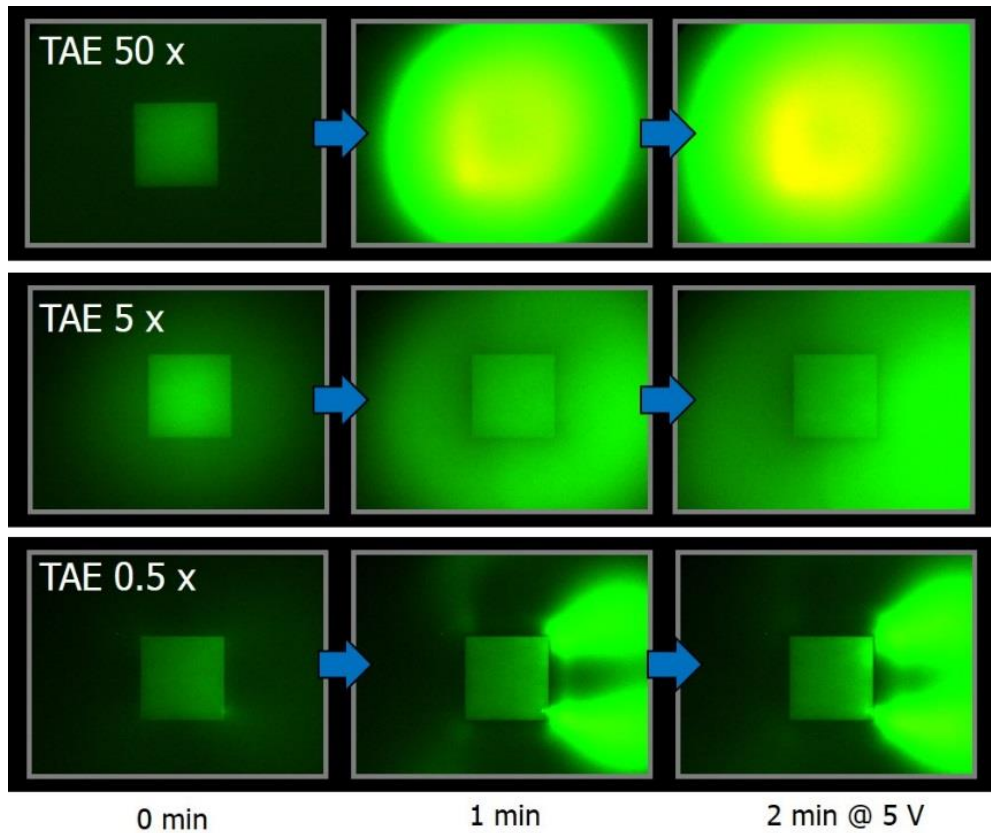


Figure 2-24. Control of effective pore size by ionic strength. 50×, 5×, and 0.5× TAE buffer condition.

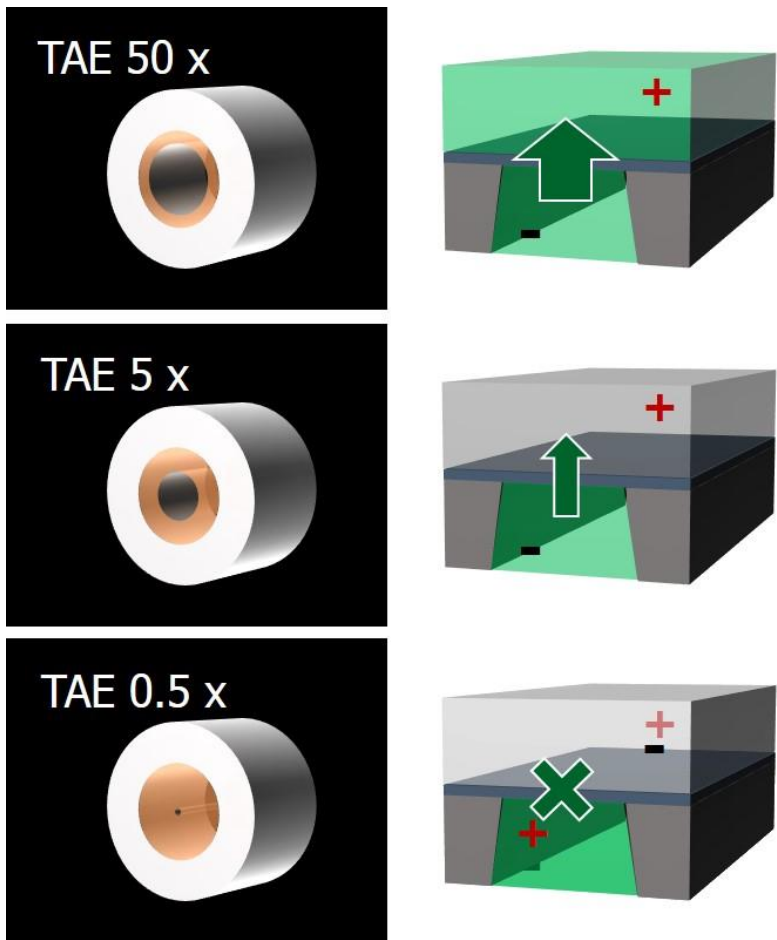


Figure 2-25. Biomolecular transport in different ionic strength  $50 \times$ ,  $5 \times$ , and  $0.5 \times$  TAE buffer condition, respectively. Green arrow indicate the direction and quantity of bimolecular transport.

Table 2-5. EDL thickness & effective pore size w.r.t. buffer concentration in bulk conditons

TAE buffer concentration	$\lambda_D$ (= EDL thickness)	Effective pore size	$D_{pore} = 13 \text{ nm}$
$50 \times$	0.3 nm	12.4 nm	
$5 \times$	0.96 nm	11.02 nm	
$1 \times$	2.14 nm	8.72 nm	
$0.5 \times$	3.026 nm	6.95 nm	

Based on these effective pore sizes, all other bimolecular translocation experiments considered in this work are demonstrated with  $50 \times$  TAE buffer. The change in current during the translocation of ssDNA through the AAO nanoporous membrane is plotted in Figure 2-26. The current decreases for the first minute while the light intensity increases because the pores are physically blocked by the ssDNA that quickly approaches the membrane at the beginning of the transport. As the DNA is transported to the opposite side of the membrane, the current and light intensity slowly increases [34]. As shown in Figure 2-27, the light intensity linearly increases with time for the initial period of the experiment. It is worthwhile to note that the slope of the increase is dependent upon the applied voltage. It is clear that DNA molecules are transported more quickly when higher voltages are applied. Such capability of controlling the transport rate may offer a useful method for fine separation. It also verified that translocation throughput efficiency linearly depends on concentration as can be seen in Figure 2-28.

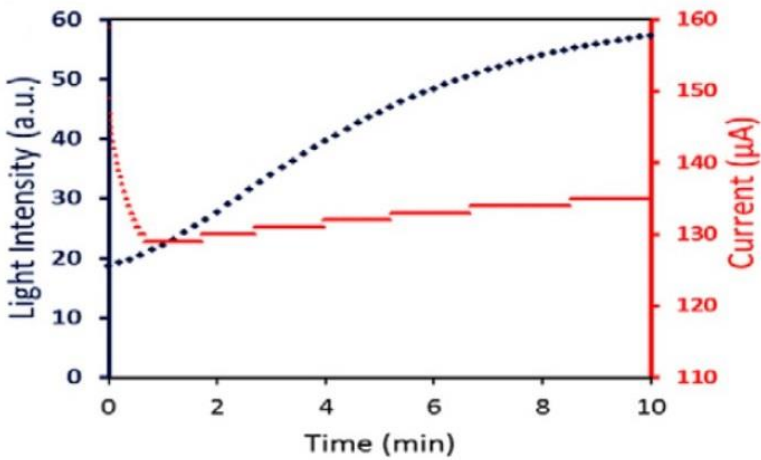


Figure 2-26. Biomolecular separation through the nanoporous membrane. Changes in current during the translocation of DNA through the AAO nanoporous membrane

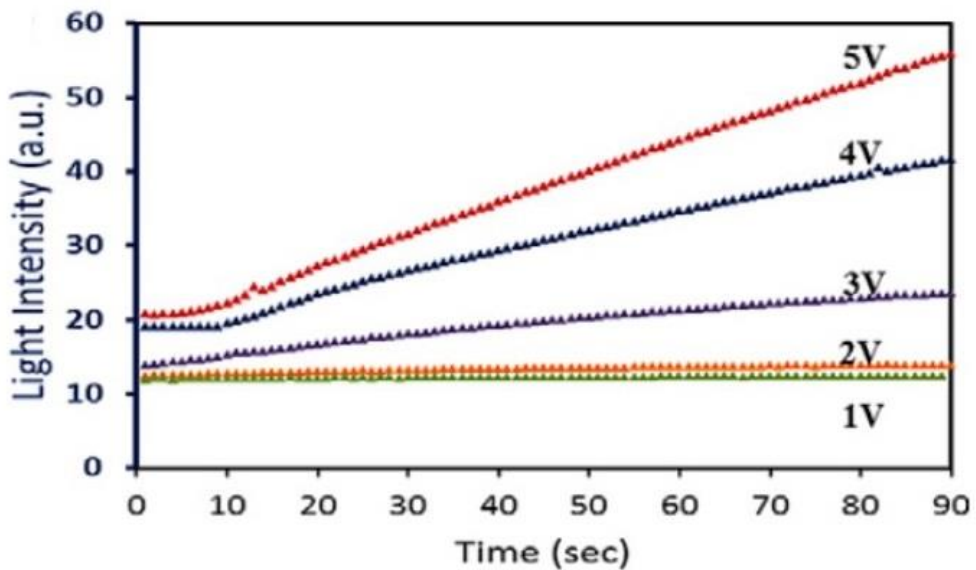


Figure 2-27. Biomolecular separation through the nanoporous membrane. ssDNA translocation vs. applied voltage,

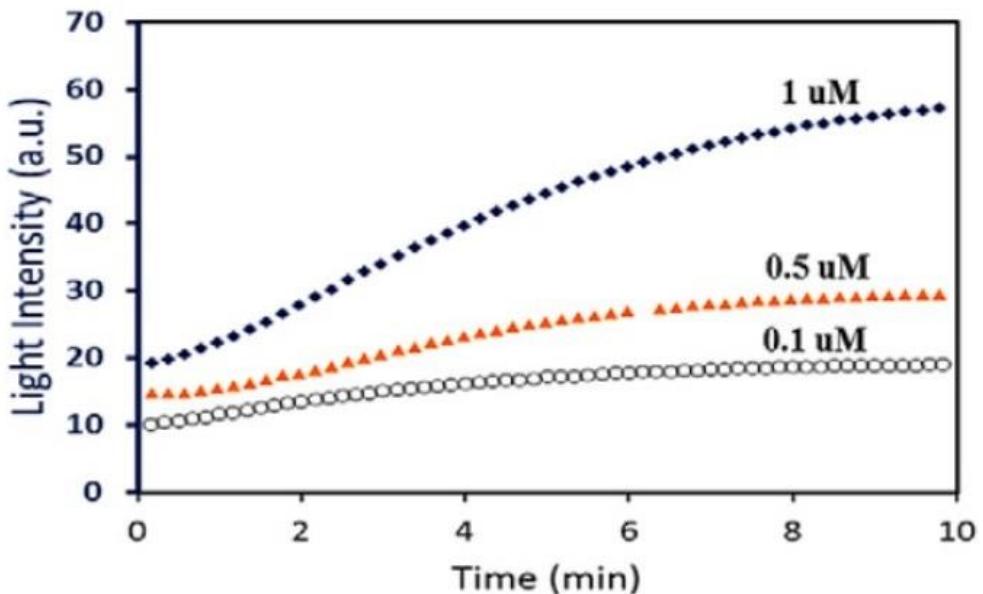


Figure 2-28. Biomolecular separation through the nanoporous membrane. ssDNA translocation vs. different ssDNA concentrations.

## 2.4.2 DNA & protein separation

To verify the size exclusive bimolecular separation, we use a complex of thrombin (coagulation protein, 36 kDa) and thrombin aptamer (4 kDa, 5'-FITC-GGT TGG TGT GGT TGG-3') [24]. Thrombin and FITC-tagged (0.33 kDa) thrombin aptamer were incubated in an aptamer binding buffer (20 mM Tris-acetate, pH = 7.4, 140 mM NaCl, 5 mM KCl, 1 mM CaCl<sub>2</sub>, and 1 mM MgCl<sub>2</sub>) for 1 hour to make an aptamer-thrombin complex (ATC). Figure 2-29 compares the separation efficiency of the free aptamer and the ATC, both at concentrations of 1 M in the 50 × TAE buffer, driven by 5 V. It is obvious from the transport results that ATC is not effectively transported through the pore while other DNA molecules easily pass through the pores. The particle diameter of a thrombin molecule, as calculated from its molecular weight, is ~ 4.9 nm [35], whereas that of a DNA strand is ~ 1 nm. Since there are two binding sites for thrombin at each aptamer [36], the ATC should be much larger than the DNA in terms of physical size. Furthermore, it has been reported that thrombin has seven positive charges at pH 7.4 [35], resulting in the loss of traction forces in the electric field. These sharp contrasts in size and electrical charge lead to an approximate 10-fold difference in transport efficiency in our experiments.

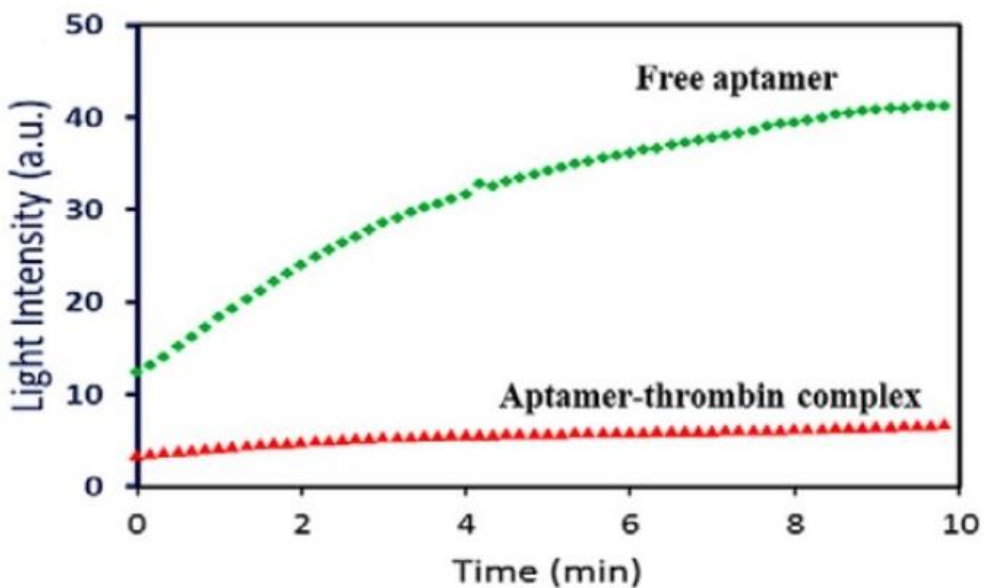


Figure 2-29. Biomolecular separation through the nanoporous membrane. Performance of size specific biomolecular separation of an aptamer and aptamer-thrombin complex at 5 V

## 2.5 Conclusions

DNA as an aptamer is separated from a complex with protein by the nanoporous anodized aluminium oxide (AAO) membrane that has well controlled pores under 100 nm in diameter. For an effective separation, virtual pore size which is determined by electrical double layer (EDL) is controlled with different buffer condition based on ionic concentration. Electrophoretic (EP) force is applied to the negatively charged DNA through nano pores of AAO for translocation. Size exclusive binary separation process is achieved due to the size difference between DNA and DNA/protein complex. To verify the transport of DNA, fluorescence intensity change is measured, and the detail of the interaction process is analyzed.

Conventional AAO membranes are already used for various applications such as bio/chemical sensors, pre-treatment filters, and nanoscale templates. These AAO membranes are made from Al-foil substrate of thickness 50 to 100  $\mu\text{m}$ , and then usually assembled in to the other device. On the other hand, AAO membrane in this work is directly fabricated from deposited Al ( $< 2 \mu\text{m}$  thickness) on silicon substrate, followed by a MEMS fabrication process to complete an integrated device. This direct AAO fabrication process can reduce the length of AAO nanochannel and improve the compatibility with microfluidic devices.

## References

1. MATHIES, A.T.W.A.R.A., *Ultra-high-speed DNA fragment separations using microfabricated capillary array electrophoresis chips*. Biophysics, 1994. **91**: p. 11352.
2. Han, J. and H.G. Craighead, *Separation of long DNA molecules in a microfabricated entropic trap array*. Science, 2000. **288**(5468): p. 1026-9.
3. Min, S.K., et al., *Theoretical Design of Nanomaterials and Nanodevices: Nanolensing, Supermagnetoresistance, and Ultrafast DNA Sequencing*. Journal of Physical Chemistry C, 2011. **115**(33): p. 16247-16257.
4. Min, S.K., et al., *Fast DNA sequencing with a graphene-based nanochannel device*. Nature Nanotechnology, 2011. **6**(3): p. 162-165.
5. Lagerqvist, J., M. Zwolak, and M. Di Ventra, *Fast DNA sequencing via transverse electronic transport*. Nano Lett, 2006. **6**(4): p. 779-82.
6. TAKAHASHI, H. and M. NAGAYAMA, *The determination of the porosity of anodic oxide films on aluminium by the pore-filling method*. Corrosion Science, 1978. **18**: p. 911-925.
7. Fu, J., P. Mao, and J. Han, *Artificial molecular sieves and filters: a new paradigm for biomolecule separation*. Trends Biotechnol, 2008. **26**(6): p. 311-20.
8. Kim, J. and B.K. Gale, *Quantitative and qualitative analysis of a microfluidic DNA extraction system using a nanoporous AlO(x) membrane*. Lab Chip, 2008. **8**(9): p. 1516-23.
9. Hideki Masuda, K.F., *Ordered Metal Nanohole Arrays Made by a Two-Step Replication of Honeycomb Structures of Anodic Alumina*. Science, 1995. **268**(5216 ): p. 1466-1468.
10. Poinern, G.E.J., N. Ali, and D. Fawcett, *Progress in Nano-Engineered Anodic Aluminum Oxide Membrane Development*. Materials, 2011. **4**(3): p.

487-526.

11. Patermarakis, G., *Development of a theory for the determination of the composition of the anodizing solution inside the pores during the growth of porous anodic Al<sub>2</sub>O<sub>3</sub> films on aluminium by a transport phenomenon analysis*. Journal of Electroanalytical Chemistry, 1998. **447**(1): p. 25-41.
12. Palibroda, E., *Aluminum porous oxide growth—II. On the rate determining step*. Electrochimica acta, 1995. **40**(8): p. 1051-1055.
13. Shawaqfeh, A.T. and R.E. Baltus, *Fabrication and characterization of single layer and multi-layer anodic alumina membranes*. Journal of Membrane Science, 1999. **157**(2): p. 147-158.
14. *Anopore Inorganic Membranes (Anodisc)*. [cited 2013 03 April]; Available from: <http://www.whatman.com/PRODAnoporeInorganicMembranes.aspx>.
15. *Electrophoresis*. Available from: <http://commons.wikimedia.org/wiki/File:Electrophoresis.svg>.
16. *gel electrophoresis of DNA*. Available from: <http://www.ncbe.reading.ac.uk/ncbe/materials/dna/baseunit.html>.
17. Bakewell, D.J., N. Vergara-Irigaray, and D. Holmes, *Dielectrophoresis of Biomolecules*. 2013.
18. Dolnik, V., S. Liu, and S. Jovanovich, *Capillary electrophoresis on microchip*. Electrophoresis, 2000. **21**(1): p. 41-54.
19. *DNA structures*. Available from: <http://en.wikipedia.org/wiki/DNA>.
20. Neidle, S., *Principles of nucleic acid structure*. 2010: Academic Press.
21. Watson, J.D. and F.H. Crick, *Molecular structure of nucleic acids; a structure for deoxyribose nucleic acid*. Nature, 1953. **171**(4356): p. 737-8.
22. Gregory, S.G., et al., *The DNA sequence and biological annotation of human chromosome 1*. Nature, 2006. **441**(7091): p. 315-21.

23. Nelson, P., *Biological physics*. 2004: WH Freeman New York.
24. Macaya, R.F., et al., *Thrombin-binding DNA aptamer forms a unimolecular quadruplex structure in solution*. Proc Natl Acad Sci U S A, 1993. **90**(8): p. 3745-9.
25. Russel, W.B., D.A. Saville, and W.R. Schowalter, *Colloidal dispersions*. 1992: Cambridge university press.
26. Aptamer interaction with Thrombin. Available from: <http://www.nanotemper-technologies.com/applications/list-all-applications/article/aptamer-interaction-with-thrombin/>.
27. Kim, Y., et al., *Electrokinetic separation of biomolecules through multiple nano-pores on membrane*. Chemical Physics Letters, 2013. **561**: p. 63-67.
28. Hoar, T.P. and N.F. Mott, *A Mechanism for the Formation of Porous Anodic Oxide Films on Aluminium*. Journal of Physics and Chemistry of Solids, 1959. **9**(2): p. 97-99.
29. Park, S.-H., et al., *The Formation of Porous Anodic Aluminum Oxide Confined in  $\mu$ m-Size Contact and Trench Patterns*. Electrochemical and Solid-State Letters, 2006. **9**(12): p. D31.
30. Williams, K.R., K. Gupta, and M. Wasilik, *Etch rates for micromachining processing - Part II*. Journal of Microelectromechanical Systems, 2003. **12**(6): p. 761-778.
31. Miao, J.Y., et al., *Micropumps based on the enhanced electroosmotic effect of aluminum oxide membranes*. Advanced Materials, 2007. **19**(23): p. 4234-+.
32. Pu, Q.S., et al., *Ion-enrichment and ion-depletion effect of nanochannel structures*. Nano Letters, 2004. **4**(6): p. 1099-1103.
33. Höltzel, A. and U. Tallarek, *Ionic conductance of nanopores in microscale analysis systems: Where microfluidics meets nanofluidics*. Journal of

- separation science, 2007. **30**(10): p. 1398-1419.
34. Zwolak, M. and M. Di Ventra, *Colloquium: Physical approaches to DNA sequencing and detection*. Reviews of Modern Physics, 2008. **80**(1): p. 141-165.
35. Heuck CC, S.U., Horn D, Fronda D, Ritz E., *The role of surface charge on the accelerating action of heparin on the antithrombin III-inhibited activity of alpha-thrombin*. J Biol Chem, 1985. **260**(8): p. 4598-603.
36. Russo Krauss, I., et al., *Thrombin-aptamer recognition: a revealed ambiguity*. Nucleic Acids Res, 2011. **39**(17): p. 7858-67.

### 3 Part II : Separation of micro scale particles

Blood plasma separation from whole blood is a crucial process for many clinical tests and assays. For example, point-of-care (POC) diagnosis requires the blood plasma separation for the monitoring of cholesterol, glucose, and hepatic function in blood [1, 2]. In order to achieve detection of various target proteins with high sensitivity and reliability, such separation process is necessary [3]. Various microfluidic devices for blood separation and plasma extraction have been developed [4-9]. Recent approaches include microfluidics-based blood component separation. Microfluidics has many advantages such as only needing small sample volume for experiment. However microchip of microfluidics had given rise to limitations in various sample preparation, separation methods and integrated blood analysis modules [10]. Recently, various types of blood cell separation method have developed such as microchannel with trench (SIMBAS) [11], paper-based analytical device ( $\mu$ -PAD) [12], centrifugal platform [13], and surface acoustic wave (SAW) [3] and so on. However, these methods are generally horizontal systems with limited flux capacity per unit time. Here we suggest a vertical separation device for high throughput and high quality separation efficiency through integration of dielectrophoretic (DEP) function on a micro-porous membrane.

In this study, we designed a blood plasma extraction device that integrates DEP function on a micro-patterned membrane. It has been demonstrated in a previous research that a pore array with size variation could filter the blood particles with

different efficiency of separation [12]. We targeted enhancing the separation efficiency and speed by establishing a “virtual barrier” with DEP function integrated on a membrane with a regular pore size and distribution. Metal electrodes were patterned on the membrane for preventing clogging by blood cells through the application of negative DEP, while helping blood plasma to pass through the membrane pores selectively. Essentially the DEP force is designed to block the passage of red blood cells (RBCs), which account for more than 90% of the whole blood cells including white blood cells (WBCs) and platelets. The diameter of micro pore array were varied between 3~10  $\mu\text{m}$ , but targeted to filter RBCs whose size is approximately 6~8  $\mu\text{m}$ .

The membrane with the pore array is a thin (500 nm)  $\text{Si}_3\text{N}_4$  film directly integrated on a silicon substrate. The filter device was integrated into a complete microfluidic system. DEP function was verified by diluted blood. The blood cells were repelled from the gaps between electrodes when a negative DEP force ( $V_{pp}=6.5$  V, 500 kHz) was applied for 1 min. Before applying voltage, blood cells had covered the whole surface. On the other hand, after voltage was applied, blood cells were aligned along the center of electrode between micro pores on the gaps. The characteristic of flow passage was also verified by placing various liquids on top of the membrane with/without applying the DEP force. Main driving force for the flow through the pore array was Laplace pressure from the meniscus of the droplet. D.I water could rapidly pass through the pore filter. However, the diluted blood sample passed the membrane at a much slower speed than that of D.I water because of its high viscosity. The height of the plasma drop slowly decreased as the fluid was transferred.

### 3.1 Concept and applications

The goal of this study is the plasma extraction from whole blood. To fractionate the plasma from other blood cells including RBCs, WBCs, and platelets, we combined the micron size of pore-array membrane and dielectrophoretic function. The pore-array were designed for the prevention of RBCs to pass through the pore, and the DEP function were targeted to RBCs because RBCs account for the half of the whole blood and more than 90% of the whole blood cells.

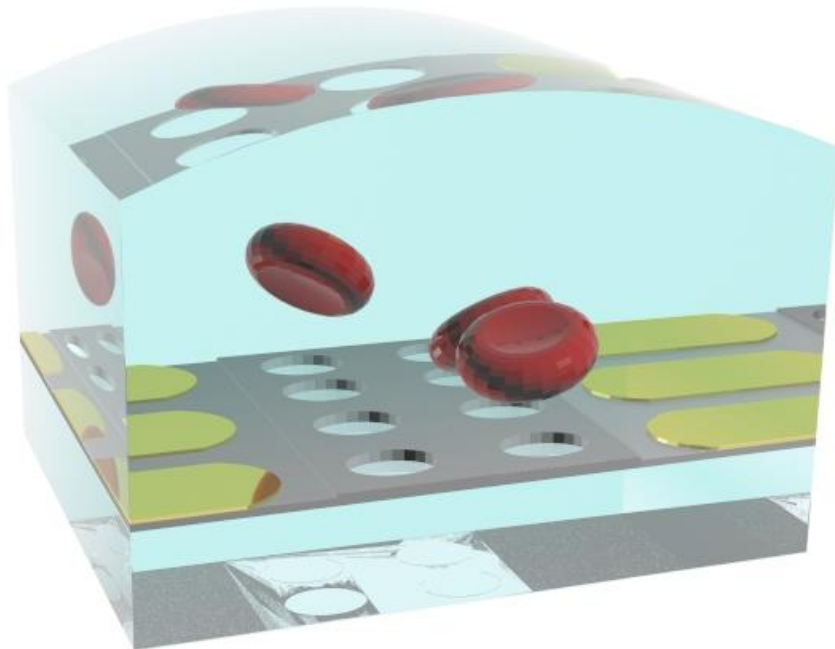


Figure 3-1. Concept of plasma extraction. On the micron size of pore-array, DEP electrodes are patterned to prevent the blood cell clogging on the pore. Red parts are blood cells (RBCs), yellow parts are DEP electrodes, and grey parts are pore-array membranes.

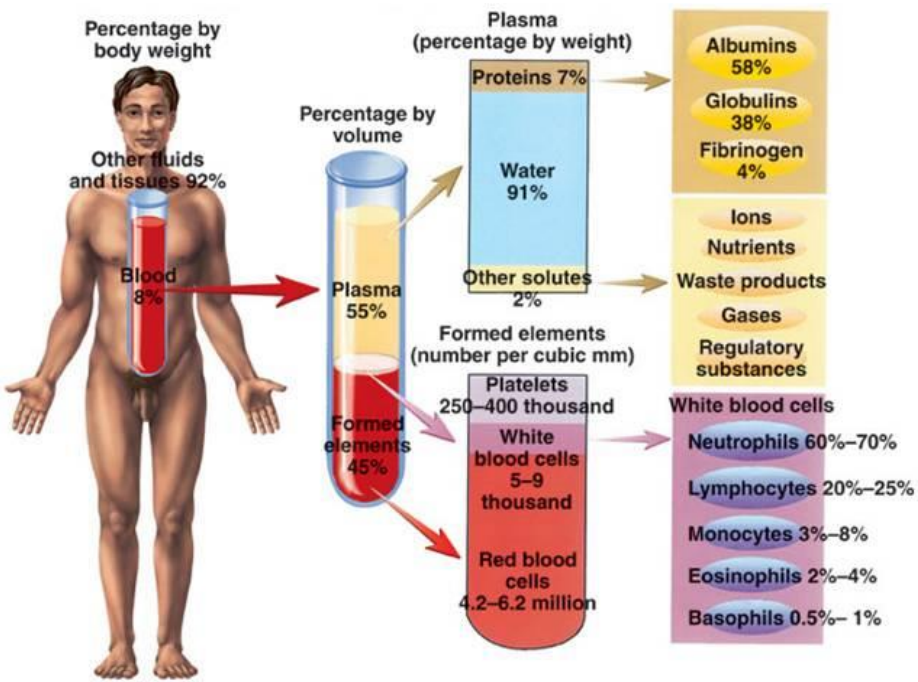


Figure 3-2. Composition of human blood [14]. Plasma is a pale yellow-colored, clear liquid that is 91% water, 7% proteins, and 2% other substances including ions, nutrients, gases, and waste products.

In the clinical tests, for example, simple diagnostic test of blood plasma for biological components like proteins in Figure 3-2 taking up 7% of the plasma weight, can be used to estimate the normal state of health in various internal organs. The qualification of individual plasma proteins is also routine and important for diagnosis and monitoring of many diseases such as paraproteinaemias, hemoglobinopathies, and genetic abnormalities [2, 15, 16]. However, it is critical to remove large volume of interfering blood cells from whole blood so that the purified plasma can be assessed and diagnosed accurately.

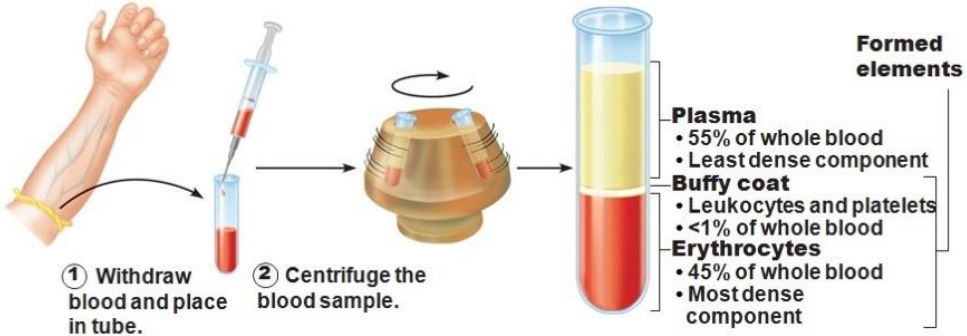


Figure 3-3. The conventional clinical way for plasma extraction [17]. This centrifugal method requires long processing time, large amount of blood sample, bulky space and relatively high external power.

The conventional method of plasma extraction from blood is centrifugation with conventional bench-top centrifuges, which are known to be expensive, time consuming and labor intensive. The practice of centrifugation has also been performed on the microscale level using compact disk-like platforms with manifolds and a spinning motor plate to achieve centrifugal pumping, fostered by the need to develop an integrated total analysis system [18-20]. In [20], they succeed to extract  $\sim 58 \mu\text{l}$  plasma from  $100 \mu\text{l}$  whole blood after 8 min of centrifugation with very high purity, cell concentration  $\sim 5 \times 10^4 \text{ ml}^{-1}$ . However, during centrifugation the sedimented blood cell can easily lyse (RBCs hemolysis), thereby releasing intracellular components which contaminate the plasma sample [20]. To overcome this limitation, several microfluidic techniques for plasma isolation from blood have been recently reported.

### 3.1.1 Micro scale pore array membrane

In the micro pore-array design, the pore-array is the microfilter which mainly targets to exclude RBCs from whole blood because the portion of RBCs is the highest in blood except plasma (see Figure 3-2). In human blood as shown in Figure 3-4, RBCs are 6-9  $\mu\text{m}$  in diameter, and 1.8-2.8  $\mu\text{m}$  in thickness, while WBCs are more than 7  $\mu\text{m}$  in diameter. In spite of their large size, WBCs can deform and squeeze through gaps as narrow as 7  $\mu\text{m}$  [21]. On the other hand, RBCs can readily align themselves and pass through spacing as narrow as 3  $\mu\text{m}$  [22]. Hence, the pore-array isolates RBCs based on size, or a combination of size and cell deformability. Using microfabrication, well-defined geometry and precise pore size as fine as sub-micrometres can be achieved. Silicon nitride membrane is a strong and rigid structure which does not easily break or deform under typical microfluidics driving pressure. A precise size distribution control or pore-array can be attained by lithography in microfabrication.

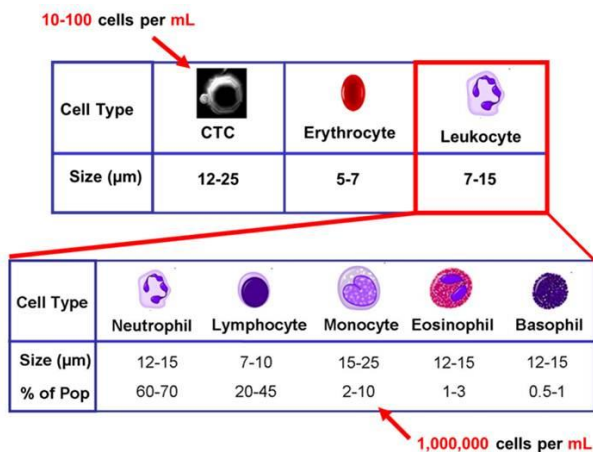


Figure 3-4. Blood cell size distribution [17]. Thrombocyte (platelet) is 2-3  $\mu\text{m}$  size.

In the previous microfilter, plasma was extracted without blood cells [23-25]. These designs needed a fine sieve with a cut-off size under 1  $\mu\text{m}$ . Various types of silicon-based microfilter designs were thus investigated. For examples, silicon-based perforated membranes with various pore shapes have been represented for trapping particles in the range of 1 to 10  $\mu\text{m}$  [26]. Figure 3-4 shows photographs of the fabricated filters with (a) circular (b) rectangular and (c, d) hexagonal holes.

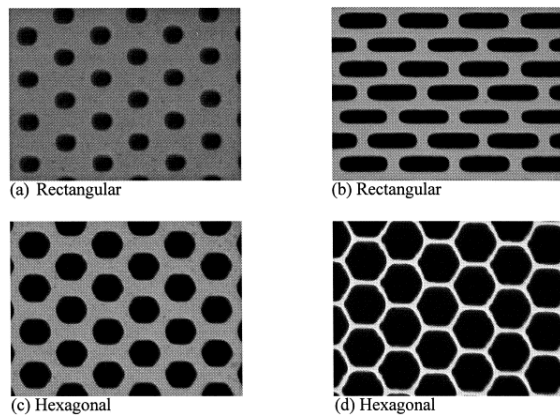


Figure 3-5 Photographs of the fabricated filters with different hole geometries [26]

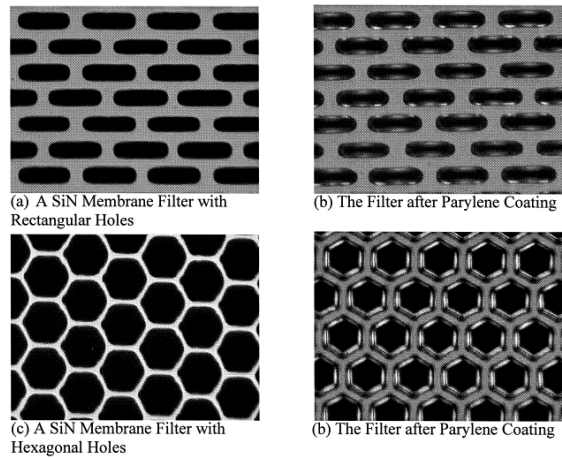


Figure 3-6. Photographs of the filters before and after Parylene deposition [26].

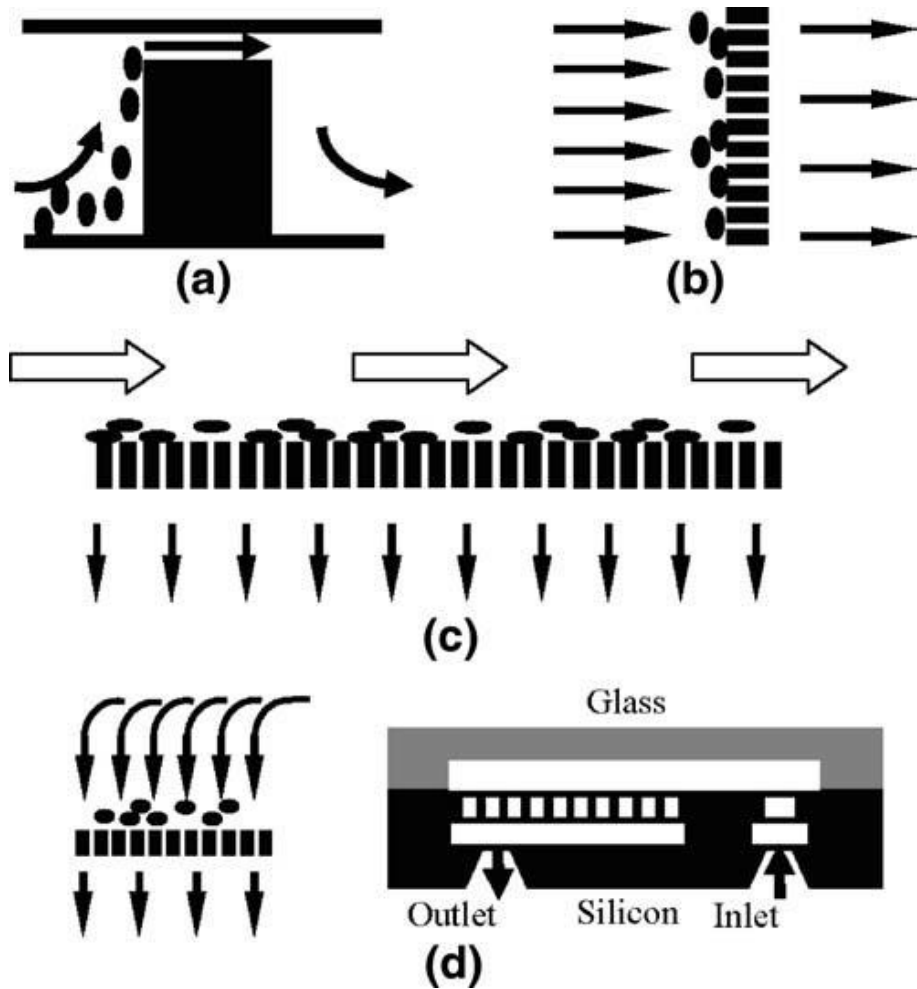


Figure 3-7. Schematics of the microfilter designs (a) weir filter (*side view*), (b) pillar filter (*top view*), (c) crossflow filter (*top view*), (d) membrane filter (*side view*) [22]

Furthermore, the microfilter designs already investigated are described in Figure 3-7 [22]. The designs can be categorized into four types: 1) weir, 2) pillar, 3) crossflow, and 4) membrane. The weir filter involves an individual barrier obstructing the flow path to trap most WBCs. RBCs can only pass through a narrow slit located on top of the barrier. The pillar filter replaces this individual barrier with a row of small pillars

spaced apart by a critical cut-off dimension. RBCs can only pass through narrow slits between the pillars. The crossflow filter is derived from the pillar type except that the pillars are located tangential to the main flow path. Crossflow filter is also known as the tangential-flow filter. The crossflow type diverts most of the flow and hence becomes less prone to clogging by sweeping the trapped WBCs towards the filter end.

Table 3-1. Total pore area and measured blood handling capacity of the microfilters [22]

Filter type	Total pore area	Blood passing capacity
Weir	0.0105 mm <sup>2</sup>	<50 µl
Pillar	0.474 mm <sup>2</sup>	300 µl
Crossflow	12.67 mm <sup>2</sup>	>300 µl
Membrane	59.6 mm <sup>2</sup>	200 µl

Table 3-2. Efficiency of microfilters for passing RBCs and trapping WBCs at a given flow of blood [22].

Filter	Flow rate	Pass RBCs	Trap WBCs
Weir	10 µl/min	28–42%	~70%
Weir	50 µl/min	10–12%	~70%
Membrane	10 µl/min	0.2%	72–85%
Membrane	10 µl/min	4%	72–85%
Pillar	20 µl/min	20–55%	70–95%
Crossflow	20 µl/min	60–95%	70–95%

The measured blood handling capacity and total pore area for each filter are listed in Table 3-1. These results show that all the filter types, except the weir filter, can

handle hundreds of microliters of blood. The total pore area across the membrane filter is larger than  $50 \mu\text{m}^2$  and at least two orders of magnitude larger than that of the pillar filter. Yet, this proportionality does not get reflected in the total blood handling capacity. One explanation could be that the total pore area of the membrane filter cannot be efficiently used due to presence of the stagnant flow regions.

Efficiency of the microfilters in terms of trapping WBCs and passing RBCs are summarized in Table 3-2. The membrane filter has an extremely low efficiency in passing RBCs—typically around 4% but may get as low as 0.2%. In order to investigate how RBCs passing efficiency is influenced by WBCs clogging the membrane, the filter was also tested directly with, instead of whole blood, isolated RBCs. However, as mentioned before, the goal of this study is the extraction of plasma without any blood cells (RBCs, WBCs and platelets). In Table 3-2, membrane microfilter has limitations on separating blood cells between RBCs and WBCs because both blood cells could not pass through the membrane microfilter. On the other side, this means the membrane microfilter can be a good platform for highly purified plasma extraction.

In conclusion, among the various microfilter types, the membrane type is the most suitable in collecting plasma from whole blood. However, extremely low efficiency in passing RBCs is a critical problem which can block the membrane pore. In addition, RBCs that enter into the filter are permanently trapped there, suggesting the presence of stagnant regions which agrees with the simulations [22].

### 3.1.2 Dielectrophoresis (DEP)

We accepted dielectrophoresis (DEP) for active energy source to prevent the pore array blockage by blood cells. As mentioned in the previous section, during the filtration process on pore array membrane, blood cells could block or be trapped in the pores. If there is no active energy to prevent the situation, pore array membrane filter should have very low efficiency in passing plasma. Therefore we need to search, design and integrate on the pore array membrane.

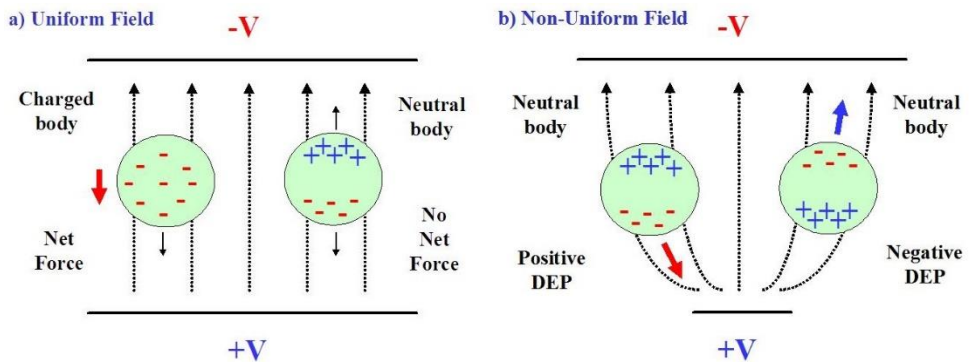


Figure 3-8. Schematic illustrating dielectrophoresis (DEP) resulted from electric force [27].

a) uniform electric field, b) non-uniform field

In a uniform electric field, dielectric particles do not move due to the zero net force, while charged particles are attracted to the opposite electrode as illustrated in Figure 3-8 a. DEP force appears when the interaction of the electric field gradient with the induced dipole of dielectric particles within the field results in a net force on the particles as shown in Figure 3-8 b [28]. Note that DEP force can be observed either with AC or DC excitation, because it does not depend on the polarity of the electric

field. Also, DEP is most easily observed in particles with diameters ranging from around 1-1000  $\mu\text{m}^2$ , because gravity (above 1000  $\mu\text{m}^2$ ) and Brownian force (below 1  $\mu\text{m}^2$ ) overwhelm the DEP force out of this range [27].

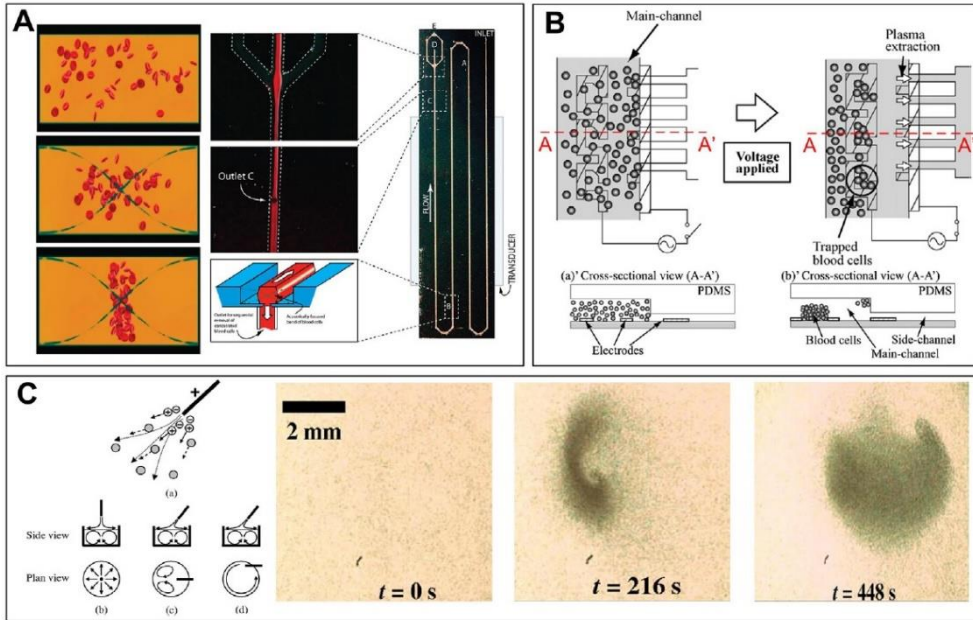


Figure 3-9. Plasma separation using various active energy source [2]. A) acoustophoresis [29], B) dielectrophoresis (DEP) combined with capillary force [1], C) bulk electrohydrodynamics thrust or ionic winds generated by sharp corona electrode tip [30]

Plasma separation methods from blood using active energy source such as acoustophoresis, electrohydrodynamics and dielectrophoresis (DEP) have also been explored [1, 29-34]. Among the various energy sources, DEP offers another effective method of separating blood plasma relying on an inhomogeneous electric field between two electrodes to induce electrostatic forces to trap cells [1]. When polarizable cells (RBCs) are placed in the non-uniform electric field, a net electric

force is imparted on the cells due to an induced or permanent dipole. This requires an electric power supply unit and control circuits outside a microfluidic device, but these peripheral devices can be miniaturized easily using LSI technology. Also, electric connections between a microfluidic device and circuit units will make setting and replacement of microfluidic devices much easier than tube connections. Moreover, no tube connections will reduce dead volume dramatically, and also lead to a highly significant decrease in blood sample. Separation of blood plasma from diluted blood (1:9) using a DEP microfluidic device was demonstrated. Blood is injected into the main channel by capillary force and in the presence of an electric field the RBCs are trapped at the electrodes while cell free plasma is collected downstream. Applying an AC signal of 10 V and 10 MHz, the device is capable of removing about 97% of blood cells to generate 300 nl plasma from 5  $\mu$ l of blood. The selectivity of the method between plasma and blood cell demonstrates good value. However, the recovery rate from the total injected volume is 6% volume ratio which is too low to use.

In conclusion, we integrate the pore array membrane and DEP, where one has an advantage in high flow rate through the membrane and the other has enough force to manipulate the blood cells. We design a different method based on similarity changing capillary to pore array membrane. This membrane should improve the performance compared with the previous capillary.

### 3.2 Theoretical background

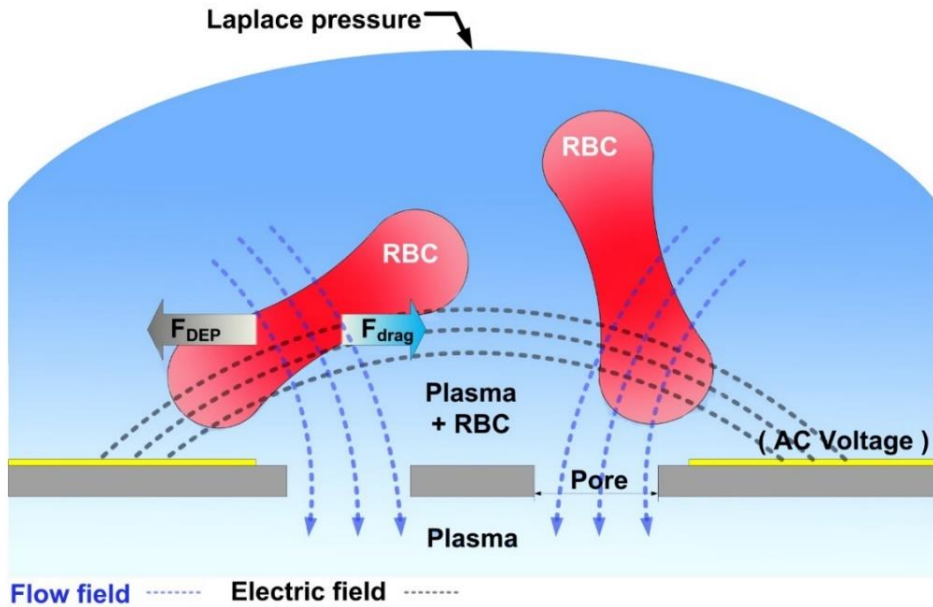


Figure 3-10. Schematic diagram of force balance between DEP force and hydrodynamic viscous force.

In Figure 3-10, the schematic demonstrates the simplified applying forces on blood cells, especially RBCs. When blood droplet forms *Laplace* pressure, the flow fields are concentrated toward the pores on the membrane. Blood, including blood cells and plasma, try to pass through pores. However, the size of the pores are not to permit the penetration of blood cells. Then, blood cells remain on the pores and block the filtration of plasma through the pores. During DEP force application by AC voltage, the electric fields are formed between the positive and negative electrodes. Therefore, the blocking blood cells are forced to move away from the pores. If DEP force is too

weak to move blood cells, the recovery rate, plasma filtration rate, is very low.

Therefore, we are going to compare the forces between DEP and hydrodynamic flow.

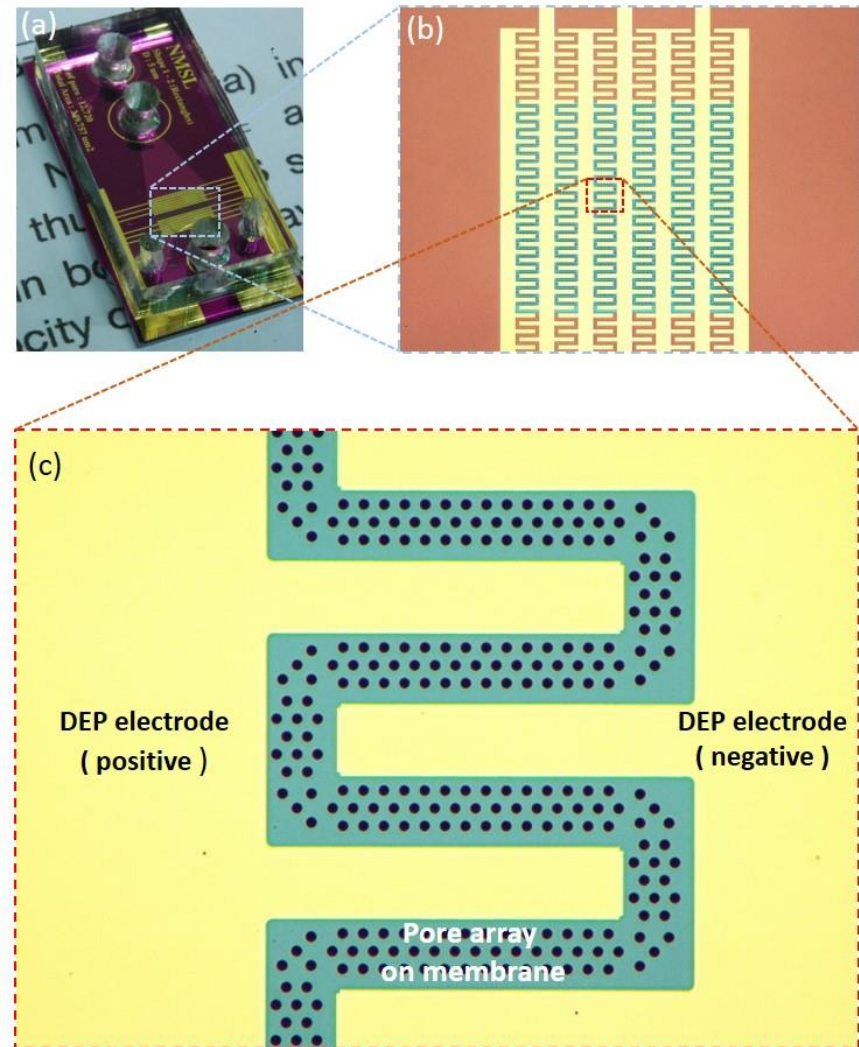


Figure 3-11. Blood cell filter images for theoretical modeling. (a) MEMS filter with PDMS microchannel, (b), (c) DEP electrode (yellow) on pore array membrane (green)

In this chapter, we are going to analyze the theoretical model which is simplified real sample model in Figure 3-11. Between the non-uniform positive and negative DEP electrodes (yellow area in Figure 3-11 (c)), the gradient of electric field makes DEP force. At the same time, blood cells try to pass through the pores on the membrane (green area in Figure 3-11 (c)), but the pores which are smaller than the blood cell prevent the passage of blood cells. We are going to investigate the exact model in Figure 3-11. The pore size varies from  $2 \mu\text{m}$  to  $10 \mu\text{m}$ , the gap between DEP electrodes is  $20 \mu\text{m}$ . Also the effects of DEP electrode shape, AC voltage amplitude and frequency are surveyed by calculation and finite element analysis (FEA) with COMSOL 3.5.

### 3.2.1 Forces on microparticles

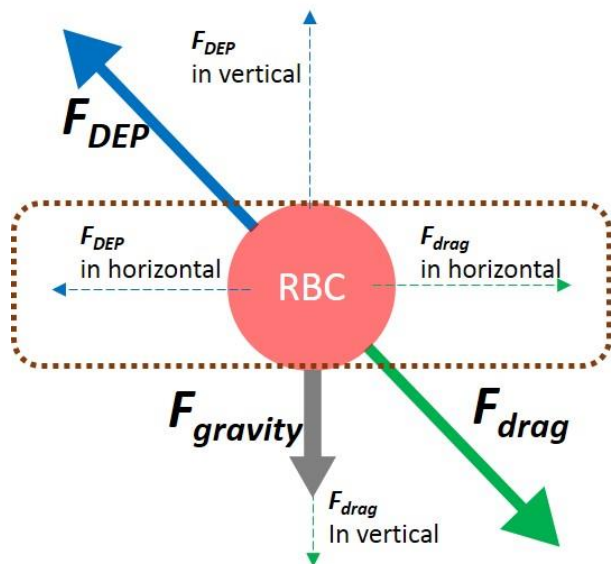


Figure 3-12. Schematic of forces on blood cell, RBC. (Blue arrow: DEP force, green arrow: hydrodynamic drag force, grey arrow: gravity force).

We will compare the DEP and hydrodynamic drag forces which are applied on the particle, blood cell. Based on equations and FEA data, the electric field and flow streamline could derive the DEP force and the drag force. In fact, there are the horizontal and vertical velocity components as shown in Figure 3-12. The applied forces on the RBC, particle, are DEP force ( $= F_{DEP}$ ), hydrodynamic drag force ( $= F_{drag}$ ), and gravity force ( $= F_{gravity}$ ). In vertical direction,  $F_{drag}$  is much stronger than  $F_{DEP}$  near the pore which acts like a flow sink. In contrast, in horizontal direction,  $F_{DEP}$  force can be comparable to  $F_{drag}$ . In fact, the object applying DEP force is not to buoy blood cell vertically, but to push out blood cell from pores in any+ direction. Thus, the vertical forces of  $F_{drag}$ ,  $F_{drag}$ , and  $F_{gravity}$  could be negligible. Instead of considering both direction forces, we focused on the effective direction of forces. At this point, we balance  $F_{DEP}$  and  $F_{drag}$  based on equations and FEA data.

If the particle, RBC, starts to move inside a fluid, this velocity is changed to relative velocity of the particle to fluid flow,  $u_{particle}$ .

$$u_{particle} = u_{fluid} + u_{DEP} \quad (3.1)$$

Here,  $u_{fluid}$  is fluid velocity and  $u_{DEP}$  is velocity induced to a particle by DEP force and these two forces are activated toward the opposite direction. We can derive the equation of particle velocity by comparing DEP force and viscous drag.

$$F_{DEP} + F_{Drag} = 0 \quad (3.2)$$

### 3.2.2 DEP force expression on blood cell

DEP is a phenomenon, which results in movement of polarizable particles in non-uniform AC electric fields. DEP is easily observed in the particles in the range of diameter 1 – 1000  $\mu\text{m}$ , because of the effect of gravity (above 1000  $\mu\text{m}$ ) and Brownian force (below 1  $\mu\text{m}$ ). Also DEP has been applied on many biological particles such as bacteria, DNA and RNA [27, 35]. In general, the geometry of particle would be important to calculate DEP effect on the particle. Blood cells, especially RBCs, are difficult in modelling because of its complex multi-shelled shape. In the previous study, blood cell is represented using complex shelled spheroid model [35]. In the real model, each layer has an intrinsic complex permittivity, which is a function of the permittivity ( $\epsilon$ ), conductivity ( $\sigma$ ), and the ratio of the imaginary number ( $j$ ) over the frequency of the applied field ( $\omega$ ). However, in research, we simplified the blood cell model for efficient calculations.

Table 3-3. Parameterization of multi-shelled spheroid model [90]

RBCs	Symmetric axis radius	$a$	1 $\mu\text{m}$
	Asymmetric axis radius	$r$	3.5 $\mu\text{m}$
Cytoplasm	Relative permittivity	$\epsilon_{cyto}$	50
	Conductivity	$\sigma_{cyto}$	0.53 S/m
Membrane	Relative permittivity	$\epsilon_{mem}$	9.04
	Conductivity	$\sigma_{mem}$	$10^{-6}$ S/m
	Thickness	$d_{mem}$	8 nm
Buffer medium	Relative permittivity	$\epsilon_m$	80
	Conductivity	$\sigma_m$	0.13 S/m

DEP force ( $F_{DEP}$ ) acting on a spherical particle immersed in a medium can be described by

$$F_{DEP} = 2 \pi \varepsilon_0 \varepsilon_m r^3 \operatorname{Re}[f_{CM}] \nabla E^2 \quad (3.3)$$

where  $r$  is the radius of particle,  $\varepsilon_0$  is the permittivity in vacuum,  $\varepsilon_m$  is the relative permittivity of suspending medium,  $\nabla E^2$  is the gradient of the square of electric field and the  $\operatorname{Re}[f_{CM}]$  is real part of  $f_{CM}$  called Clausius-Mossotti (CM) factor. This factor is given by

$$f_{CM} = \frac{\varepsilon_p^* - \varepsilon_m^*}{\varepsilon_p^* + 2\varepsilon_m^*} \quad (3.4)$$

where  $\varepsilon_p^*$ ,  $\varepsilon_m^*$  are the complex permittivity of the particle and medium, respectively. It can be expressed by

$$\varepsilon^* = \varepsilon - j \frac{\sigma}{\omega} \quad (3.5)$$

where  $\varepsilon$  is relative permittivity,  $\sigma$  is conductivity and  $\omega$  is the radian frequency of electric field. This real part of CM factor defines direction of force due to all other terms are positive. If it is a positive value, positive DEP is derived and particles are attracted. Otherwise particles are repelled by negative DEP.

Therefore, it is possible to estimate not only the magnitude but the direction of the DEP force on each cell through the equation above. Here, we investigated the

direction of blood cells in respect to frequency and the gradient of electric field, which are the only things we can control without changing the sample.

### 3.2.2.1 Frequency effect of DEP

We are going to investigate the frequency effect of AC voltage which apply DEP force on blood cell. The frequency effect could be estimated by substituting Eq. (3.3) into Eq. (3.2).

$$\begin{aligned}
 f_{CM} &= \frac{\left(\varepsilon_p - \frac{j\sigma_p}{\omega}\right) - \left(\varepsilon_m - \frac{j\sigma_m}{\omega}\right)}{\left(\varepsilon_p - \frac{j\sigma_p}{\omega}\right) + 2\left(\varepsilon_m - \frac{j\sigma_m}{\omega}\right)} \\
 &= \frac{(\varepsilon_p - \varepsilon_m)(\varepsilon_p + 2\varepsilon_m)\omega^2 + 3(\varepsilon_p\sigma_m - \varepsilon_m\sigma_p)\omega j + (\sigma_p - \sigma_m)(\sigma_p + 2\sigma_m)}{(\varepsilon_p + 2\varepsilon_m)^2\omega^2 + (\sigma_p + 2\sigma_m)^2}
 \end{aligned} \tag{3.6}$$

Since the effective term of this equation is just real part, Eq.4 can be simplified to

$$Re[f_{CM}] = \frac{(\varepsilon_p - \varepsilon_m)(\varepsilon_p + 2\varepsilon_m)\omega^2 + (\sigma_p - \sigma_m)(\sigma_p + 2\sigma_m)}{(\varepsilon_p + 2\varepsilon_m)^2\omega^2 + (\sigma_p + 2\sigma_m)^2} \tag{3.7}$$

The range of the CM factor is placed on  $-0.5 \leq f_{CM} \leq 1.0$  by the Eq.(3.5), thus the magnitude of the CM factor is limited even when  $\varepsilon^*_p \rightarrow \infty$  or  $\varepsilon^*_m \rightarrow \infty$ . Therefore it was possible to draw the magnitude of real part of CM factor in respect to electric field frequency using Eq.(3.5).

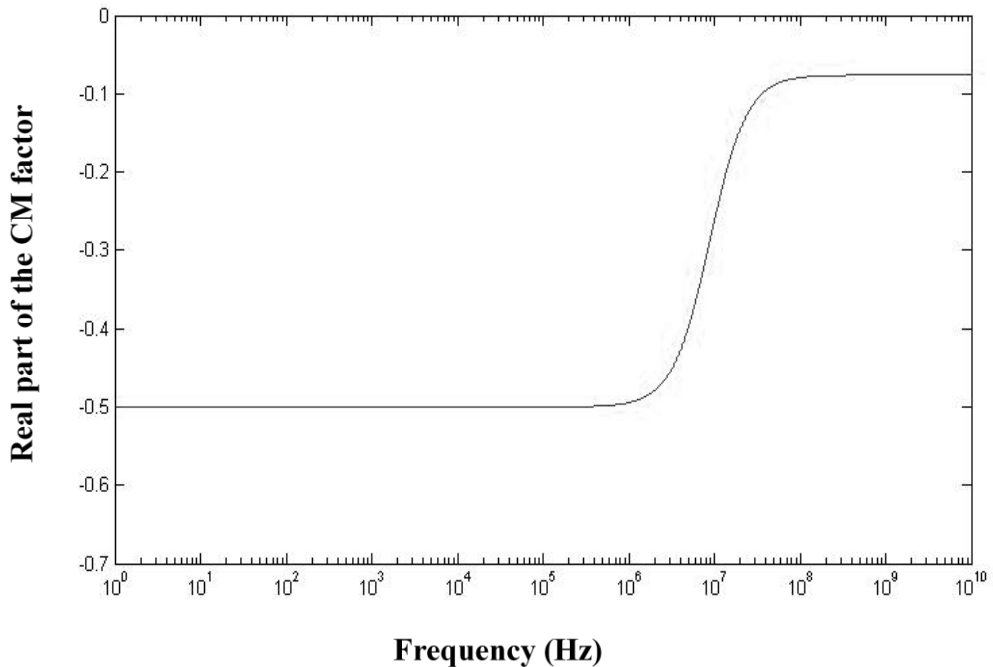


Figure 3-13. Real part of the CM factor change depending on electric field frequency.

The graph in Figure 3-13 is the result, which informs us of the DEP direction. We calculated it by substituting relative permittivity and conductivity of diluted plasma (80, 55 mS/m) and blood cell (63, 1 $\mu$ S/m) into the equation, separately [1]. The CM factor is always negative value over a frequency range shown. The maximum absolute value of the factor is 0.5 while frequency is below 1 MHz and it falls down with higher frequency. It was very important to know this as prior information

because we did not have to take time to learn about attractive force induced by positive DEP. Therefore, we designed electrode shapes, applying only negative DEP and used quite low frequency.

### 3.2.2.2 DEP force on RBC

Now we are considering the DEP force on blood cell, RBC, depending on electrode design. Various designs of non-uniform DEP electrodes are shown in Figure 3-14. We already confirmed that only negative DEP occurred on the whole frequency range in our experimental condition. In addition, in Eq. (3.1), the gradient of AC electric field mostly determines the magnitude of DEP force. The electric field is highly influenced by the electrode shape. Therefore, we are going to estimate the magnitude of DEP force using finite elements analysis (FEA).

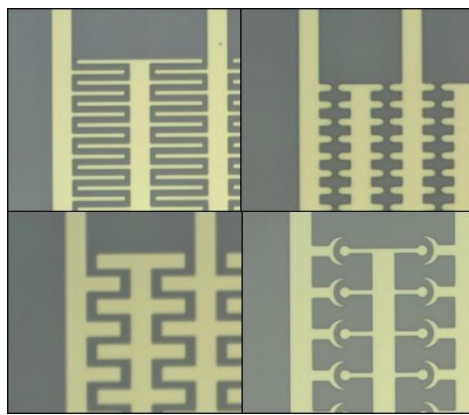


Figure 3-14. Various shapes of non-uniform DEP electrode for blood cell separation. Yellow area is the gold electrode, and grey area is the membrane of Si<sub>3</sub>N<sub>4</sub>.

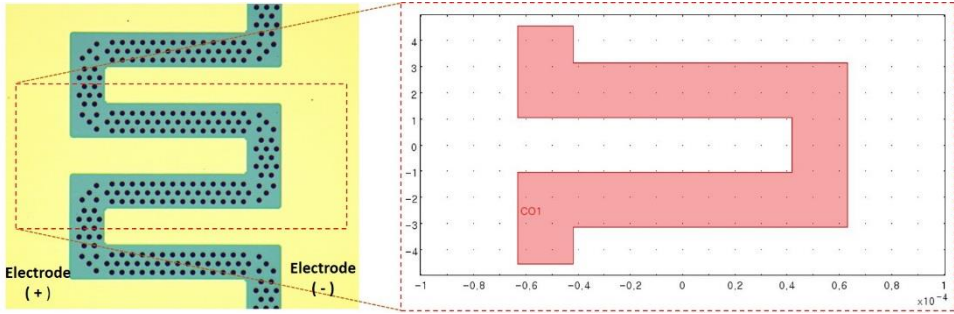


Figure 3-15. Finite element analysis (FEA) modeling of gap between the positive and negative electrode using COMSOL 3.5.

In Figure 3-14, various shapes of DEP electrode are presented. Among them, rectangle shape of electrode design is analyzed by FEA using COMSOL 3.5 in Figure 3-15. Recent version of COMSOL (over 4.2) supports DEP simulation package. However, we could not fully understand detail calculation process of the simulation package because they are using the complex multiphysics method which combines electrokinetics and hydrodynamics in microfluidics. Instead of the complex automatic tool, we just acquired data on electric field using COMSOL 3.5. Based on equation (3.3), we manually calculated the gradient of electric field and DEP force on blood cell.

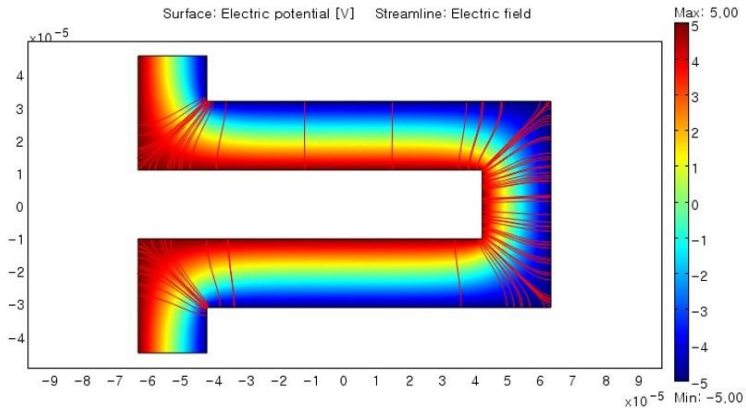


Figure 3-16. FEA result for electric field between electrodes, when voltages are positive (+5 V) and negative (-5 V) on each electrode.

Figure 3-16 represents the result of FEA on electric fields between DEP electrodes, when positive voltage is +5 V, and negative voltage is -5 V on each electrode. The streamline at the corner of an electrode is denser than that on parallel electrodes. Dense streamline means that the change of electric field is large. Therefore, DEP force at corner electrode is larger than the force on parallel electrode.

In addition, depending on the mesh size, the result could be different. In the following Figure 3-17 and 18, the DEP force calculation result could be compared with the mesh size (or the number of mesh). When the mesh size is smaller, the accuracy of FEA result is higher. In the case of large mesh size in Figure 3-17. (c), there are many singularity and error points. The error comes from the non-uniform and insufficient mesh size. In conclusion, we have succeed in finding out the appropriate mesh size which can support reasonable and trustable DEP force calculation result in Figure 3-18 (c).

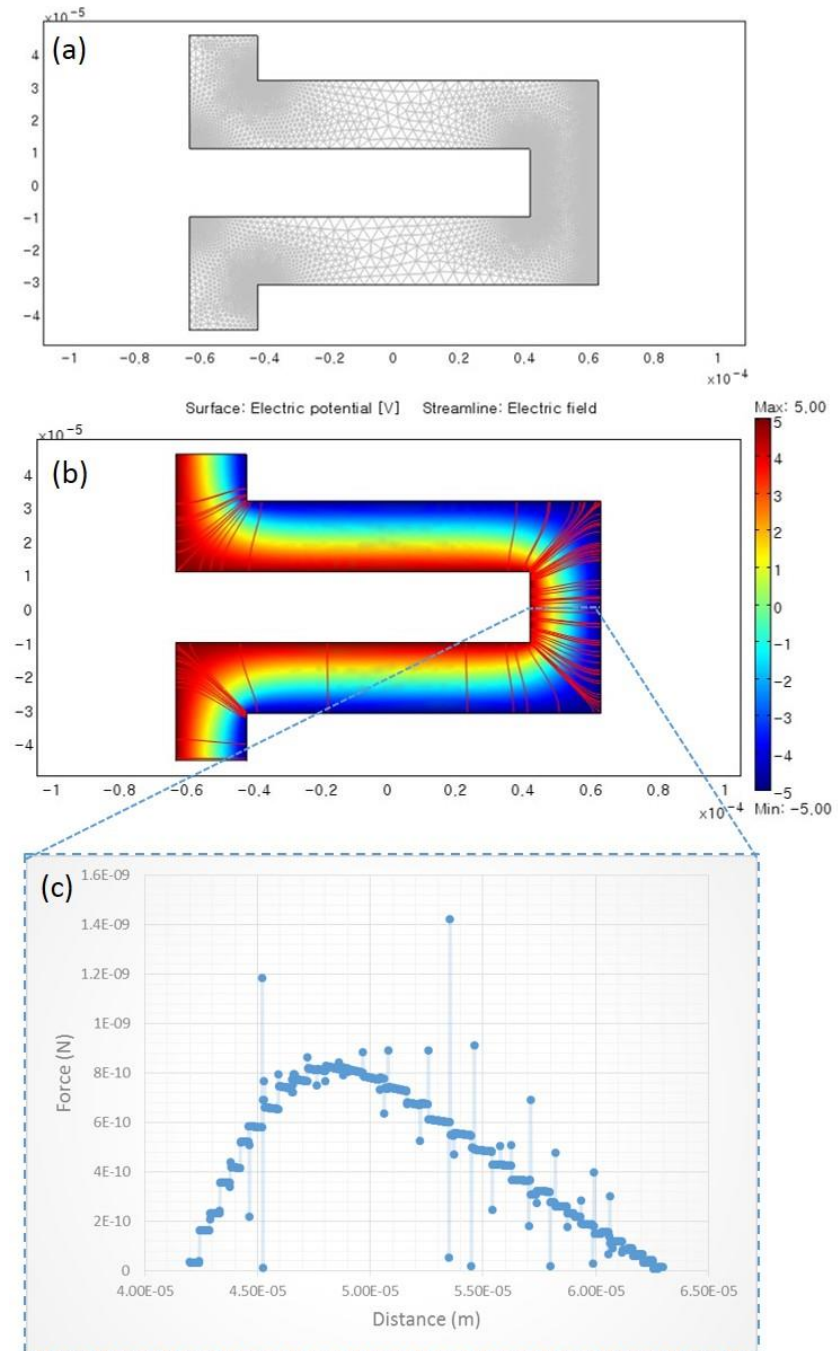


Figure 3-17. FEA for DEP(number of mesh=39,097), (a) mesh, (b) electric field, (c) DEP

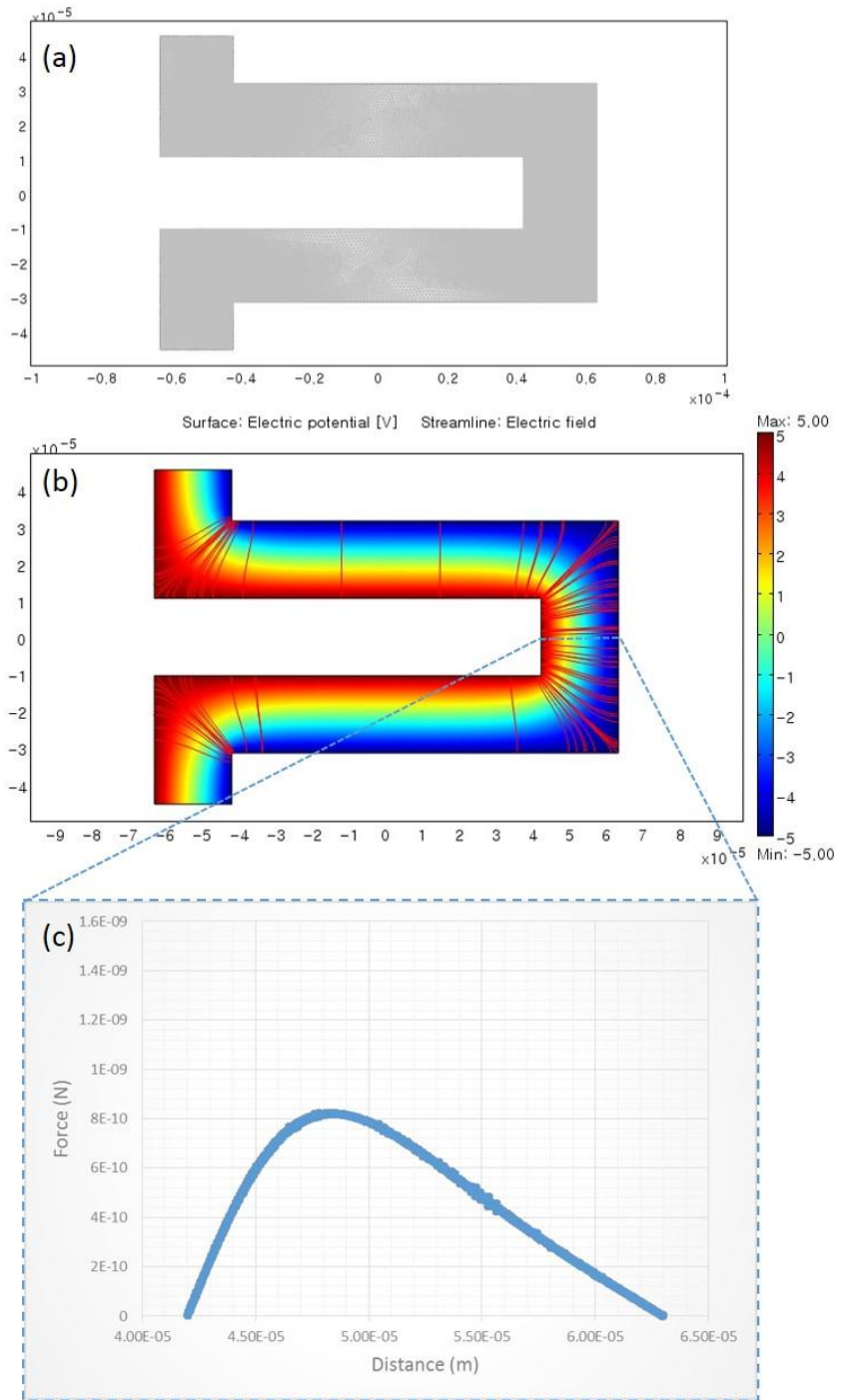


Figure 3-18. FEA for DEP(number of mesh=625,552), (a) mesh, (b) electric field, (c) DEP

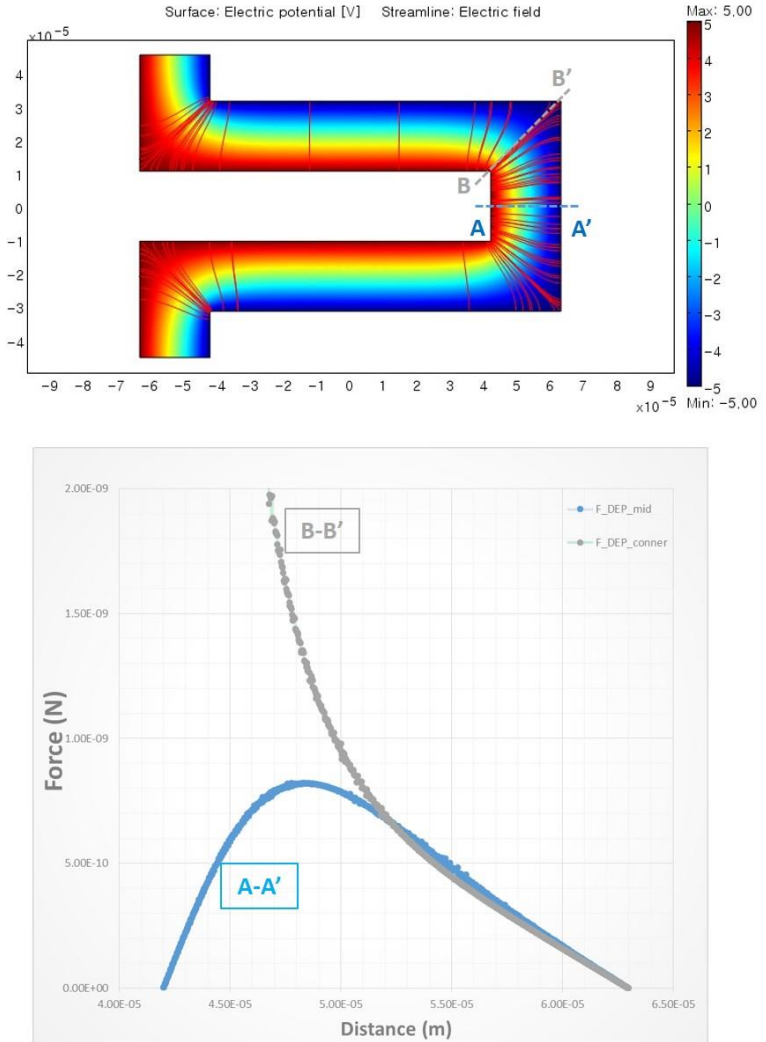


Figure 3-19. DEP force comparison between mid-line and corner-line.

Here we are going to compare the DEP forces at mid-area and corner-area. As shown in Figure 3-19, DEP force at corner-line (B-B') is larger than the force at mid-line (A-A'). As it gets closer to the sharp corner (Figure 3-19 B), DEP force is increases sharply. This result is easily anticipated from the electric field streamline density. However, we need an exact value to compare DEP force and hydrodynamic force.

### 3.2.3 Hydrodynamic drag force on blood cell

If there is no DEP force, most particles could be sucked into a vortex caused by pores and then get stuck. In order to prevent pore blocking, DEP force has to exceed the drag force. In general, hydrodynamic drag force  $F_{Drag}$  on a spherical particle is expressed by

$$F_{Drag} = -6\pi\mu ru \quad (3.8)$$

where  $\mu$  is fluid viscosity,  $r$  is the radius of particle and  $u$  is fluid velocity. However,  $u$  is difficult to derive using analytical solution. Instead of the vertical velocity inside pore,  $u$  represents the horizontal velocity on the membrane. Figure 3-19 shows the flow field where the fluid goes toward the pore, and the pores are placed at the gap between DEP electrodes on the membrane. Then, the flow near the pores gets fast, and the flow far-off the pores gets slow. In fact, the total area of the pore array on membrane determines the flow velocity and flux. For the large area of pores, the total flow rate increases, but the flow velocity through the pore is contradistinctively decreased. Therefore, we are going to investigate the effect on flow velocity with various sizes and number of pores using numerical simulation.

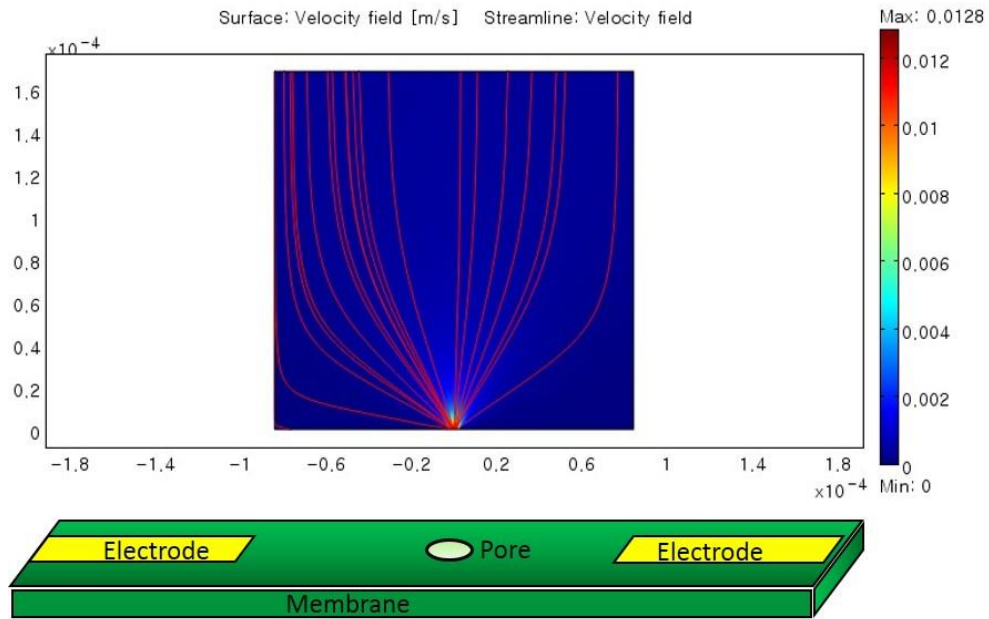


Figure 3-20. Schematic and FEA result about flow field near the pore ( $3 \mu\text{m}$ ).

Figure 3-20 represent the velocity field and streamline when uniform pressure is applied on the top-side surface where the pore ( $3 \mu\text{m}$ ) is the outlet. The velocity field changes and density of the streamline is very dynamic near the pore. The electrode thickness ( $0.1 \mu\text{m}$ ) and shape (rectangle) on the membrane are negligible in analysis of the flow. Actually, the process of mesh construction for FEA is difficult near the very thin electrode edge, and the calculation results which are applied to the electrode shape are not effective. We are going to apply these assumptions and conditions to the next analysis about pore size effect and number of pore.

### 3.2.3.1 Fluid velocity with pore size

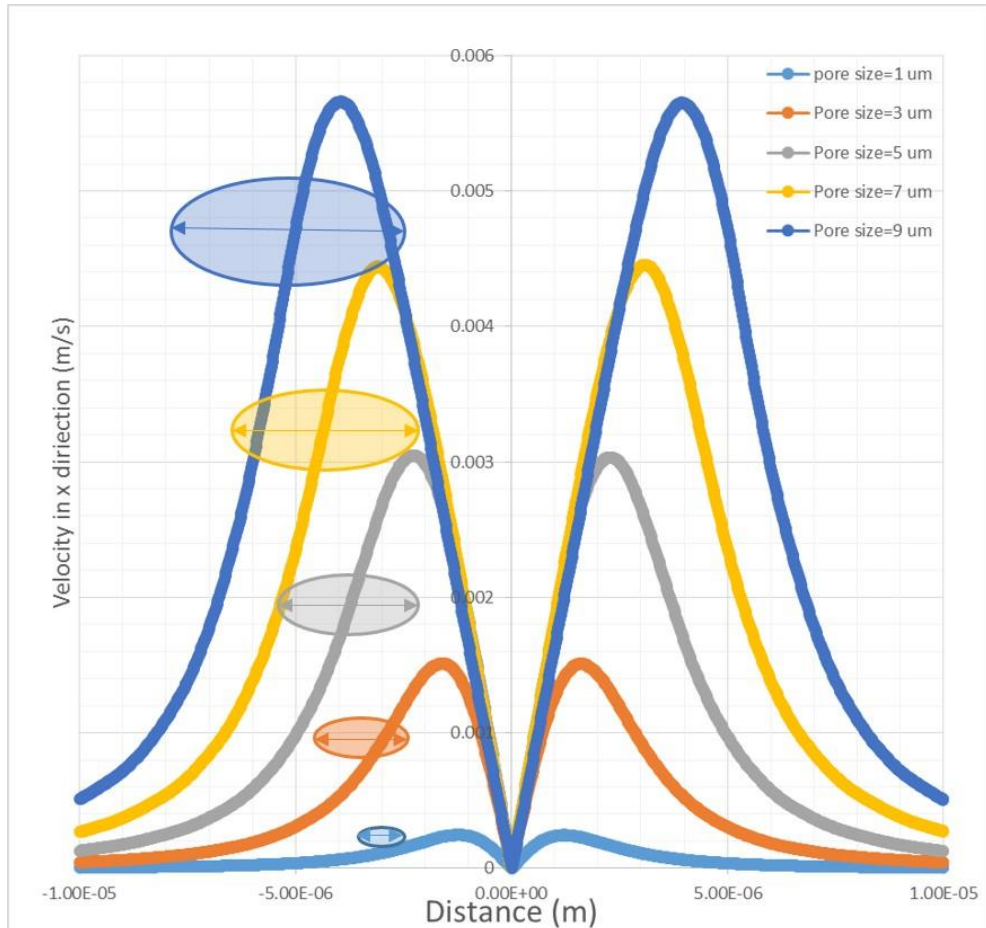


Figure 3-21. Horizontal flow velocity with various pore sizes on the membrane surface. The diameter of pore sizes are 1, 3, 5, 7, 9  $\mu\text{m}$ , respectively.

Now, we are going to estimate the effect of “pore” size on membrane. In Figure 3-21, the horizontal fluid velocities on the membrane surface are described with different pore sizes ranging from 1  $\mu\text{m}$  to 9  $\mu\text{m}$ . The result shows that the horizontal velocities near the pore edge are fast in speed and flow loses speed as it gets farther from the edge. In this FEA, we assume that the distance from the membrane surface

is 1  $\mu\text{m}$  because of RBC thickness, which is 2~3  $\mu\text{m}$ . In addition, only one pore is placed at the center between DEP electrodes. As a result, the velocity of a small pore is slower than the velocity of a large pore. This means that the hydrodynamic drag force, which acts on blood cells, dramatically increases when the pore size is large. Therefore, the hydrodynamic force is larger than the applied DEP force. Then, “virtual barrier” which prevents the blood cell blocking on the pore does not work properly.

Also, the pore sizes more than 5  $\mu\text{m}$  are not enough to filter out blood cells (5 ~ 7  $\mu\text{m}$ ). Moreover, large RBC ( $> 5 \mu\text{m}$ ) could pass through the gap under 4  $\mu\text{m}$  size because of its flexible and deformable characteristics [76]. In this sense, smaller pore size is better for blood cell filtration. Nevertheless, the throughput of small pore array membrane could be too low and the processing time might take too long.

In addition, the micromachining fabrication under 1  $\mu\text{m}$  size of pore is difficult and costly. In conclusion, among the various pore sizes in Figure 3-20, pore size of 3  $\mu\text{m}$  is relatively well-chosen for modelling and analysis of flow considering the aspects of filtration and throughput.

### 3.2.3.2 Fluid velocity with number of pores

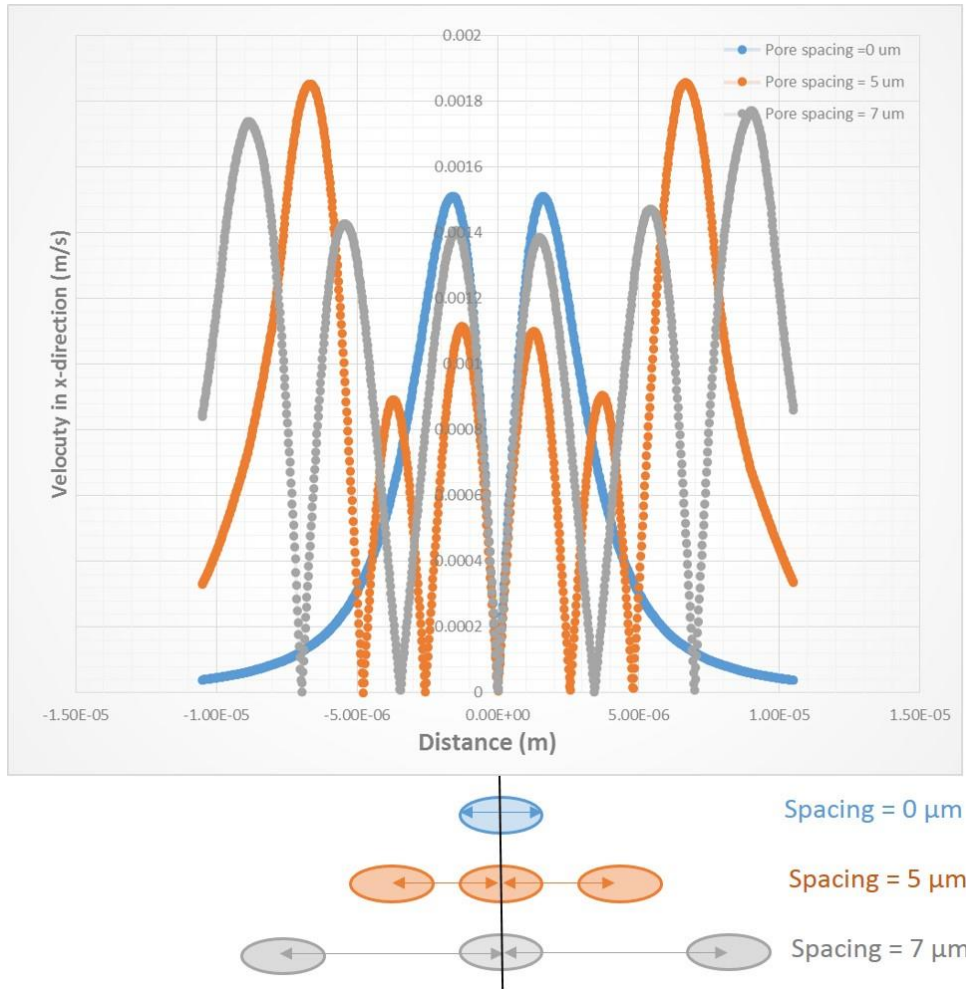


Figure 3-22. Horizontal flow velocity of different spacing between pores. The diameter of a pore is  $3 \mu\text{m}$  and the spacing between pore centers is  $0, 5, 7 \mu\text{m}$ .

Here, we are going to evaluate the effect of pore “array.” Based on the previous chapter result,  $3 \mu\text{m}$  pore size is suitable for blood cell separation FEA. In this analysis result as shown in Figure 3-22, different spacing between pores is positioned on the membrane. The spacing between centers of pore is  $0, 5, 7 \mu\text{m}$ , so the gap

between pores is 0, 2, 4  $\mu\text{m}$  respectively. The orange-red and the grey lines represent the results of 5  $\mu\text{m}$  and 7  $\mu\text{m}$  spacing case. At the center pore, the velocity of multi-pore case is faster than the single-pore case. On the other hand, at the outside, the velocity of single-pore is dramatically reduced, but the velocities of multi-pore are greater than before. The reason for this velocity variation is the increase of total flow rate throughout the pores. At the same applied pressure on fluid, the ratio of sum flow rate passage through pores is (1: 1.76: 2.08) on the blue, orange-red, and grey lines in Figure 21, respectively. Comparing the single-pore and multi-pore, the total area difference causes the variation. However, with the same pore area, the wide spacing result (7  $\mu\text{m}$ ) shows higher total flow rate than the narrow spacing result (5  $\mu\text{m}$ ). We guess there is the interference between pores, and the narrow spacing of pores is better in reducing the velocity near pores. We postulate that there is reduction of hydrodynamic drag force with decrease of velocity.

In Figure 3-23, the horizontal velocity of various pore are evaluated. The number of pores ( $N= 1, 3, 5$ ) are compared in the fixed pore spacing (4  $\mu\text{m}$ ) and gap (1  $\mu\text{m}$ ) between pores. The orange-red and the grey lines represent the result of 3 pores and 5 pores effects. As the number of pores increase, the maximum velocity around the pores decrease (1 pore = 0.00151 m/s, 3 pores = 0.00085 m/s, 5 pores = 0.000762 m/s). In addition, the ratio of sum flow rate is (1: 1.70: 1.69) on the blue, orange-red, and grey lines in Figure 3-22, respectively. The interference between pores makes the fluid velocity to even out in level. Moreover, more number of pores result in higher evenness effect on flow rate.

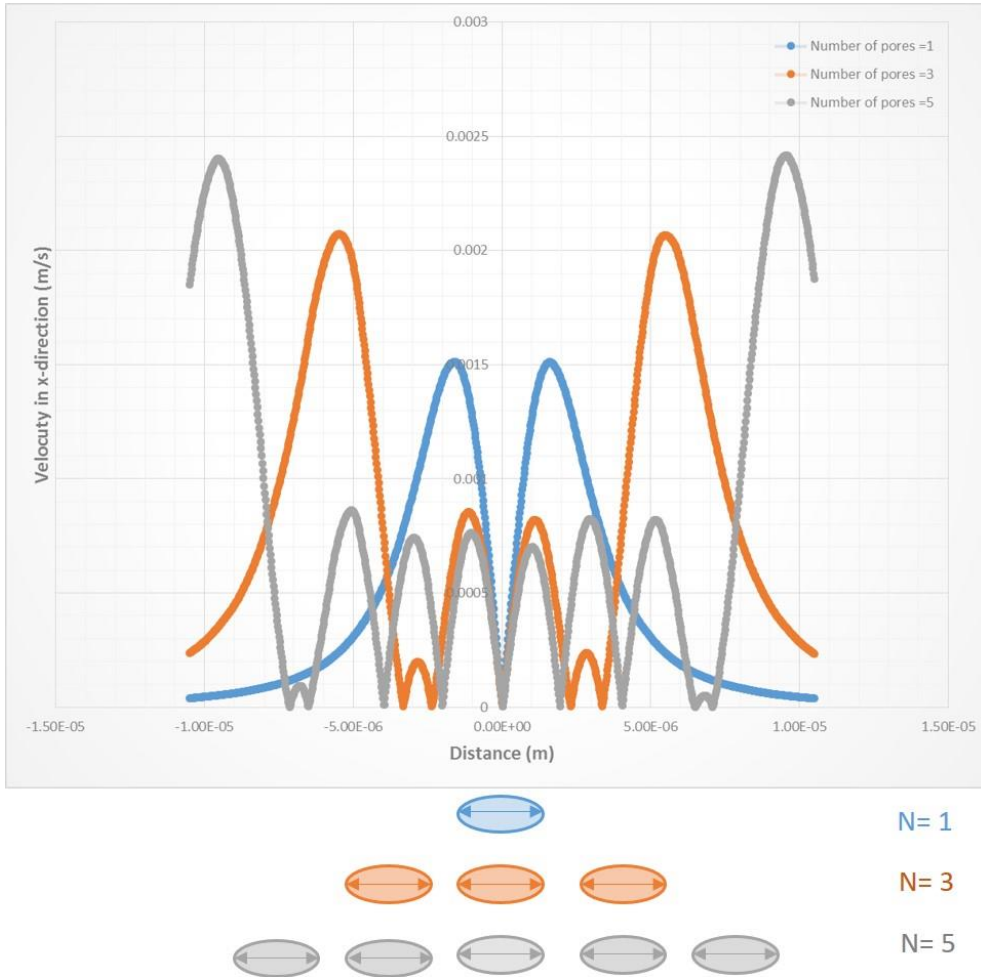


Figure 3-23. Horizontal flow velocity of different pore numbers ( $N=1, 3, 5$ ). The diameter of a pore is  $3 \mu\text{m}$  and the spacing between pore centers is  $4 \mu\text{m}$ .

In conclusion, we investigate the flow velocity to calculate the hydrodynamic drag force. Multi-pore is better than single-pore in the aspect of low drag force and high throughput, and we confirm that by FEA with various pore size ( $d$ ), spacing (gap) and number ( $N$ ).

### 3.2.4 Balance between DEP vs. Hydrodynamic drag forces

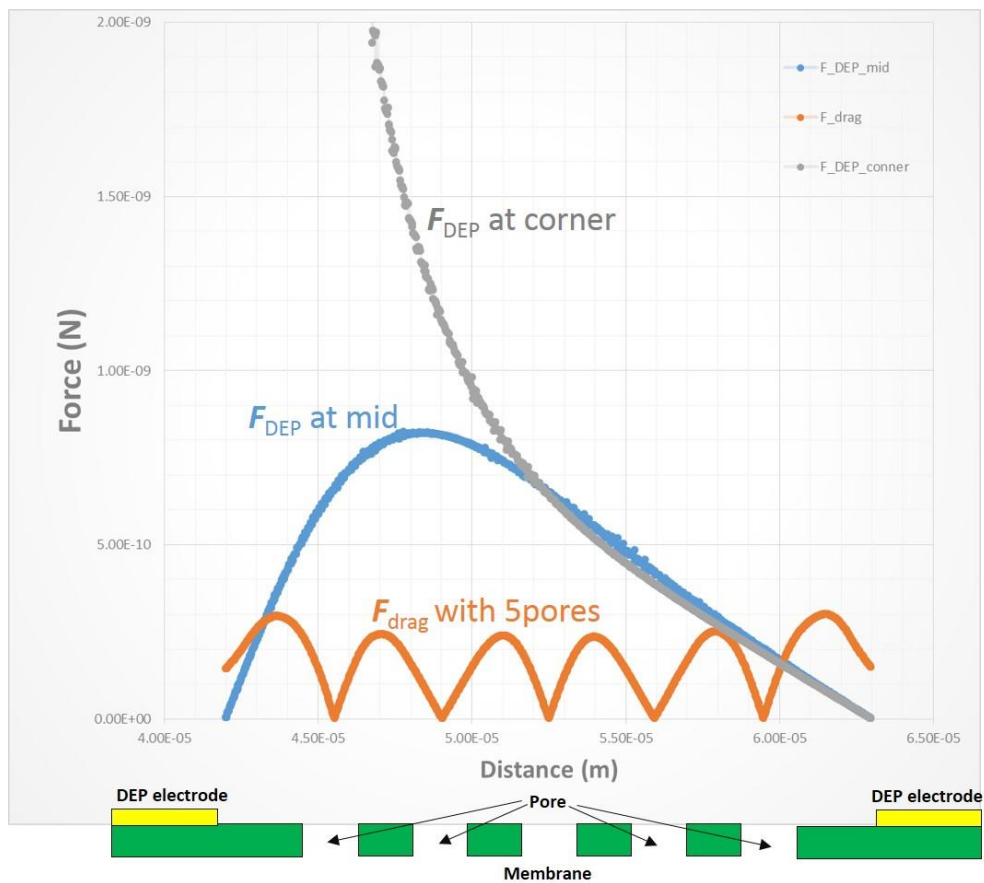


Figure 3-24. Force balance between  $F_{DEP}$  and  $F_{drag}$  on membrane. (Blue line:  $F_{DEP}$  at mid,

grey line:  $F_{DEP}$  at corner, yellow red line:  $F_{drag}$ )

In Figure 3-24,  $F_{DEP}$  at mid and corner are compared with  $F_{drag}$ , of which data are the previous chapter results. If RBC moves on the pores,  $F_{DEP}$  and  $F_{drag}$  are applied on the particle simultaneously. RBC is repelled from the pores because both of  $F_{DEP}$  are larger than  $F_{drag}$ . This graph denotes that the blood cell which prevents fluid passage

through pores could be effectively removed and blood filtration process would work well.

In summary, using calculation and FEA results, we confirm that our blood filtration system could correctly operate.  $Re[f_{CM}]$ ,  $\nabla E^2$  and  $u_{fluid}$  can be easily tuned without changing materials, but all other terms are difficult to change. Since electric field gradient is highly dependent on electrode shape, we optimized the various shapes of electrode by testing micro-polystyrene beads and FEA simulation electric field results. In addition, fluid velocity is proportional to the diameter of pore and area of pore array on membrane. We will move on to compare these theoretical results with experimental results in the next chapter.

### 3.3 Materials and methods

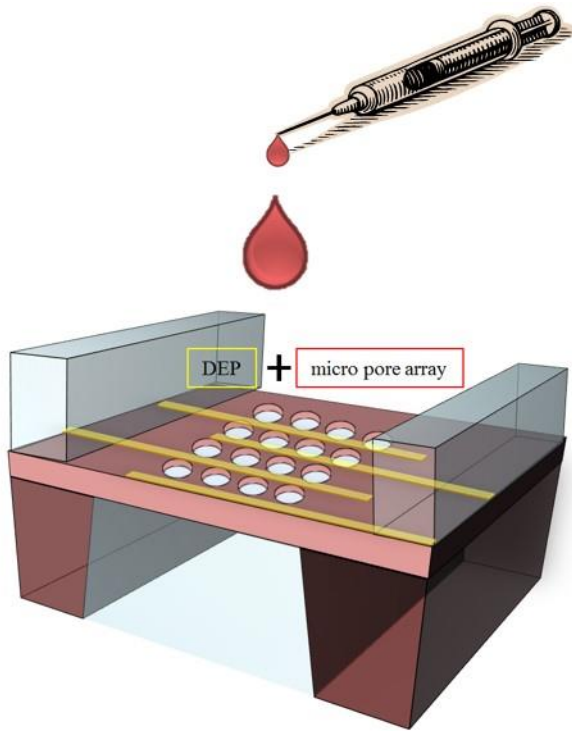


Figure 3-25. Concept of blood plasma extraction device and components. The system consists of blood sample and MEMS filter. The MEMS filter combines DEP function and micro pore array which is made by microfabrication process.

In Figure 3-25, the system consists of blood sample and MEMS filter. The drop of blood is put into the membrane which combines DEP function and micro pore array. From now on, the blood sample preparation and MEMS filter fabrication process will be discussed. Also experimental equipment setup and procedures are going to be analyzed. Moreover, detail measurements and evaluation methods will be evaluated.

### 3.3.1 Blood sample preparation



Figure 3-26. Phlebotomy: Syringe draw procedure [55], Venipuncture and EDTA tube.

Whole blood sample was drained from healthy adult donor through venipuncture. An ethylenediaminetetraacetic acid (EDTA) vacutainer tube prevented blood coagulation with anticoagulant coating on the storage inner wall. The whole blood was diluted with isotonic buffer with different concentrations. This isotonic buffer was made up of 8.5% (w/v) sucrose and 0.3% (w/v) dextrose in 1× phosphate buffered saline (PBS). BSA powder was also added to the solution with concentration 1% (w/w). Depending on the dilution ratio, the buffer concentration varied like shown in Table 3-4. The conductivity change could show effect on force of DEP especially in  $f_{CM}$  from Eq. (3.4). Not only the amplitude but also the direction of DEP force might vary with the change. However, as shown in Table 3-4, the variation of conductivity was slight. Also, the number of blood cells were different on dilution ratio in Figure 3-27. At each experiment, 20  $\mu\text{L}$  of diluted blood was injected into the microchannel inlet at a time.

Table 3-4. Conductivity change of various dilution ratio of blood and buffer.

	<b>Isotonic Buffer</b>			
<b>Concentration (v/v)</b> <b>(Blood : Buffer)</b>	Buffer only	1:100	1:40	1:10
<b>Conductivity (mS/cm)</b>	12.20	12.10	12.01	11.75

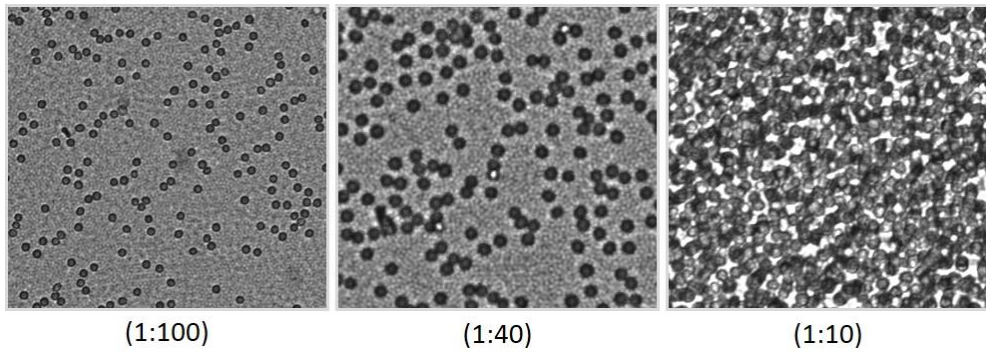


Figure 3-27. Inverted microscope images of RBC in various dilution ratio.

### 3.3.2 MEMS integration process

Figure 3-28 represents the integrated devices. There are 2 types of MEMS filter devices. Both types are integrated with silicon part and PDMS microchannel part. The right one is the first version of device and the left one is the second version. As you can see, the size of silicon part and microchannel part is much larger than the left one. The large device is convenient to handle for experiment, but it is not a cost-effective design because of productivity in one silicon wafer. The numbers of devices from 4-inch wafer were 17 in the first version and 65 in second version, resulting in enhancement of productivity of more than 288%. This enhancement could improve the mass-productivity and support statistical performance analysis. Moreover, if 4-inch wafer could change to 6-inch or 8-inch wafer, the increase of productivity would be much better than the previous one. In addition, in the second device design, tubing parts which connect the buffer inlet and outlet are removed, so the later device is suitable for integration with detection part and other parts. In the next chapters, the experiment results are from both versions of MEMS devices.

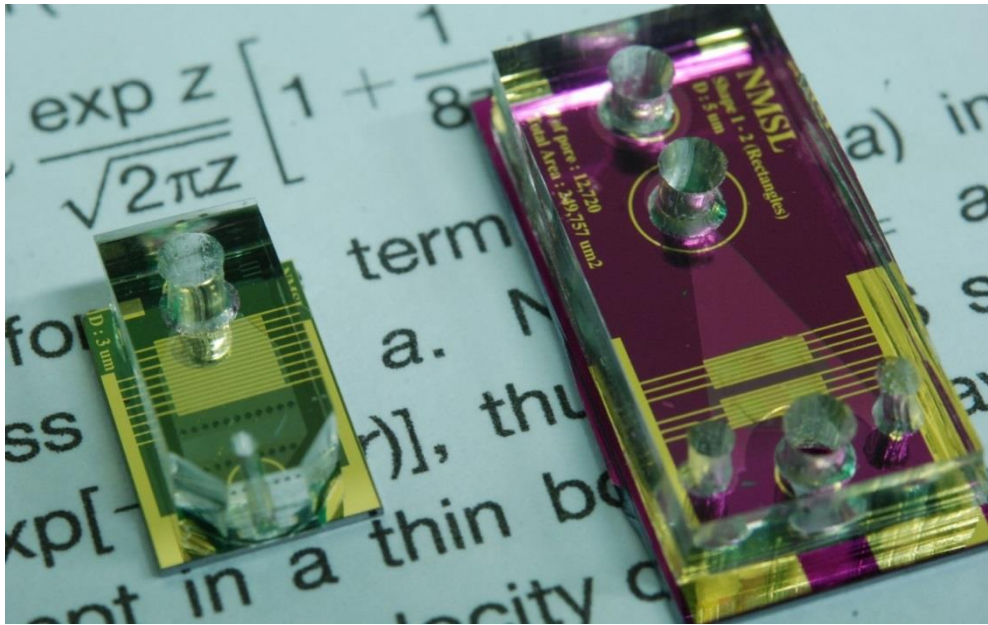


Figure 3-28. MEMS filter devices. The right one is the first version device ( $25\text{ mm} \times 12\text{ mm}$ ) and the left one is the second version device ( $11.75\text{ mm} \times 8.45\text{ mm}$ ).

### 3.3.2.1 MEMS filter design

The cross-section view of schematic is in Figure 3-29. Fig.3-29 (a) is the first device version, and Fig.3-29 (b) is the second device design. Both designs consist of 3 parts; MEMS filter part (silicon &  $\text{Si}_3\text{N}_4$ ) and separate top and bottom microchannel parts. The different points are the small size of MEMS silicon part and bottom PDMS and plastic microchannel. This modification is to enhance the integration with other parts. The top microchannel has blood inlet venting holes—the blood inlet is the place to drop blood sample with venting holes acting to fill fluid without air trapping. Also PDMS channel helps the observation of blood cell movement through microscope due to transparent property. Then, MEMS filter part is composed of pore array and

DEP electrodes on  $\text{Si}_3\text{N}_4$  membrane. The bottom microchannel has the function of buffer injection, extraction and mixture. Each part is assembled by using the surface treatment method.

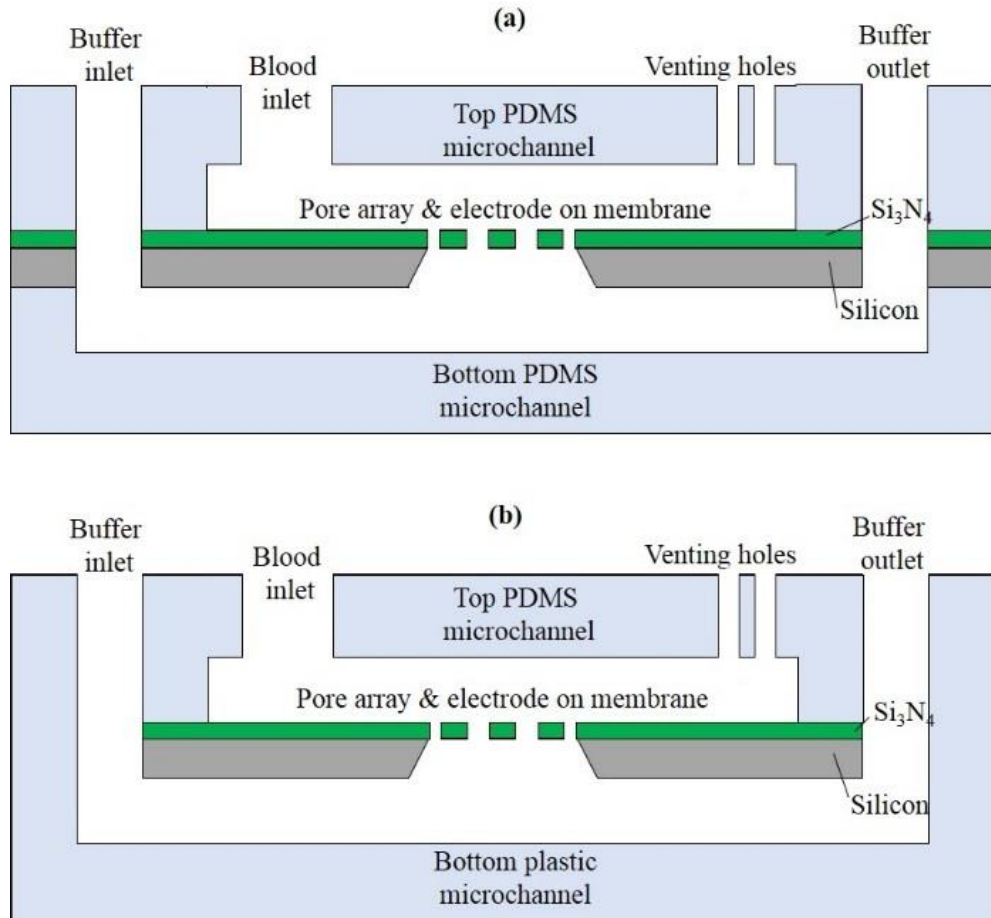


Figure 3-29. Cross-section view of the integrated MEMS filter and microchannels. (a) first design version, (b) second design version

### 3.3.2.2 Fabrication process

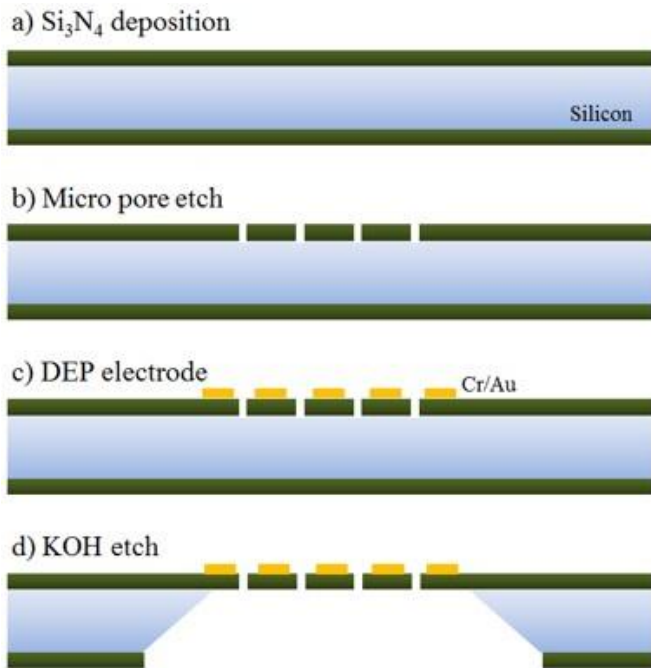


Figure 3-30. Fabrication process of MEMS filter. (a) Si<sub>3</sub>N<sub>4</sub> deposition on silicon, (b) micro pore array patterning on Si<sub>3</sub>N<sub>4</sub>, (c) gold electrode for DEP patterning, and (d) anisotropic KOH wet etching

Within MEMS filter, silicon part and fabrication process is briefly shown in Figure 3-30. The detailed outline of each step is explained in Table 3-5. Si 4-inch <100> wafer is the substrate material of this process. From bare Si wafer SPM clean process, micro pore array and gold DEP electrode are patterned and precisely aligned under 1 μm error (Karl-Suss, Germany).

The minimum feature size was 2 μm, which could be guaranteed by photolithography process, so the smallest pore diameter and the spacing between

pores were over 2  $\mu\text{m}$ . This value is essential to control performance of filter such as purity (selectivity) and throughput (recovery). The purity is determined by the pore size due to size exclusive separation mechanism between pore and RBC ( $= 2 \mu\text{m} : 6 \mu\text{m}$ ). Also, the recovery rate is affected by DEP electrode gap which decides the force amplitude with the non-uniform electric field. Moreover, total area of pore array fixed the passage of fluid flux through pores, and the area could be changed with spacing between pores on membrane.

Anisotropic wet etching, KOH etch, is used to make the free-standing  $\text{Si}_3\text{N}_4$  membrane which is a common material with high chemical resistance and good mechanical property [38]. Low stress nitride, which is deposited by low pressure chemical vapour deposition (LPCVD), could endure KOH (40% w/v) solution. Furthermore, thickness of membrane could be achieved under 1  $\mu\text{m}$  of which ratio between pore diameter and length is 4:1 ( $= 2 \mu\text{m} : 0.5 \mu\text{m}$ ).

PDMS microchannel is attached on MEMS substrate. The microchannel is made by PDMS replica molding process which was first reported to the public in 1996 [39]. From this traditional method, PDMS base and curing agent (catalyst) is mixed in 10:1 ratio and air bubble is removed by a vacuum chamber. After degassing process, PDMS is poured to microchannel patterned SU-8 mold. In a heating oven, PDMS with mold cures for 45 minutes. Then, PDMS microchannel is detached from the mold and is attached on MEMS filter part by using  $\text{O}_2$  plasma treatment (PVA Tepla microwave asher, Germany).

Table 3-5. Detail process protocol for MEMS filter and microchannel

Process	Step
SPM cleaning	$\text{H}_2\text{SO}_4 + \text{H}_2\text{O}_2 = 4:1$ @120 °C for 5 min D.I. water for 10 min Rinse & dry for 10 min
$\text{Si}_3\text{N}_4$ deposition	LPCVD (Low Pressure Chemical Vapor deposition) 650 °C, DSC: 300 sccm, NH <sub>3</sub> : 100 sccm, 200 mTorr
AZ 1512 PR (photoresist)	with HDMS: 500 rpm/5 s, 2500 rpm/7s 500 rpm/ 5 s, 4000 rpm/ 35 s
Photolithography	Soft bake @ 95 °C for 90 s 60 s exposure @ 15mW Developing @ AZ 300 MIF : D.I. water = 1:6 for 90 s Hard bake @ 110 °C for 3 min
Dry etching with P-5000	$\text{Si}_3\text{N}_4$ etching RF 600 W, 100 mTorr, 30 G, 4000 Å/min $\text{CHF}_3$ 15 sccm, $\text{CF}_4$ 10 sccm, Ar 10 sccm, $\text{O}_2$ 8 sccm
AZ 5214 PR (photoresist)	with HDMS: 500 rpm/5 s, 2500 rpm/7s 500 rpm/ 5 s, 4000 rpm/ 35 s
Photolithography	Soft bake @ 95 °C for 90 s 3 s exposure @ 15mW
- Image reverse process	Post exposure bake @ 95 °C for 180 s 60 s exposure @ 15mW Developing @ AZ 300 MIF : D.I. water = 1:6 for 90 s Hard bake @ 110 °C for 3 min
Cr/Au deposition with E-gun evaporator	Power 10 kW, $\text{N}_2$ gas Chamber pressure $\leq 5 \times 10^{-7}$ Torr in 30 min

Process	Step
Lift-off process	Acetone ≥ 10 min (ultrasonic could be used) Methanol 5 min, IPA 5min
KOH wet etching	40 w.t % (KOH : D.I.water) 80 °C for 10 hr Rinse in D.I. water without bubble and shower Manual N <sub>2</sub> gun dry carefully Bake 110 °C for 5 min
SU-8 PR (photoresist)	Surface treatment with O <sub>2</sub> plasma 20 s 500 rpm/ 5 s, 2500 rpm/ 30 s
Photolithography - 50 μm thickness	Soft bake @ 95 °C for 60 min 17 s exposure @ 15mW Post exposure bake @ 100 °C for 6 min Developing @ SU-8 developer for 15 min Hard bake @ 110 °C for 1 min
PDMS molding (Polydimethyl siloxane) - Sylgard 184	DC-184A : DC-184B = 10:1 mixing for 15 min 1 <sup>st</sup> degassing for 30 min with vacuum chamber PDMS pouring to SU-8 mold 2 <sup>nd</sup> degassing for 30 min with vacuum chamber 70 °C for 50 min

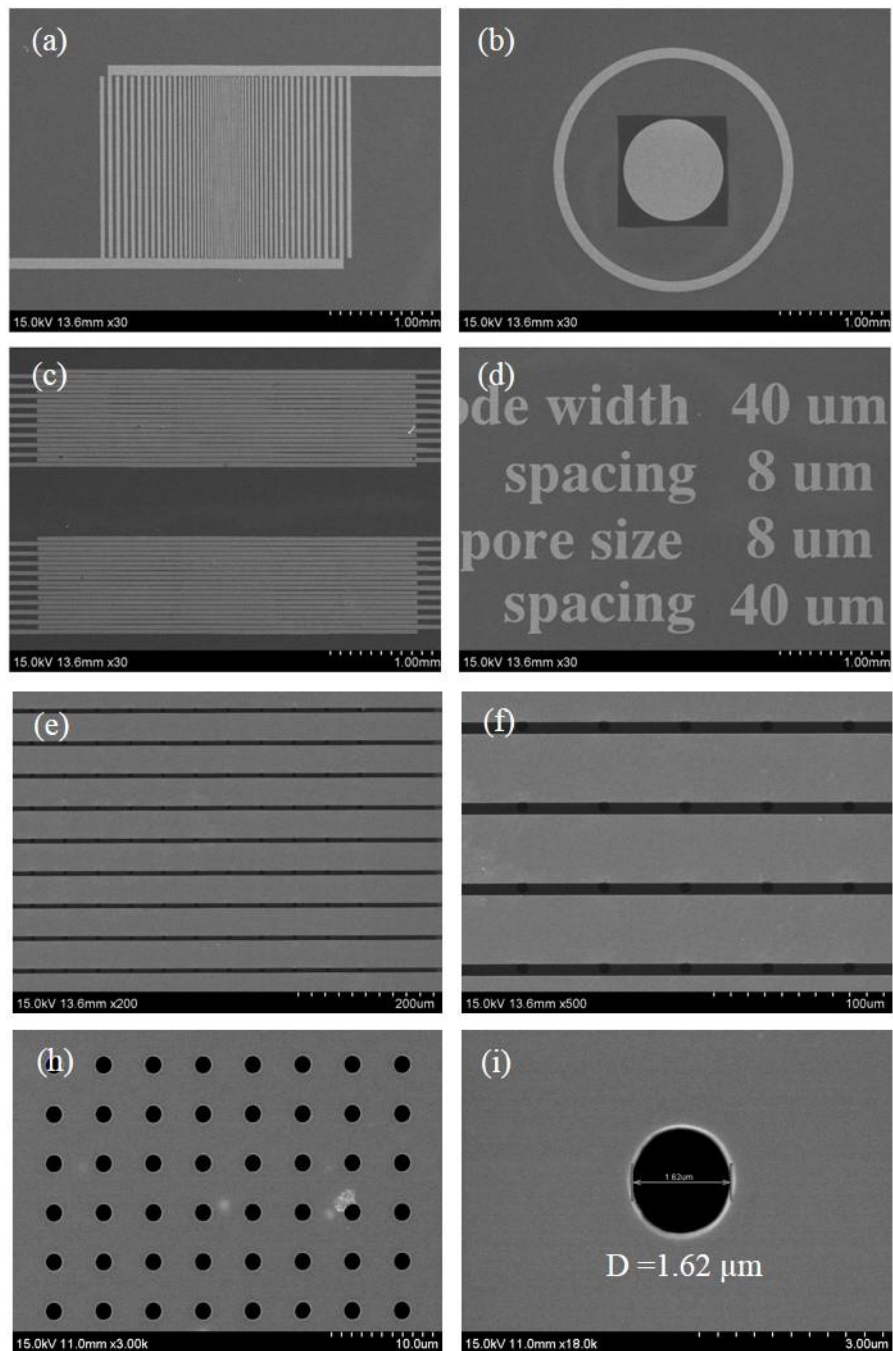


Figure 3-31. MEMS filter device images by SEM. (a), (c) DEP electrode, (b) membrane by KOH etching, (d) parameters, (e), (f) pore between electrodes, (h), (i) pores on membrane

### 3.3.3 Experimental setup

Variety of equipment are also used in MEMS fabrication as well as experimental processes in Figure 3-32. Electron microscope called SEM (Hitachi S-5000, Japan) is a beneficial microscope to confirm MEMS structure in Figure 3-31. In contrast, optical microscopes including inverted and metal microscopes are suitable for biological application like cell observation. Out of them, inverted microscope (Nikon Eclipse TE 2000-E, Japan) in Fig.3-32 (a) provides very clear images of blood cells and its motion where the substrate should be transparent. Therefore, only earlier DEP experiments with indium tin oxide (ITO) electrode on glass wafer was used to find out proper DEP electrode shape. Now metal microscope (Nikon Eclipse\_ME600L, Japan) in Fig.3-32 (b) became available to observe blood cells movement when DEP force is applied.

Furthermore, macroscopic CCD camera in Fig.3-32 (c) enables to measure the volume change of blood droplet before and after filtration. By comparing the volume difference, the amount of fluid passing through pore array membrane could be acquired. In addition, the blood droplet shape is measured by the pendant drop method with a tensionmeter (KRÜSS DSA100S) and the values are applied to the calculation. A function generator (Tektronix, USA) and probe station systems supply stable AC voltage to DEP electrodes.

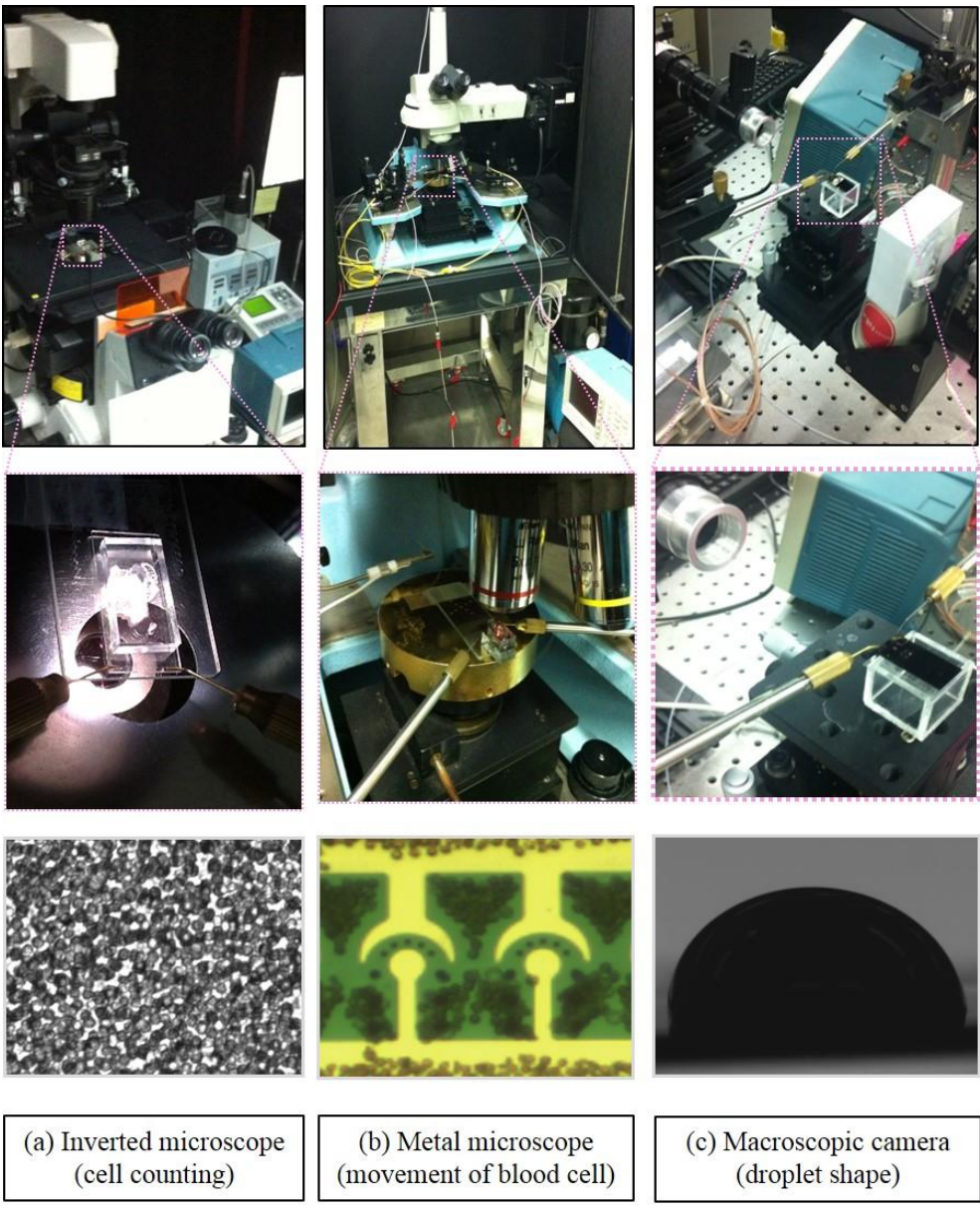


Figure 3-32. Experimental setups for blood filtration. (a) inverted microscope for cell counting, (b) metal microscope for DEP effectiveness of blood cell, and (c) Macroscopic camera for measuring blood droplet.

### 3.3.4 Evaluation methods

In order to evaluate the blood cell filter performance, we gather experimental data and calculate indicators from the data. The indicators are the purity and recovery of plasma from blood.

The purity means the level of efficiency in blood cells removal from whole blood. Based on size exclusive separation, blood cells which are larger than pore size could not transit through the pore array. However, due to high flexibility of blood cells, the pores could not perfectly filter them [76]. So the plasma passed through pores might contain some number of unfiltered blood cells. By counting the blood cells after separation, we derive the purity of plasma.

On the other hand, the recovery is defined as the ratio between the filtered plasma volume and the input blood volume. It is directly related to flow rate through the pore array. As mentioned in previous chapters, the flow rate is affected by total pores area and DEP effectiveness. The total pore area is determined by size and density of pores on membrane. Narrower spacing between pores increases density and large total area of pores. Moreover, DEP effectiveness involves the amplitude of force which could be varied by applying voltage or changing gap between electrodes or shape of electrodes. Thus, considering these parameters, the volume change of blood drop will be measured, and the amount of throughput will be induced.

The two indicators—purity and recovery have a trade-off relation, which means high purity equates with low recovery and low purity equates with high recovery. Consequently, we need to find an optimal value which satisfies both requirements.

## 3.4 Results and discussion

### 3.4.1 Experiments with microbeads

Experiments with microbeads were conducted to predict magnitude of DEP force depending on electrode shape, before dealing with red blood cells. Since many shapes can be designed on a photolithographic mask, different sorts were produced by a cycle fabrication process. Figure 3-32 in the previous chapter displays representative electrode types. We carried out tests with 0.5% w/v polystyrene microbeads without any function group. About 20  $\mu\text{L}$  of bead solution was injected to the device via inlet. We waited until channel was entirely filled with the solution. When motion of fluid was negligible, AC electric field was applied using a function generator. As presented in Figure 3-33, it was impossible to figure out electrode array due to high amount of beads, but almost all of them were swept away from the intended area and electrode shape became notable. Here, the intended area meant the region where we expected beads to be under repulsion force, the place keeping short distance between an electrode pair. Figure 3-33 (b), (c), (d), (e) are some examples illustrating particle movements. The working voltage was higher than 5 V<sub>pp</sub> (offset: 0 V) and AC frequency was around 100 kHz (sine wave). These processes were performed under 2 minutes.

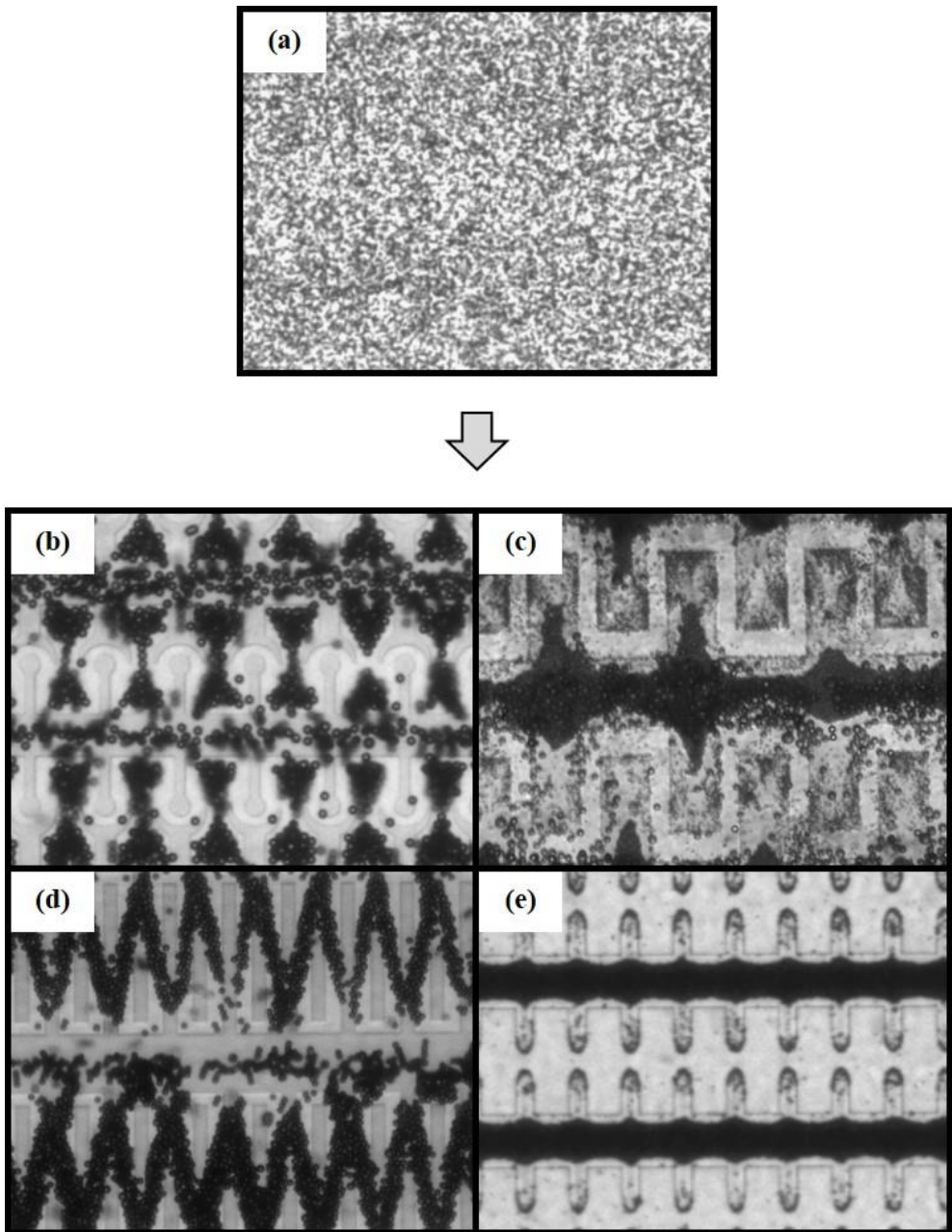


Figure 3-33. Inverted microscope image for DEP with microbeads. ITO is used for DEP electrode, and substrate is glass wafer. (a) before the voltage applied and after the voltage turned on. Beads were arranged differently by the distinct electrode arrays such as the shapes of (b) crescent, (c) crossed rectangles, (d) narrow crossed rectangles and (e) fingers.

### 3.4.2 Electrode shape optimization

Experiments with microbeads were conducted to predict magnitude of DEP force depending on electrode shape. We progressively increased the DEP voltage from zero and the frequency as well. As the input voltage had higher AC field, larger DEP force was applied. However if the voltage was higher than a certain level, electrolysis was generated and resulting in all electrodes burning out. On the contrary, if the frequency was lower than tens of kHz at 5 V or more, electrolysis occurred as well.

Although DEP effectively worked as shown in Figure 3-33, since ITO-glass wafer did not have pores, it was unable to measure the drag force caused by viscous effect. Consequently, the selected shapes were fabricated on a silicon nitride wafer which contained pores and was then tested with beads again. Viscous effect made the results dissimilar. After comparing the results, we chose two shapes which showed the highest efficiency; the results are as presented in Figure 3-34. We brought these decisions into experiments with real blood cells.

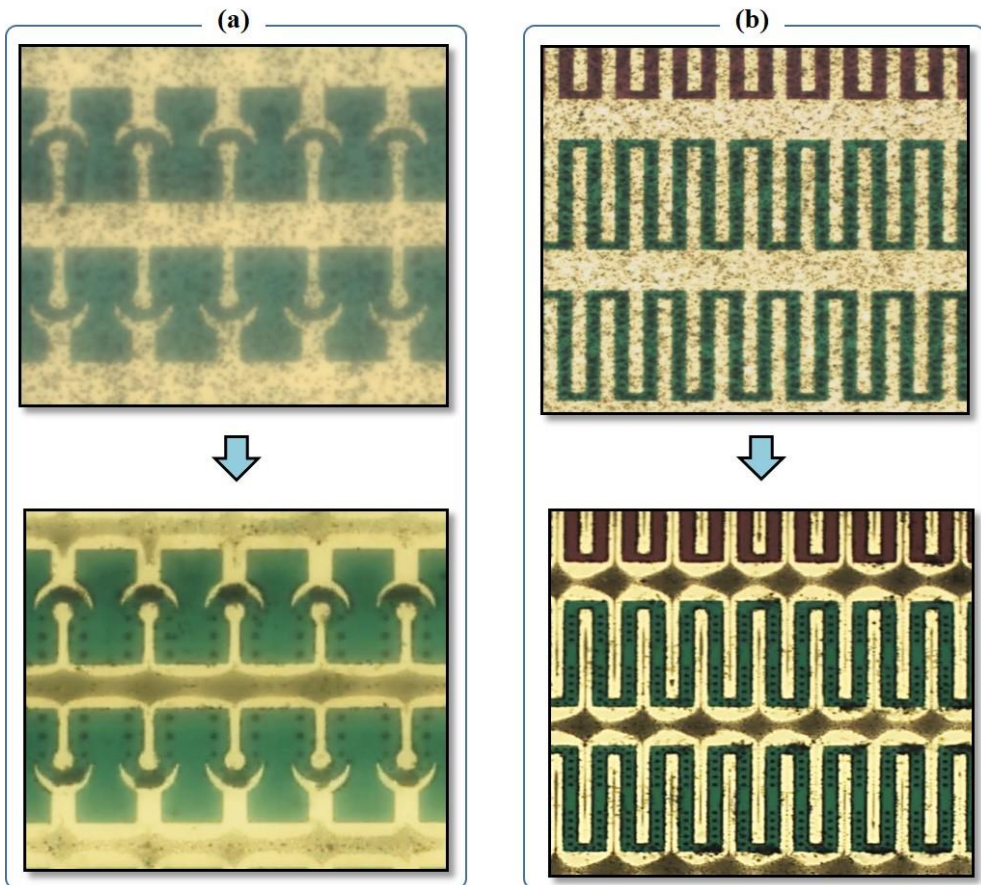


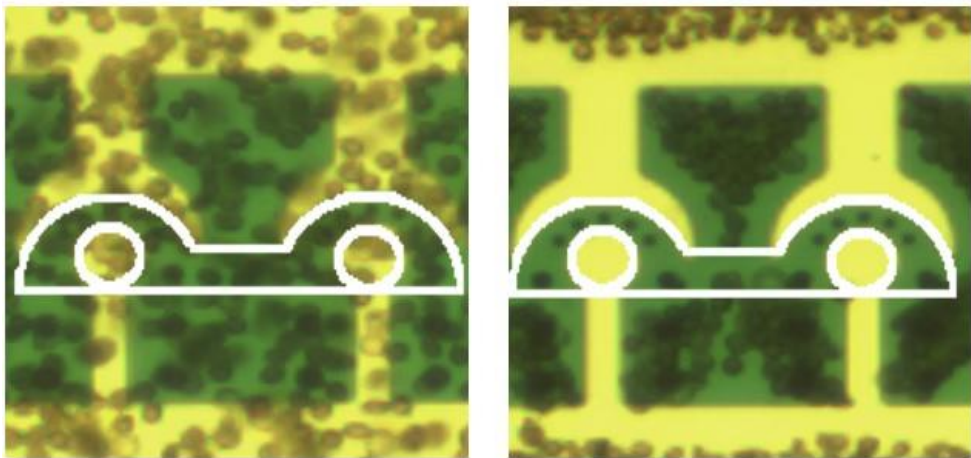
Figure 3-34. Two different electrode shapes which could generate strong DEP force. The areas which seem brighter are electrodes and the perfectly circular black dots between electrodes are micropores. The diameters of pores in both cases are  $8 \mu\text{m}$ . It was not possible to find pores in photos before DEP was applied but pores came into view after beads were trapped onto electrodes.

### 3.4.3 Experiment with blood cells

#### 3.4.3.1 Purity

Since viscosity of blood is even higher than that of bead solution, mobility of blood cells was remarkably decreased in comparison to microbeads. It led to ambiguous boundary of cells distribution and left narrow pore array region because cells were less mobile than as expected. The two electrode shapes were already decided in previous chapter (3.4.2 Electrode shape optimization), so they showed good performance as shown in Figure 3-35 electrode. However Figure 3-35 (a) electrode design was not practical, since there was not enough area to make pores in a blood test. The small amount of pore area induced the plasma to not be able to pass through the device easily. Therefore we selected crossed rectangular shape as the optimized one like shown in Figure 3-35 (b). We counted the number of red bold cells which remained in a specified area noted by a white solid line in Figure 3-35, and reported the ratios between them with and without DEP. Keeping the same structure, we solely modified the dimensions of electrodes, such as gaps between electrodes and aspect ratios of them. After the voltage was applied (1 MHz, 6.5 V<sub>pp</sub>), blood cells were repelled from the electrode tip where the largest electric field exists, as shown in Figure 3-36. The most appropriate frequency for blood cells is about 1 MHz, slightly different from that of beads and this process was completed within 4 minutes. The concentration of blood mixture with isotonic buffer was 40:1.

(a)

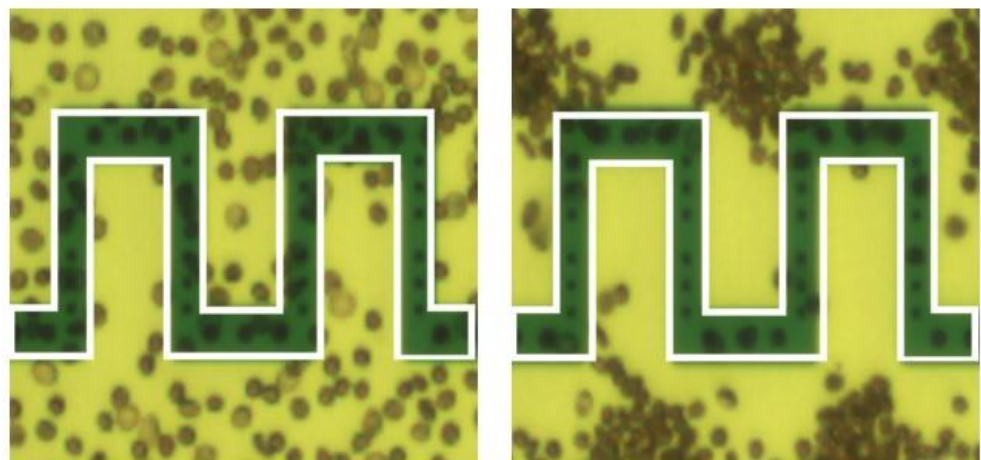


# of blood cells : 20

# of blood cells : 4

Efficiency: 80.0 %

(b)

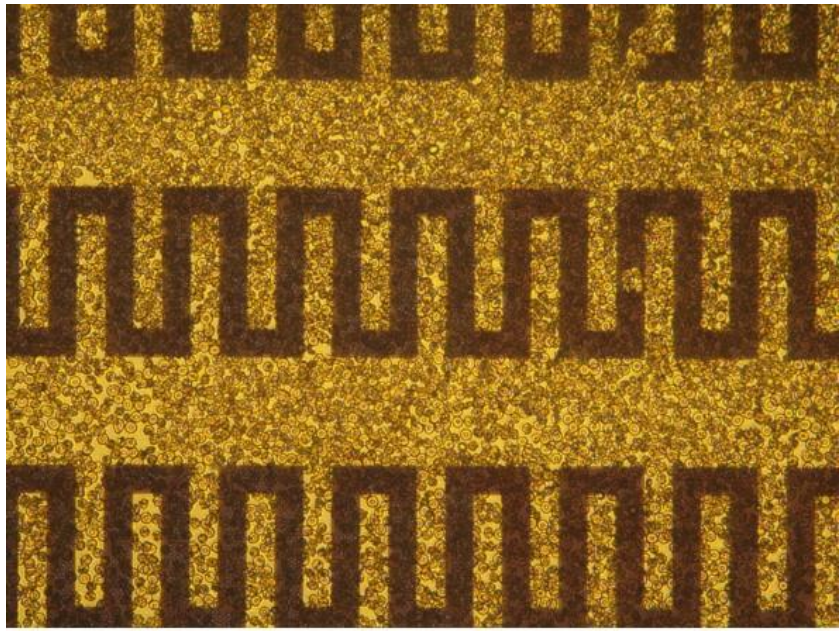


# of blood cells : 49

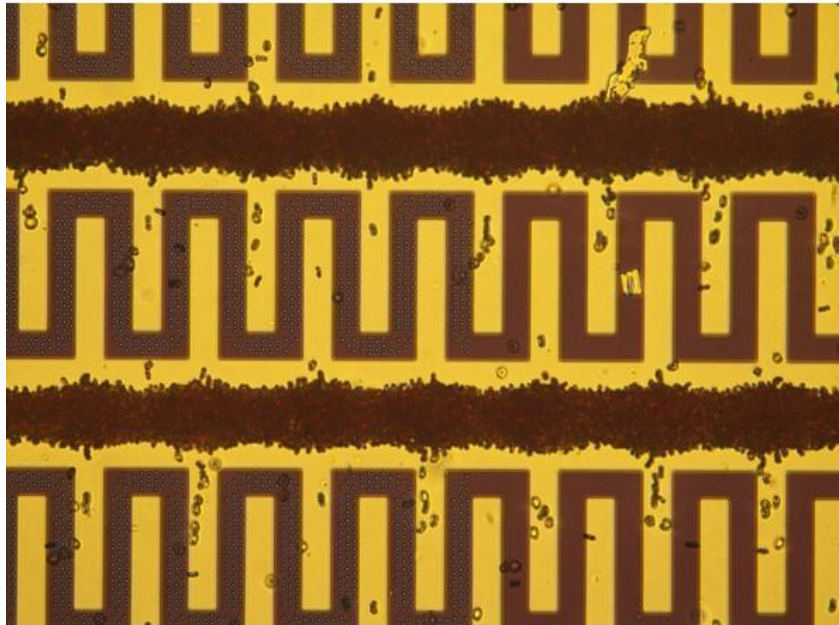
# of blood cells : 12

Efficiency: 75.5 %

Figure 3-35. Blood cell separation efficiencies of different electrode shapes. Photos show comparison between the number of blood cells near pore array before and after applying DEP voltage.



(a) DEP **OFF**



(b) DEP **ON**

Figure 3-36. Blood cell separation with DEP by metal microscope. DEP conditions are  $V_{pp} = 10$  V, 500 kHz, 3min, (20:1 = buffer: blood).

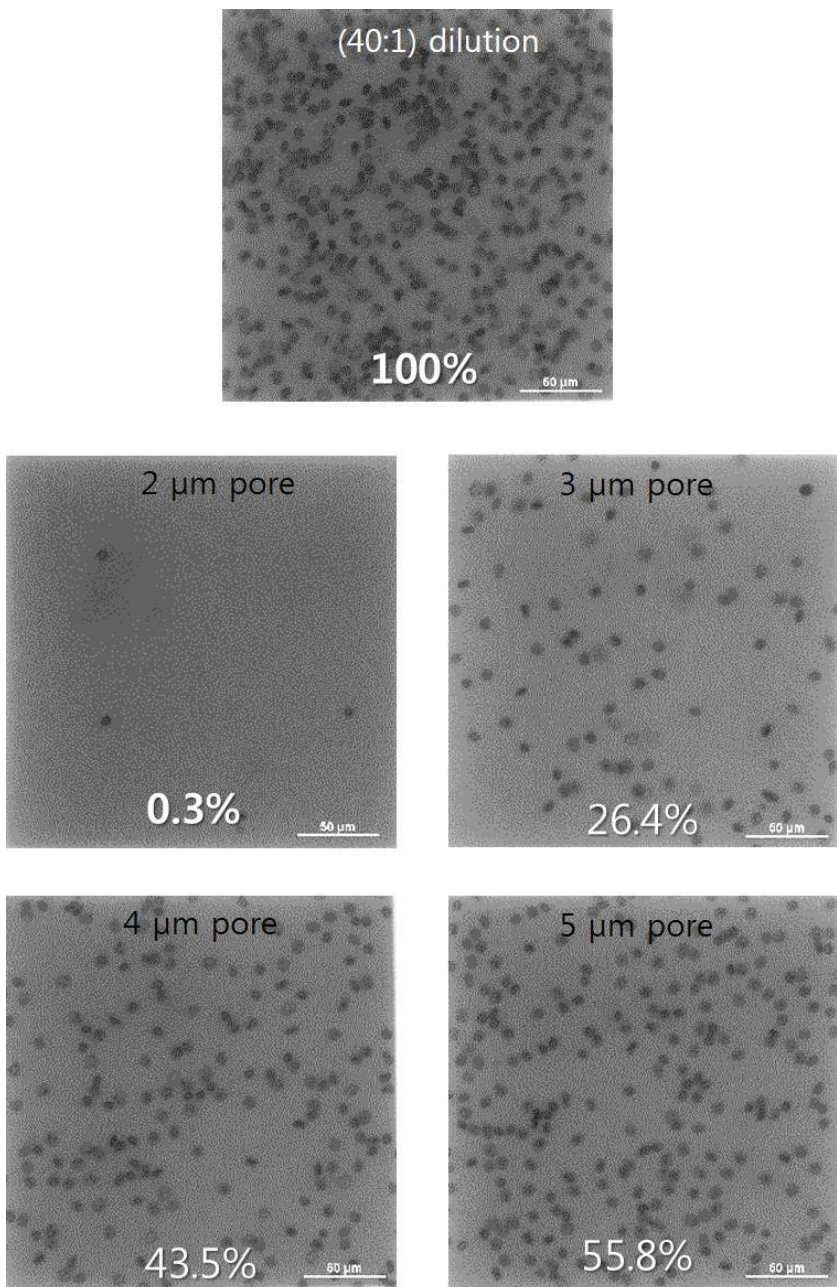


Figure 3-37. Purity of blood cell after filtration with various pore sizes. (a) Original diluted blood (b) 2  $\mu\text{m}$  pore result, (c) 3  $\mu\text{m}$  pore result, (d) 4  $\mu\text{m}$  pore result, and (e) 5  $\mu\text{m}$  pore result by inverted microscope

### 3.4.3.2 Recovery rate

The pore array, meanwhile, was tested with diluted blood. Although there has been an upper fluidic channel on the device, we did not use it while pore performance was tested. Blood sample was dropped right at the exact region where pore and electrode arrays were placed, in order to report the numerical change in the contact angle. After measuring an initial contact angle, it was compared with another contact angle after certain minutes have passed; we usually set the interval for 5 minutes. With measuring the contact angle and the radius of circular border plane between liquid and surface, it was possible to estimate the volume of the droplet in Figure 3-38. Equation 3.9 and Figure 3-38 explains the relationship.

$$V = \frac{\pi R^3}{3} (1 - \cos\theta)^2 (2 + \cos\theta) \quad (3.9)$$

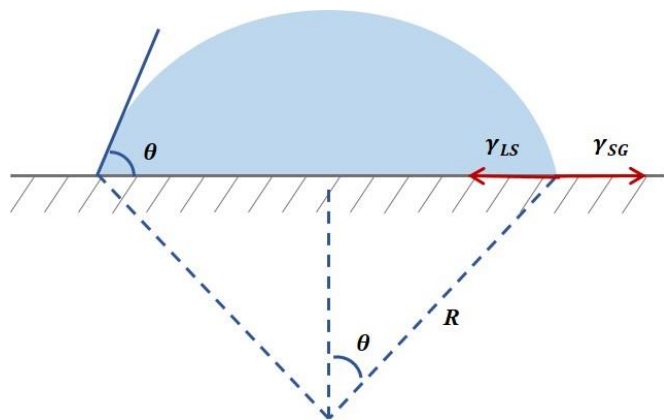


Figure 3-38. Concept diagram of relation between a droplet on surface and contact angle.

Capillary is the driving force which lets liquid above the device pass through the pores. However liquid could not be extracted efficiently due to dimensions of pores being very small. There was a trade-off between recovery rate and purity; if the pore widens, plasma flow goes up but cells also penetrate pores, hence purity decreases. Otherwise, the device holds low recovery but high purity. Therefore, determining a primary diameter range of pores was a very important step in producing an optimized device. For this reason, we tested several devices with different pore sizes.

To increase recovery rate, additional isotonic buffer was filled with the lower chamber and surface treatment was applied on the top and bottom side of the chip. The types of surface treatment were different according to the region. A lower surface and side wall of pores should be hydrophilic so that filtered plasma could be easily diffused. The area near electrode arrays on an upper surface should be hydrophilic due to hydrophobicity of gold. The rest of the upper part needed hydrophobic treatment for sessile drop with a high contact angle in contrast. Laplace pressure ( $\Delta p$ ) in Equation 3.10 states that the higher contact angle droplet equates to a larger pressure.

$$\Delta p = \gamma \left( \frac{1}{R_1} + \frac{1}{R_2} \right) \quad (3.10)$$

In case of  $R_1$  being equal to  $R_2$ , equation could be

$$\Delta p = \gamma \frac{2}{R} \quad (3.11)$$

where  $\Delta p$  is pressure difference,  $\gamma$  is the surface tension and  $R$  is the radius of curvature of the droplet. Figure 3-39 is a schematic diagram regarding surface treatment.

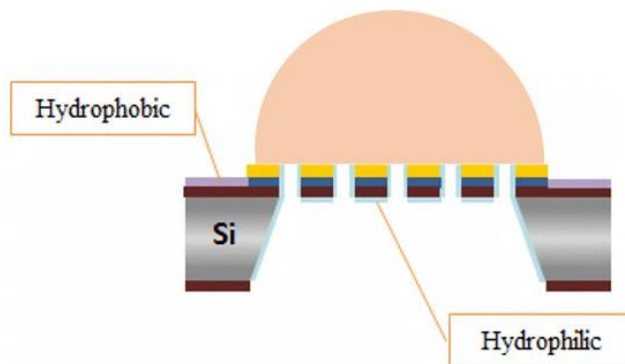


Figure 3-39. Schematic of sessile drop and surface treatment

It was confirmed that as serum passes through the pore membrane the height of serum droplet slowly decreased. Figure 3-40 shows the changes in contact angles 5 minutes after blood was dropped. The device with a diameter of 5  $\mu\text{m}$  or more permitted all blood to pass through. On the other hand, blood stream was stopped with all others.

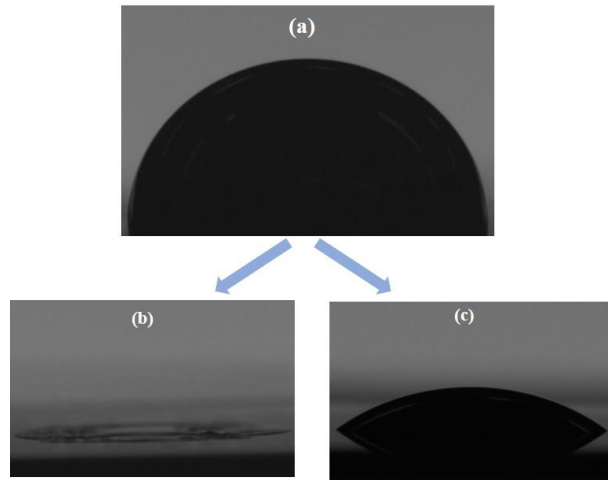


Figure 3-40. Shrinking droplet ( $20 \mu\text{l}$ ) with (a)  $5 \mu\text{m}$  pores and (b)  $3 \mu\text{m}$  pores, 5 minutes after blood dropped on the surface. In the device with a diameter of  $3 \mu\text{m}$ , pores were blocked with blood cells and blood flow was stopped.

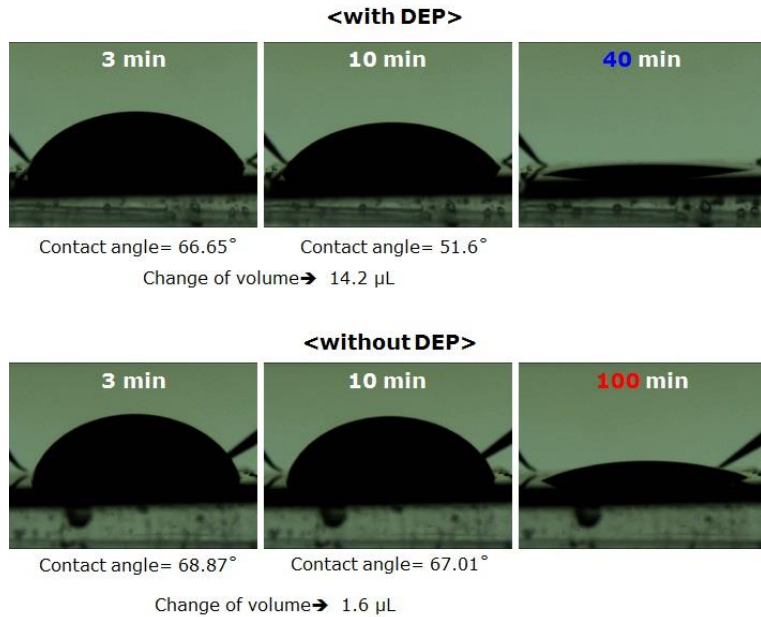


Figure 3-41. Diluted blood cell droplet (40:1,  $40 \mu\text{m}$ ) contact angle change with/without DEP applied ( $V_{pp}=10 \text{ V}$ ,  $500 \text{ kHz}$ ). The droplet volume change is (on:off =  $14.2 : 1.6$ ). Also without DEP, filtration through pore array takes more than 100 min.

We measured recovery and purity depending on 5 different diameters of pores and results from them were plotted on a graph as shown in Figure 3-41. Purity was measured by counting the number of red blood cells before and after filtration per unit area. If the pore size exceeded 9  $\mu\text{m}$ , processes were rapidly finished. It meant DEP could not work because of a strong drag force. By comparing purity and throughput between 9  $\mu\text{m}$  and 5  $\mu\text{m}$  pore array, it was easy to recognize that blood cells were not filtered by the device.

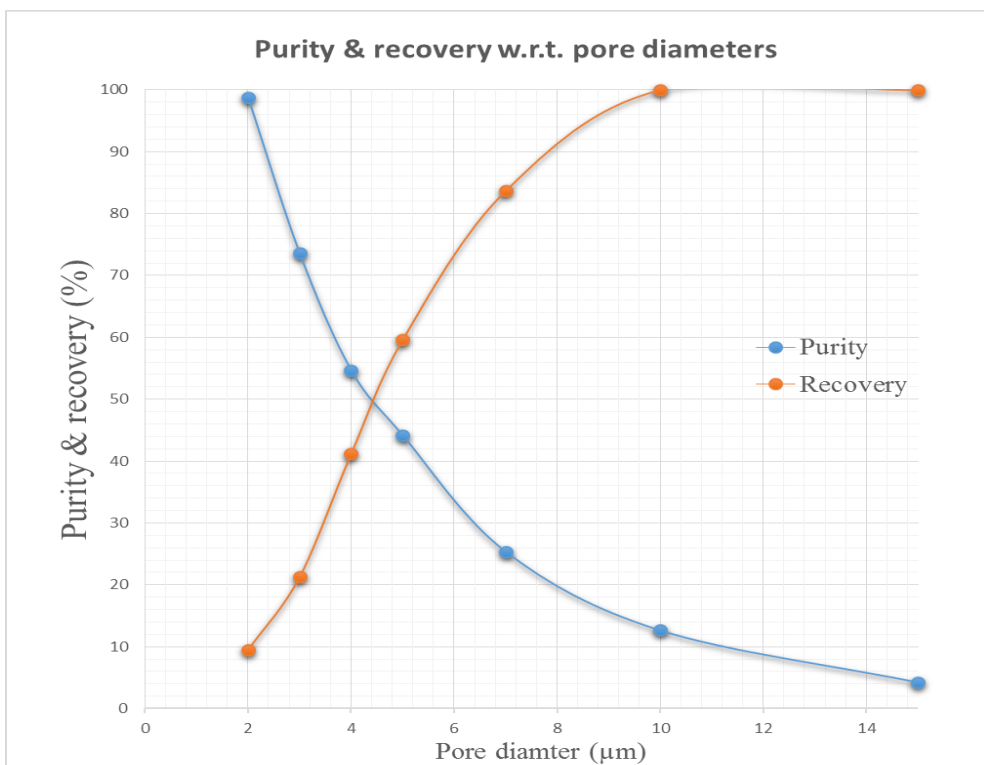


Figure 3-42. Relation between purity and recovery with pore diameter from 2  $\mu\text{m}$  to 15  $\mu\text{m}$ .

On the basis of the results, the proper pore size was able to be estimated. Figure 3-42 gave us the optimized pore size and proper running time. Considering both recovery and purity of the device, pores with a diameter of 4  $\mu\text{m}$  to 5  $\mu\text{m}$  are suitable to assure high throughput separation. As can be seen Figure 3-42, 5 minutes was enough time to extract all plasma from the initial drop with the 5  $\mu\text{m}$  pores

### 3.4.3.3 DEP efficiency

To figure out DEP effectiveness, we experimented with two same samples under same conditions but the only difference was whether DEP was tuned on or not. Figure 3-43 definitely shows the DEP effect. Red blood cells were stacked on electrodes causing pores to be exposed; its pattern being similar to Figure 3-43. Figure 3-43 shows contrary results. Without DEP, cells were randomly stuck onto the device. Since cells blocked pores, plasma could not penetrate the membrane.

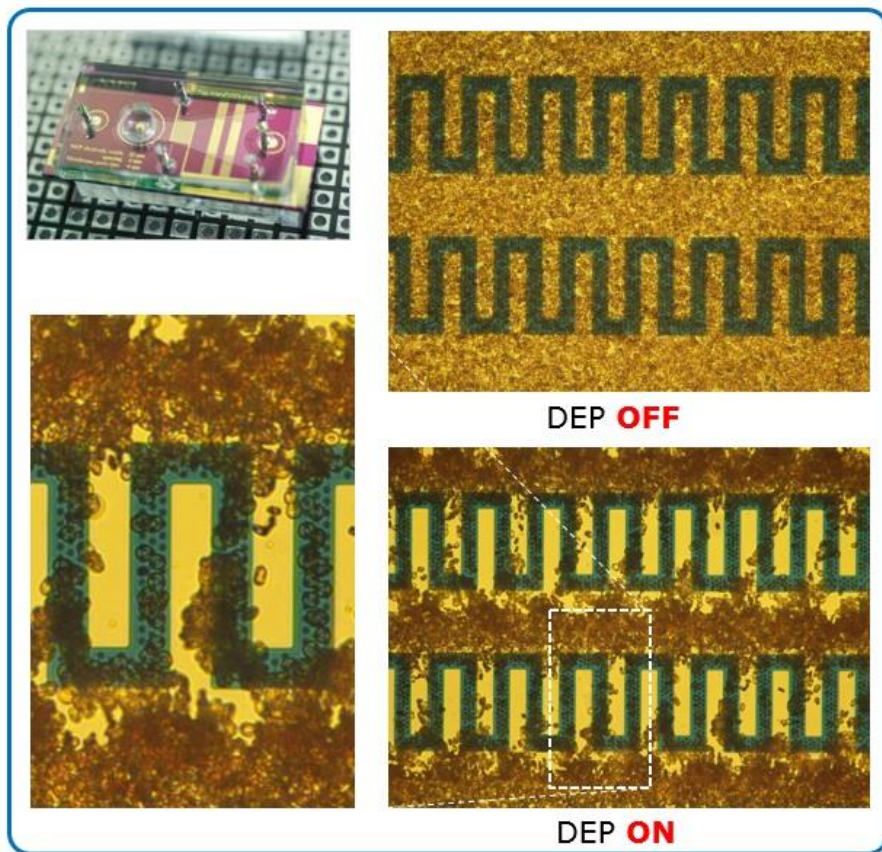


Figure 3-43. DEP effectiveness comparison with diluted blood (20:1). DEP force makes pore array be exposed by moving away blood cells.

### 3.5 Conclusions

We studied several techniques required for developing blood separation system. It has been a part of the present diagnostic sensors. With DEP as one of the most powerful tools for manipulating biological cells, it was demonstrated by using DEP liquid in mixture with particles was passed through pores without blocking effect while particles were repelled from pore array region. Using this technique, we succeeded in separating blood cells from plasma. It was able to be achieved in assistance with micropore array under hydrodynamic systems. We found the appropriate frequency and voltage (1 MHz, 6.5 V<sub>pp</sub> each) when negative DEP were applied on blood cells. Moreover, the electrode array on our devices is the optimal shape in result from numerous pre-experiments. From the analyzed results, this device showed the fastest processing time which means that it had the highest recovery rate. Also, the device with a diameter of 4  $\mu\text{m}$  to 5  $\mu\text{m}$  resulted in the process to be over within 5 minutes, successfully maintaining a certain level of purity (more than 60%). We expect that the blood plasma collected in the channel of this device can be used for various biological diagnostic sensors.

## References

1. Nakashima, Y., S. Hata, and T. Yasuda, *Blood plasma separation and extraction from a minute amount of blood using dielectrophoretic and capillary forces*. Sensors and Actuators B-Chemical, 2010. **145**(1): p. 561-569.
2. Hou, H.W., et al., *Microfluidic Devices for Blood Fractionation*. Micromachines, 2011. **2**(3): p. 319-343.
3. Lange, K., B.E. Rapp, and M. Rapp, *Surface acoustic wave biosensors: a review*. Anal Bioanal Chem, 2008. **391**(5): p. 1509-19.
4. Bhagat, A.A., et al., *Microfluidics for cell separation*. Med Biol Eng Comput, 2010. **48**(10): p. 999-1014.
5. Pamme, N., *Continuous flow separations in microfluidic devices*. Lab Chip, 2007. **7**(12): p. 1644-59.
6. Kersaudy-Kerhoas, M., R. Dhariwal, and M.P. Desmulliez, *Recent advances in microparticle continuous separation*. IET Nanobiotechnol, 2008. **2**(1): p. 1-13.
7. Eijkel, J.C. and A. van den Berg, *Nanotechnology for membranes, filters and sieves. A series of mini-reviews covering new trends in fundamental and applied research, and potential applications of miniaturised technologies*. Lab Chip, 2006. **6**(1): p. 19-23.
8. Tsutsui, H. and C.M. Ho, *Cell Separation by Non-Inertial Force Fields in Microfluidic Systems*. Mech Res Commun, 2009. **36**(1): p. 92-103.
9. Kulrattanarak, T., et al., *Classification and evaluation of microfluidic devices for continuous suspension fractionation*. Adv Colloid Interface Sci, 2008. **142**(1-2): p. 53-66.
10. Toner, M. and D. Irimia, *Blood-on-a-chip*. Annu Rev Biomed Eng, 2005. **7**: p. 77-103.

11. Dimov, I.K., et al., *Stand-alone self-powered integrated microfluidic blood analysis system (SIMBAS)*. Lab Chip, 2011. **11**(5): p. 845-50.
12. Yang, X., et al., *Integrated separation of blood plasma from whole blood for microfluidic paper-based analytical devices*. Lab Chip, 2012. **12**(2): p. 274-80.
13. Gorkin, R., et al., *Centrifugal microfluidics for biomedical applications*. Lab Chip, 2010. **10**(14): p. 1758-73.
14. in [http://anaphyteachushowtoblog.blogspot.kr/2012\\_01\\_21\\_archive.html](http://anaphyteachushowtoblog.blogspot.kr/2012_01_21_archive.html).
15. Azim, W., et al., *Diagnostic significance of serum protein electrophoresis*. Biomedica, 2004. **20**(1): p. 40-44.
16. Kagan, B.M., *The Clinical Significance of the Serum Protein's*. Southern Medical Journal, 1943. **36**(3): p. 234-238.
17. ; Available from: <http://pratted.wordpress.com/2012/11/09/how-to-sort-circulating-tumor-cells-part-i-size/>.
18. Haeberle, S., et al., *Centrifugal extraction of plasma from whole blood on a rotating disk*. Lab Chip, 2006. **6**(6): p. 776-81.
19. Lai, S., et al., *Design of a compact disk-like microfluidic platform for enzyme-linked immunosorbent assay*. Anal Chem, 2004. **76**(7): p. 1832-7.
20. Wong, A.P., et al., *Egg beater as centrifuge: isolating human blood plasma from whole blood in resource-poor settings*. Lab on a Chip, 2008. **8**(12): p. 2032-2037.
21. Manz, A. and H. Becker, *Microsystem technology in chemistry and life sciences*. Vol. 194. 1997: Springer.
22. Ji, H.M., et al., *Silicon-based microfilters for whole blood cell separation*. Biomed Microdevices, 2008. **10**(2): p. 251-7.
23. Ionescu-Zanetti, C., et al., *Mammalian electrophysiology on a microfluidic platform*. Proc Natl Acad Sci U S A, 2005. **102**(26): p. 9112-7.

24. Yang, S., A. Undar, and J.D. Zahn, *A microfluidic device for continuous, real time blood plasma separation*. Lab Chip, 2006. **6**(7): p. 871-80.
25. VanDelinder, V. and A. Groisman, *Separation of plasma from whole human blood in a continuous cross-flow in a molded microfluidic device*. Anal Chem, 2006. **78**(11): p. 3765-71.
26. Xing, X., et al., *Micromachined membrane particle filters*. Sensors and Actuators a-Physical, 1999. **73**(1-2): p. 184-191.
27. Sung, J.M., *Dielectrophoresis and Optoelectronic Tweezers for Nanomanipulation*.
28. Pohl, H.A., *The motion and precipitation of suspensoids in divergent electric fields*. Journal of Applied Physics, 2004. **22**(7): p. 869-871.
29. Lenshof, A., et al., *Acoustic whole blood plasmapheresis chip for prostate specific antigen microarray diagnostics*. Anal Chem, 2009. **81**(15): p. 6030-7.
30. Arifin, D.R., L.Y. Yeo, and J.R. Friend, *Microfluidic blood plasma separation via bulk electrohydrodynamic flows*. Biomicrofluidics, 2006. **1**(1): p. 014103.
31. Petersson, F., et al., *Separation of lipids from blood utilizing ultrasonic standing waves in microfluidic channels*. Analyst, 2004. **129**(10): p. 938-43.
32. Petersson, F., et al., *Continuous separation of lipid particles from erythrocytes by means of laminar flow and acoustic standing wave forces*. Lab Chip, 2005. **5**(1): p. 20-2.
33. Yeo, L.Y., J.R. Friend, and D.R. Arifin, *Electric tempest in a teacup: The tea leaf analogy to microfluidic blood plasma separation*. Applied Physics Letters, 2006. **89**(10): p. 103516.
34. Xu, C., et al., *Dielectrophoresis of human red cells in microchips*. Electrophoresis, 1999. **20**(9): p. 1829-31.

35. Kuczenski, R.S., H.C. Chang, and A. Revzin, *Dielectrophoretic microfluidic device for the continuous sorting of Escherichia coli from blood cells*. Biomicrofluidics, 2011. **5**(3): p. 32005-3200515.
36. Gimza, J. and D. Wachner, *A unified resistor-capacitor model for impedance, dielectrophoresis, electrorotation, and induced transmembrane potential*. Biophys J, 1998. **75**(2): p. 1107-16.
37. in <http://www.youtube.com/watch?v=7NSEFVbzTAU>.
38. Mellor, J.W., *A Comprehensive Treatise on Inorganic and Theoretical Chemistry: Volume V*. 1924: Longmans, Green and Company.
39. Xia, Y., et al., *Complex Optical Surfaces Formed by Replica Molding Against Elastomeric Masters*. Science, 1996. **273**(5273): p. 347-9.

## 4 Summary

Scale of context is a keyword to comprehend diverse multiscale particle physics and behavior. Depending on the particle dimension from macro particle to ionic range, the dominant force applied to particle can be absolutely different. Thus, particle separation methods also should be changed according to the size of particles. For instance, particles under 20  $\mu\text{m}$  size are generally recommended to use wet screening instead of dry screening because of assemble with other particles and adhesion on large particles due to humidity in air. This phenomenon can be interpreted by dimensionless number  $Re$ , which is defined by the ratio of inertia to viscous force.  $Re$  of the small size particle is low, which means viscous effect is greater than the inertia effect in tiny scale. Comparing with the typical macro region, various distinct phenomenon occur in micro or nano region because the negligible force in large world could govern the particle behavior in small world. Therefore, not only viscous force but also other various minor forces in macro domain could play decisive roles in micro domain. In this way, multiscale particle physics are required to investigate and to analyze with consideration about scale of context.

## 4.1 Comparison between molecular and micro scale particles

Among the wide range of multiscale particles, DNA as molecular particle and blood cell as micro particle are the selected examples to separate with pore array membrane. Since DNA and blood cell are completely different particle in scale, we need to consider the different physics on both particles. Each particle is studied about the dominate forces, analysis, device and applications.

Separation of molecular particle is investigated. DNA and protein are separated by electrophoresis and nano-porous membrane. Gel electrophoresis, for example, is used to sort charged biopolymers according to weights for interrogating the molecular composition of a certain mixture. Proteins that cause a disease can be removed through a blood filtration from a patient. DNA purification can be achieved through a size specific separation and collection after cell lysis. Among various applications, the nano-pore based translocation of single strand DNA (ssDNA) is a vital issue because of their utility in fast DNA sequencing. The idea is to electrophoretic ally drive negatively charged nucleotides into a nano-pore and identify each constituent nucleotide by monitoring currents while the DNA molecules resides within the pore. For efficient biomolecule separation based on nano-porous membrane, some of the key properties that materials with controlled pore diameter, length and surface chemistry are required. However, commercially available nano-porous membranes possess pore size-cutoff properties and low transport rates since they generally have broad size distributions and relatively large thickness values. Anodized aluminum oxide (AAO) membrane has the potential to be a good nano-porous membrane element for biomolecule separation because of its

very high pore density, e.g., up to  $24 \times 10^{20}$  pores/cm<sup>2</sup>, its relative uniform pore sizes, as well as the availability of the sub 100 nm pores.

Also separation of micro scale particle is investigated with blood cell. Plasma extraction (= removing blood cell from blood) is used by dielectrophoresis and micro pore array membrane. Blood plasma separation requires for the monitoring of cholesterol, glucose, and hepatic function in blood. Recently, various types of blood cell separation method have developed such as microchannel with trench (SIMBAS), paper-based analytical device ( $\mu$ -PAD), centrifugal platform, and surface acoustic wave (SAW) and so on. However, these methods are generally horizontal systems with limited flux capacity per unit time. Here we suggest a vertical separation device for high throughput and high quality separation efficiency through integration of dielectrophoretic (DEP) function on a micro-porous membrane. We target enhancing the separation efficiency and speed by establishing a “virtual barrier” with DEP function integrated on a membrane with a regular pore size and distribution. Metal electrodes are patterned on the membrane for preventing clogging by blood cells through the application of negative DEP, while helping blood plasma to pass through the membrane pores selectively. Essentially the DEP force is designed to block the passage of red blood cells (RBCs), which account for more than 90% of the whole blood cells including white blood cells (WBCs) and platelets. The diameter of micro pore array are varied between 3~10  $\mu\text{m}$ , and target to filter RBCs of which size is approximately 6~8  $\mu\text{m}$ .

In spite of the same principle of size exclusive filtration in the two multiscale particles, the particle driving forces are different, DNA is electrophoresis (EP) and blood cell is dielectrophoresis (DEP), because DNA is a charged particle and blood cell is uncharged particle. Even the filtration pore size control methods are different. In micro particle, MEMS fabrication can support the dimension for the filtration. On the other hands, in molecular particle, not only physical pore size but also electrical double layer (EDL) determines the effective filtration pore size. Moreover, relative ratio between pore size and particle size means different depending on scale of context.

## 4.2 Future works

Recently applications in healthcare and environment use the separation of particles as a crucial process. Examples include pharmaceutical manufacturing/analysis, removal of air pollutants, wastewater treatment, and alternative energy production and storage. Based on mechanical, chemical, electromagnetic, and thermal properties of particles, various particle separation technologies have been developed over a period of time for different applications. Among these separation technologies, membrane separation is an intuitive and effective method because of direct particle-pore interaction. Also membrane method has been well-developed and widely used in the field of microbiology. However more fundamental study is required to use the

membrane-based separation for modern biological applications such as molecular binary separation and red blood cell filtering for point of care diagnosis.

Conventional AAO membranes are already used for various applications such as bio/chemical sensors, pre-treatment filters, and nanoscale templates. These AAO membranes are made from Al-foil substrate of thickness 50 to 100  $\mu\text{m}$ , and then usually assembled in to the other device. On the other hand, AAO membrane in this work is directly fabricated from deposited Al ( $< 2 \mu\text{m}$  thickness) on silicon substrate, followed by a MEMS fabrication process to complete an integrated device. This direct AAO fabrication process can reduce the length of AAO nanochannel and improve the compatibility with microfluidic devices.

Blood cell is separated by micro pore array membrane with pore size of 2 to 10  $\mu\text{m}$ . For effective blood cells separation, the size of pores and the number of pores are investigated. The blood cells which might block the pores are repelled from the pore by DEP force. DEP parameters such as electrode shape and applied voltage of frequency/amplitude, are studied for enhanced purity and recovery. In this analysis it is crucial to compare hydrodynamic drag and DEP forces.

In this study, the separation processes are verified using precise pore size control. In order to apply different scale of particles, different pore size control methods are required. For, example, using atomic layer deposition (ALD) can help the thickness control as 1 nm resolution. Also, depending on different particles, other driving force

to move the particle is necessary. These separation methods can be more efficient with integration of various microfluidic components.

### 4.3 Conclusions

The understanding of characteristics of multiscale particles is applied to the separation of particles in two different domains such as DNA and blood cell with pore array membrane. Each of these particles has different size scale and characteristic properties such as density, elasticity, conductivity, etc. Basic principle of separation for nano pore is the combination of physical pore diameter and thickness of electrical double layer. On the other hand, basic principle of separation for micro pore is the physical dimension of pore with respect to the particle size interacting with drag and DEP forces. Though EDL is negligible in micro pore because of relatively large pore diameter, EDL is an important factor in nano pore because of relatively small pore diameter. Also the driving forces for nano particle (DNA) and micro particle (Blood cell) are electrophoresis and dielectrophoresis, respectively. Through this study the effect of various factors that control for pore transport physics in different dimension is evaluated. This report presents a theoretical and engineering analysis of separation technique based on particle size, including experimental results of separation of DNA and blood cell from the blood using two different types of membrane devices.

## Abstract in Korean (국문초록)

### 포어어레이 박막을 이용한 멀티스케일 입자분리

멀티스케일 입자의 거동 및 현상을 이해할 때, 입자의 크기에 따라서 고려해야 할 물리 법칙이 다르다. 즉, 거대 입자영역에서는 무시할 수 있었던 요인이 미소 입자영역에서는 오히려 지배적으로 작용하기도 한다. 예를 들어, DNA나 단백질과 같은 분자 입자의 움직임에서는, 중력보다도 온도 및 pH에 의한 영향이 더 중요하게 고려된다. 최근 건강 및 환경에 대한 관심이 커지면서 멀티스케일 입자 분리기술의 중요성이 높아졌다. 예를 들어, 입자분리 기술은 의약품 제조 및 분석, 대기오염물질 제거, 폐수처리, 대체에너지 제조 및 저장 등 넓은 분야에서 활용되고 있다. 이런 입자분리 기술은 오랫동안 다양한 기계적, 화학적, 전자기적 원리를 이용하여 발달해왔다. 그 중에서 다공성 박막을 이용한 입자분리기술은 입자와 기공 사이의 크기의 관계를 이용하기 때문에 직관적이고 효과적이다. 하지만, 현재의 박막 입자분리 기술은 분자 스케일 입자의 이진분리와 혈액 여과 point-of-care (POC)와 같은 새로운 생화학 분야에 적용하기에는 추가적인 연구가 필요하다. 따라서 본 연구에서는 포어어레이 박막을 이용하여, 분자 스케일의 DNA와 단백질 이진분리와 마이크로 입자 스케일의 혈구분리에 대해서 연구를 진행하였다.

먼저, 기공의 크기가 100 nm 이하로 잘 조절된 나노다공성 AAO 박막을 이용하여 단백질 복합체와 DNA를 분리하였다. 베퍼의 이온농도에 따라

서 EDL 두께를 조절함으로써, 나노기공을 통한 분자 입자분리를 효과적으로 이룰 수 있었다. 또한, 전기영동 방법을 통해서 음전하를 띠는 DNA가 나노기공 박막을 통과하도록 유도하였다 DNA와 DNA/단백질 복합체 사이의 크기 차이를 이용하여 DNA를 이진분리 하였다. DNA의 이동을 확인하기 위해서 형광 강도의 변화를 측정하고, 각각의 상관관계에 대해서 분석하였다. AAO는 이미 생화학 센서, 전처리 필터, 그리고 나노스케일 템플릿 등의 다양한 분야에서 활용되고 있다. 상용으로 사용되는 AAO 박막은 알루미늄 호일로 만들어지기 때문에 두께가 50~100  $\mu\text{m}$  되며, 다른 장치에 결합해서 사용해야 한다. 반면, 본 연구에서 제작한 AAO 박막은 실리콘 기판 위에 직접 2  $\mu\text{m}$  이하 두께의 알루미늄을 증착하여 제작되었고, 후속 MEMS 공정과정을 통해서 다른 장치와 쉽게 결합하였다. 이 같은 AAO 박막 제작방식은 AAO 나노채널의 길이를 줄일 수 있으며, 또한 마이크로 유체장치와의 결합을 용이하게 한다.

또한, 2~10  $\mu\text{m}$  크기의 포어어레이 박막을 이용하여 혈구를 분리하였다. 효과적인 혈구분리를 위해서 기공의 크기, 개수, 그리고 간격을 조절하였다. 그리고 유전영동을 통해서 기공을 막는 혈구를 제거하였다. 전극의 형상, 전압의 주파수 및 진폭을 조절하여, 순도 및 회수율을 향상할 수 있었다. 혈구에 작용하는 유체 역학적 힘과 유전영동 힘을 비교를 통해서, 실험만으로 예상할 수 없는 복잡한 변수 간의 상관관계에 대해서 이해할 수 있었다. 혈액에서 추출된 혈장을 통해서 콜레스테롤, 포도당, 간기능에 대해서 확인할 수 있는 Point-of-care (POC) 진단이 필요하다. 최근 많은 연구가 마이크로 유체장치를 기반으로 진행되고 있다. 상용적인 마이크로 유체장치는 주시기를 통해서 유체의 흐름을 제어하기 때문에, 비교적 많은 양의 샘플이 필요하다. 하지만 일반적으로 POC는 소형의 플

랫폼 상에서 적은 양의 샘플량이 요구된다. 본 연구에서는 적은 샘플 양으로도 뛰어난 성능을 가진 혈구 입자분리 장치를 개발하였다.

멀티스케일 입자의 특성에 대한 이해를 두 가지 다른 스케일 영역에 존재하는 DNA와 혈구의 분리에 적용하였다. 위의 두 가지 입자는 크기뿐만 아니라 밀도, 탄성, 전도도 등의 측면에서도 다르다. 나노 입자의 분리 과정에서는 물리적인 기공의 크기와 EDL 두께를 결합된 기공 크기에 대해서 고려하였다. 반면, 마이크로 입자의 분리과정에서는 유체역학적 힘과 유전영동 힘의 비교를 통해서, 마이크로 입자와 기공의 관계를 고려하였다. 마이크로 기공에서는 EDL의 두께가 상대적으로 작기 때문에 무시할 수 있지만, 나노 기공에서 EDL 두께가 상대적으로 크기 때문에 중요한 변수로 작용한다. 또한, 나노 입자 (DNA)와 마이크로 입자 (혈구)에는 각각 전기영동과 유전영동이라는 다른 힘이 적용되었다. 본 연구를 통하여, 다른 크기 영역에 있는 입자가 기공을 통해서 이동할 때 영향을 미칠 수 있는 요인에 대해서 조사하였다. 본 연구는 입자크기에 따른 입자 분리기술에 대해서 조사하고 이론적으로 해석하였으며, 두 가지 다른 박막 장치를 구성하여 DNA와 혈구 분리 실험을 성공적으로 보일 수 있었다.

.....

주요어: 멀티스케일 입자, 분리, 박막 분리기술, 입자-기공 크기관계, DNA, 분자, 혈구, 포어어레이 박막, AAO, EDL, 전기영동, 유전영동

학 번: 2005-21012